CAUÊ ZIRNBERGER LAZANEO

Mixing and submesoscale dynamics in the western South Atlantic Ocean

São Paulo

2021

CAUÊ ZIRNBERGER LAZANEO

Mixing and submesoscale dynamics in the western South Atlantic Ocean

A dissertation submitted to the Oceanographic Institute of the University of São Paulo in partial fulfillment of the requirements for the degree of Doctor of Science with a concentration in Physical Oceanography to the joint degree program of University of São Paulo (Brazil) and University of Massachusetts (USA).

USP Advisor:
Prof. Dr. Ilson Carlos Almeida da Silveira
UMass Dartmouth Advisor:
Prof. Dr. Amit Tandon

São Paulo

2021

LAZANEO, C. Z. **Mixing and submesoscale dynamics in the western South Atlantic Ocean**. Doctoral dissertation. Joint Program: Oceanographic Institute of the University of São Paulo and the School of Marine Science and Technology of the University of Massachusetts Dartmouth. Doctoral dissertation presented as a requirement for the degree of Doctor of Science with a concentration in Physical Oceanography to the joint degree program of University of São Paulo (Brazil) and University of Massachusetts (USA).

Evaluated on 07 / 29 / 2021

Committee in charge

Prof. Dr. _____ Institution _____
Chair Signature _____

Prof. Dr. _____ Institution _____

Grade _____ Signature _____

Prof. Dr. _____ Institution _____

Grade _____ Signature _____

Prof. Dr. _____ Institution _____

Grade _____ Signature _____

Prof. Dr. _____ Institution _____

Grade _____ Signature _____

I dedicate this work to those who believe in science

ACKNOWLEDGEMENTS

I would like to thank my advisors, Ilson and Amit, for their guidance and help during my Ph.D. course. They have taught me how to become a scientist, spending countless hours talking about my research and providing invaluable feedback on my work. Their encouragement, support, and advice throughout my graduate career have enabled me to complete this dissertation, and I cannot thank them enough.

I want to extend the thank to all members of my committee and gratefully acknowledge their input into this dissertation: Paulo Calil, Daniel MacDonald, and Marcelo Dottori. I also want to thank Prof. Miles Sundermeyer and Prof. Steven Lohrenz for their support in the Dual Degree process of application.

Thanks to my office mates : Dante Napolitano, Iury Simões, Agata Piffer, Igor Farias, Filipe Pereira, Felipe Vilella, Caíque Luko, Pedro Walfir, Julia Araújo, Siddhant Kerhalkar and Shikha Singh. Thanks to friends from IOUSP I made during the Ph.D., Danilo Silva, and Dalton Sasaki, and those I met a long time ago since the undergraduate and who are still close to me, Laura Verona and obviously Juliana Mancio. It is precious to have an "informal committee of knowledge friends" to share my crazy thoughts about geophysical fluid dynamics. It impossible to finish a Ph.D. without “a little help from my friends...”

I want to take this opportunity to thank the teachers and mentors who helped me along my way. Each of them has made a substantial contribution to my career, and I wouldn’t be here without them. Also, I want to thank the staff of the IOUSP (Ana Paula, Daniel, and Letícia) and the staff of the SMAST (Mike Marino, André Schmidt,

Gail Lyonnais, Arlene Wilkinson, Cindy Costa, and Susan Silva) for all the assistance. Thanks to Frank Smith (Chico) for helping me in the editing of part of the manuscripts presented here. I would like to especially thank André and his family for their friendship and countless support during the whole time I lived in the USA.

Thanks to my parents and grandmother, who are my "porto seguro". From the earliest age, they gave me wings and have encouraged me to explore the world. Last but not least, a special thanks to Juliana. Ju, your love, support, ability to cheer me up, and scientific skills were essential to the conclusion of this academic step. Thanks!

This study was financed in part by the Coordenação de Aperfeiçoamento de Pessoal de Nível Superior - Brasil (CAPES) - Finance Code 001. This study was also financed in part by the Conselho Nacional de Desenvolvimento Científico e Tecnológico - CNPq (Processo 205857/2018-3), and Petróleo Brasileiro S.A. (Petrobras) through the Santos Project (Petrobras: 3368)

Resumo

LAZANEO, C. Z. **Mixing and submesoscale dynamics in the western South Atlantic Ocean**. 2021. 135 f. Tese (Doutorado) – Instituto Oceanográfico, Universidade de São Paulo e *School of Marine Science and Technology*, *University of Massachusetts Dartmouth*. São Paulo, 2021.

Esta dissertação aborda dois processos oceânicos que resultam na dissipação de energia cinética turbulenta no oeste do Oceano Atlântico Sul. Primeiramente, abordamos o fluxo turbulento vertical e a mistura em nível picnoclínico, relacionado à reversão do escoamento entre a Corrente do Brasil (CB) e a Corrente de Contorno Intermediária (CCI). Em segundo lugar, abordamos o efeito da topografia da Cadeia Vitória-Trindade (CVT) na geração de vórtices de submesoescala de subsuperfície, que resultam na dissipação da energia cinética turbulenta, bem como em processos de mistura. No primeiro estudo, investigamos o papel do cisalhamento vertical gerado pela reversão do escoamento entre a CB e a CCI, que escoa logo abaixo da camada de mistura na latitude de 21,6° S. A partir de medições de microestrutura, inéditas na região, observamos que o cisalhamento vertical na interface entre as duas correntes desestabiliza localmente a coluna d'água, podendo superar o efeito estabilizador da estratificação. Assim, ocorrem processos de mistura, resultando em trocas verticais de propriedades na base da camada de mistura. Em particular, calculamos o fluxo vertical de nitrato e observamos que a turbulência pode fornecer nutrientes à camada superior. No segundo estudo, buscamos estudar vórtices coerentes de submesoescala (SCVs) intra-picnoclínicos na região da CVT, a partir de observações sinóticas. Capturamos dois SCVs anticiclônicos embebidos em um meandro da Corrente Sul Equatorial (CSE), a partir de medições de alta resolução de temperatura, salinidade e velocidade. Os SCVs foram encontrados à sotavento do Monte Columbia (20,5° S, 32,3° W). Como essas estruturas foram observadas adjacentes e interagindo, interpretamos sua estrutura como uma versão de submesoescala do efeito Fujiwhara no oceano. Ambos os vórtices apresentaram baixos valores de vorticidade potencial, e assinaturas distintas de temperatura e salinidade, relativas às águas circundantes. As características mais homogêneas da água do interior dos SCVs são resultado de mistura. Por meio de medições de microestrutura feitas em um dos SCVs, observamos taxas de dissipação de energia cinética turbulenta semelhantes, em magnitude, às medidas da camada de mistura. Até onde sabemos, essas são as primeiras medições de microestrutura feitas no interior de uma SCV intra-picnoclínico. Não podemos determinar a região de formação de tais SCVs a partir de um transecto hidrográfico. No entanto, sugerimos que eles poderiam ter sido gerados através da interação entre escoamento e topografia, uma vez que o meandro

da CSE, o qual foram observados os SCVs embebidos, foi observado interagindo com a Ilha da Trindade dois meses antes. No terceiro estudo, investigamos se o CVT tem, ou não, propensão para gerar vórtices de submesoescala. Em seguida, simulamos, com um modelo numérico oceânico regional, a CSE interagindo com a cadeia. Observamos que este tipo de vórtice é frequentemente formado na região, em diferentes feições topográficas e diferentes profundidades (intra e sub-picnoclínicas) ao longo de sua extensão de 900 km. Simulamos a geração de SCV com ambas as polaridades. A partir da interação entre o CSE e a topografia da CVT, filamentos vorticais de número de Rossby O(1) são formados a jusante da topografia, criando anomalias de vorticidade potencial. Esses filamentos eventualmente evoluem, enrolam e formam SCVs. Sugerimos que a CVT pode ser considerada um *hotspot* para a geração de vórtices de submesoescala. Por fim, destacamos a importância do oeste do Oceano Atlântico Sul no desenvolvimento de processos de pequena escala e dissipação de energia. A região é fundamental para a compreensão do balanço de energia do oceano.

Palavras-chave: Turbulência e mistura oceânica. Interação escoamento-topografia. Cascata de energia direta. Vórtice coerente de submesoescala.

Abstract

LAZANEO, C. Z. **Mixing and submesoscale dynamics in the western South Atlantic Ocean**. 2021. 135 f. Doctoral dissertation – Oceanographic Institute of the University of São Paulo and the School of Marine Science and Technology of the University of Massachusetts Dartmouth. São Paulo, 2021.

This dissertation addresses two oceanic processes that result in the dissipation of turbulent kinetic energy in the western South Atlantic Ocean. We first approach the vertical turbulent flux and mixing at pycnoclinic level related to the flow reversal between the Brazil Current (BC) and the Intermediate Western Boundary Current (IWBC). We secondly address the effect of the topography of the Vitória-Trindade Ridge (VTR) on the generation of subsurface submesoscale vortices, which results in the dissipation of turbulent kinetic energy as well as mixing. In the first study, we investigate the role of the vertical shear generated by the flow reversal between the poleward-flowing Brazil Current (BC) and the equatorward-flowing Intermediate Western Boundary Current (IWBC), which occurs just below the mixed layer at the latitude of 21.6° S. From unprecedented measurements of microstructure in the region, we observe that the vertical shear at the interface between the two currents locally destabilizes the water column, and may overcome the stabilizing effect of stratification. Thus, mixing processes occur, resulting in vertical exchanges of various properties at the base of the mixed layer. In particular, we compute the vertical nitrate flux, and observe that turbulence may supply the upper layer with nutrients. In the second study, we seek intrapycnoclinic, submesoscale coherent vortices (SCVs) in the VTR region from synoptic observations. We captured two anticyclonic SCVs embedded in a meander of the South Equatorial Current (SEC) from high-resolution measurements of temperature, salinity, and velocity. The SCVs were found at the lee of the Columbia Seamount (20.5° S, 32.3° W). As these structures are adjacent and interacting, we interpret their observed structure as a submesoscale version of the Fujiwhara effect in the ocean. Both eddies present low potential vorticity, and distinct signatures of temperature and salinity relatively to surrounding waters. The more homogeneous water characteristics are a result of mixing in their interior. Through microstructure measurements taken in one of the SCVs, we observe turbulent kinetic energy dissipation rates similar in magnitude to those measured in the mixed layer. To the best of our knowledge, these are the first microstructure measurements taken in the interior of an intrapycnoclinic SCV. We cannot determine the region of formation of such SCVs from one hydrographic transect. However, we suggest that they could be generated through flow-topography interaction since the SEC meander was observed interacting with the Trindade Island two months earlier.

In the third study, we investigate whether the VTR is prone to generate submesoscale vortices. We then simulate, with a regional ocean numerical model, the SEC interacting with the ridge. We observe that this type of vortex is often formed in the region at different topographic features and different (intra- and subpycnoclinic) depths along its 900km extension. We simulate SCV generation with both polarities. From the interaction between the SEC and the topographic features of the VTR, vortical filaments of Rossby number $\mathcal{O}(1)$ are formed downstream of the topography, creating potential vorticity anomalies. These filaments eventually evolve, roll up and form SCVs. We suggest that VTR can be considered a hotspot for the generation of submesoscale vortices. Finally, we highlight the importance of the western South Atlantic Ocean regarding the development of small-scale processes and energy dissipation. This region is key to the comprehension of the ocean energy budget.

Keywords: Turbulence and ocean mixing. Flow-topography interaction. Forward energy cascade. Submesoscale coherent vortex.

List of Figures

List of Tables

Contents

CHAPTER 1.

INTRODUCTION

The oceans that cover the solid surface of the Earth are almost in a turbulent state. This state involves eddying motions visible at scales of clouds, smokes, or even patches of foam in the ocean (Thorpe, 2005). Movements at these scales are efficient in transferring momentum and heat in the ocean. Processes as dispersion, stirring, and mixing in the ocean are also characteristic of turbulent motions.

Turbulence is usually described by key characteristics that distinguish it from non-turbulent flows. According to Tennekes and Lumley (1989), turbulence is a characteristic of the flow and not of the fluid. For example, turbulence flows are highly irregular, rotational – they have three-dimensional vorticity –, are dissipative and diffusive, and transport energy from large-scale eddies to small-scale. The term “turbulence” has been used in reference to fluid motions since Leonardo Da Vinci (1452 – 1519), who illustrated a turbulent flow with many co-existing vortices of different sizes (Figure 1.1a). The co-existence of eddies of a wide range of scales in nature is also illustrated in "The Starry Night" (Figure 1.1b) by Vincent Van Gogh (1853 – 1890). In this specific painting, we see many eddies of different sizes in the atmosphere. But, the same configuration can also be observed in the oceans. However, understanding the oceanic physical processes that reach from the large scale to the small scale turbulent flow are not fully understood.

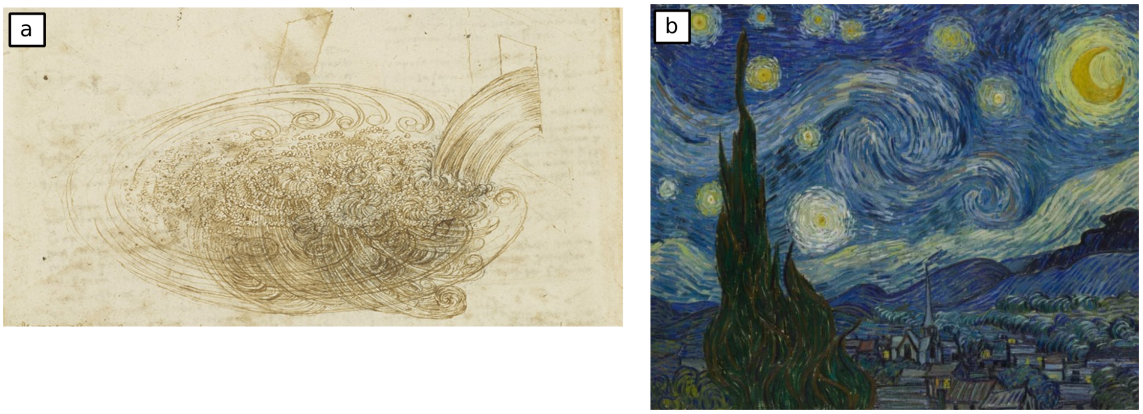

Figure 1.1: (a) : A turbulent cascade as seen by Leonardo da Vinci. Reproduced from Kemp (2019). (b) "The Starry Night" is an oil on canvas painting by Vincent van Gogh (1889). It has been in the permanent collection of the Museum of Modern Art in New York City

Among the many scales of ocean movement is a class of phenomena called submesoscale. The aforementioned class of motion scale is related to the familiar mesoscale eddies that contain the majority part of kinetic energy in the ocean (McWilliams, 2016). Eddies at mesoscale transfer energy toward larger scales by an inverse cascade (Charney, 1971). Thus, they do not afford an intuitive route of energy toward dissipation scales passing through the submesoscales. On the other hand, to achieves the climate equilibrium, the dissipation of kinetic energy, which occurs at the turbulence scale, is required (e.g., McWilliams, 2016). Thus, the understanding of the submesoscales is crucial to bridging the meso and smaller scales.

The submesoscale is characterized by $\mathcal{O}(1)$ Rossby number dynamics. That means that advective terms from the Navier-Stokes equation are not negligible as in the mesoscale geostrophic flows. The submesoscale dynamics is not appropriately described by the quasi-geostrophic theory usually applied to mesoscales (Thomas et al., 2008). Moreover, the Richardson number (Miles, 1961), which reveals the stabilizing influence of the stratification over the destabilizing influence of the vertical shear on the flow, assumes intermediate values at the submesoscales. And at the mesoscales, the stratification dominates, and the Richardson number is large. Therefore, as the vorticity and the shear

enhances at the submesoscales, energy is removed from the dominant geostrophic flows. That results in the transference of energy toward smaller scales and is irreversibly lost.

Measurements of properties characterizing submesoscale and smaller-scale processes in the oceans are still challenging and too sparse. This is the main reason for the late discoveries of these oceanic movements and their roles in general circulation. Today, with the advancement of technologies, the oceanographic instrumentation can sample processes on smaller scales. This helps in a better understanding of oceanic phenomena and their relationships. However, there is still much to be discovered, measured, and finally, incorporated into climate models so that in this way, the forecasts of future scenarios are increasingly accurate.

The present dissertation is aimed at addressing the mechanisms that remove energy from the dominant balance in the western South Atlantic Ocean, permitting the forward energy cascade towards dissipation scales. Despite the high activity of ageostrophic processes at the boundary layers, we focus here, along with the independent, although intrinsically related, following chapters, the presence of such mechanisms in the interior ocean. The dissertation is organized as follows. In Chapter 2, we address the dissipation of energy generated in the subsurface due to the reverse flow of the poleward Brazil Current and the equatorward Intermediate Western Boundary Current. The magnitude of turbulent kinetic energy dissipation along the interface of the reversal flow reveals the importance of mixing on the vertical tracer exchanges. In Chapter 3, we capture, for the first time in the western South Atlantic Ocean, two adjacent subsurface vortices at submesoscales wandering near the Vitória-Trindade Ridge. From a high-resolution thermohaline and velocity dataset and microstructure profiles, we estimate their dynamic regime and the amount of energy dissipation. In Chapter 4, we simulate the ocean circulation around the

Vitória-Trindade Ridge to verify if this kind of subsurface vortex could be locally generated owing to the influence of the shallow banks, seamounts, and islands from the Ridge. Finally, in Chapter 5 we present the concluding remarks from all the independent chapters present in the current dissertation.

CHAPTER 2.

ON THE ROLE OF TURBULENT MIXING PRODUCED BY VERTICAL SHEAR BETWEEN THE BRAZIL CURRENT AND THE INTERMEDIATE WESTERN BOUNDARY CURRENT

Manuscript published on January 2020, in the *Journal of Geophysical Research: Oceans*. This manuscript is co-authored by Dante C. Napolitano, Ilson C. A. Silveira, Amit Tandon, Daniel G. MacDonald, Rafael A. Ávila and Paulo H. R. Calil

DOI: 10.1029/2019JC015338

Abstract

An intensification of the vertical shear is observed below the surface mixed layer at 21° S due to the mutually opposing flows of the Brazil Current (BC) and the Intermediate Western Boundary Current (IWBC). The propensity to develop turbulence and mixing due to vertical shear over intense stabilizing density gradients is an important characteristic of such environments. For the first time, microscale measurements were made in the BC-IWBC system, providing direct quantitative values of the turbulent fluctuations. Peaks of relative strong dissipation rates of turbulent kinetic energy (TKE) (O(10^{-8}) W kg^{-1}) were observed close to the base of the surface mixed-layer. On the other hand, prominent peaks of TKE dissipation rates of up to two orders of magnitude higher than the background were observed at deeper levels, where stratification begins to lose intensity. Analyzing such peaks, caused by intense vertical shear or weak stratification—and sometimes both—, allows a characterization of the local mixing processes and the role played by vertical exchanges of biogeochemical properties. Based on the estimated nitrate gradient and the vertical diffusivity, we show that turbulent mixing driven by vertical shear plays an important role in the supply of nitrate to the upper layer.

Introduction

The Brazil Current (BC) is the western boundary current that closes the South Atlantic Subtropical Gyre. It is unique among poleward-flowing western boundary currents in that its vertical structure changes along its extent (Boebel et al., 1999; Stramma and England, 1999). The BC originates from the bifurcation of the surface branch of the South Equatorial Current (SEC) around 15° S (Soutelino et al., 2011). Between its origin and approximately 20° S, the BC is an eddy-dominated, mixed-layer jet transporting Tropical Water (TW) in the upper 200 m of the water column (Soutelino et al., 2011). 21° S marks the latitude of the South Atlantic Central Water (SACW) flow bifurcation at the pycnocline, where this nutrient-rich and less salty water mass feeds the BC in its poleward flow. Below the pycnocline, the equatorward flow of the Intermediate Western Boundary Current (IWBC) is formed due to the bifurcation of the colder, fresher and nitrate-richer Antarctic Intermediate Water flow (AAIW; Boebel et al., 1999). Between 26–21° S, the IWBC interacts with the poleward flow of the BC, enhancing the vertical shear and property gradients. According to Silveira et al. (2004), the BC-IWBC system is a baroclinic current system with a single distinct flow reversal between the upper and intermediate portions of the continental slope. The reverse flow of the BC-IWBC in the upper 400 m enhances the vertical shear in the interior ocean and may dissipate energy through small-scale processes such as vertical mixing. Mixing in this region is one of the least understood physical processes that may control stratification, primary production, and carbon exchanges, as well as heat and dissolved material (nutrients) exchanges through diapycnal transport (Gregg, 1987). A better knowledge of turbulent processes, including the dissipation of turbulent kinetic energy (TKE), is fundamental to our under-

standing of ocean mixing and the distribution of heat, salt and biogeochemical components in the ocean (Gargett, 1997).

Ocean circulation is characterized by a wide range of scales of motion, and its main energy sources are well known (Ferrari and Wunsch, 2009). The work of wind stress on the surface of the ocean is the primary source of energy input to the ocean. Although relatively small compared to wind stress, the effects of heating (cooling) and precipitation (evaporation) are also relevant. On the other hand, the sink of energy and its mechanisms are far less well understood (*e.g.*, D'Asaro et al., 2011). To achieve energy dissipation, a forward cascade of energy is required from motions ranging from ocean-basin scales to the viscous, centimeter scales (*e.g.*, D'Asaro et al., 2011). Instabilities of the large-scale circulation lead to the generation of mesoscale eddies, which are commonly recognized from satellite altimetry and quasi-synoptic hydrographic data, and may be simulated by numerical models with relatively coarse spatial resolution; on submesoscale, stirring and straining by eddies and filaments of order 1–10 km in the mixed-layer may invoke secondary instabilities (*e.g.*, Nagai et al., 2008); from this stage on, these secondary instabilities can evolve down the forward energy cascade, leading ocean-basin scale to the viscous, centimeter-scale motions and ultimately energy dissipation (McWilliams, 2016). However, observations of smaller-scale processes, mainly on dissipation scales (*i.e.*, the small-scale end of the turbulent cascade Kolmogorov, 1968) are scarce and, until now, nonexistent in the BC-IWBC domain.

Different mechanisms can extract energy from geostrophic flows through baroclinic instabilities and transfer it to unbalanced motions, from where it may be cascaded to the smallest scale (Ferrari and Wunsch, 2009; Nikurashin and Ferrari, 2011; Nikurashin et al., 2013). According to Zhai et al. (2010), western boundary regions are recognized

as a sink site for the westward-propagating ocean eddies, dissipating a great amount of energy in mid-latitudes. The interaction of a flow over rough topography can promote strong dissipation of turbulent energy, enhancing the mixing in the interior ocean (Polzin et al., 1997; Munk and Wunsch, 1998; Ledwell et al., 2000; Kunze et al., 2006). Recent literature suggests that fronts and mixed-layer instabilities, characterized by intense density gradients and vertical shear of the horizontal velocity component (Boccaletti et al., 2007; Thomas et al., 2008; Mahadevan et al., 2010; Thomas et al., 2013; Ramachandran et al., 2018), are also possible routes of energy dissipation (Molemaker et al., 2010).

Stratified-shear conditions occur in many ocean environments such as thermal/salinity fronts (*e.g.*, Ramachandran et al., 2018), wind-driven flows (*e.g.*, Gregg, 1989), and in opposing flows such as the BC-IWBC, as in the present study. The propensity to develop turbulence and mixing due to vertical shear over intense density gradients is an important characteristic of these environments. Turbulence and mixing can be generated when the destabilizing influence of shear overcomes the stabilizing influence of stratification, which is revealed by the Richardson number ($Ri = N^2/S^2$, where $N^2 = g\rho_0^{-1}\partial\rho/\partial z$ is the stratification, and $S^2 = (\partial u/\partial z)^2 + (\partial v/\partial z)^2$ is the shear squared intensity). The shear instabilities develop leading to turbulence if the ratio between these quantities is equal or less than a quarter (Miles, 1961). The local value of Ri in the ocean (measured in orders of magnitude) may be a useful guide to the factors leading to turbulence and can provide a means to quantify mixing (Thorpe, 2007). The generation of turbulence is frequently associated with Kelvin-Helmholtz instabilities (Thorpe, 1973). These instabilities are defined by a billow of stratified fluid that may decay into turbulence and become well-mixed (Gregg, 1987). According to Gregg (1987), a perturbation in a stratified-shear condition such as the passage of a storm (*e.g.*,

Rumyantseva et al., 2015) can evolve into a roll-up of stratified fluid until it overcomes the buoyancy force and the feature collapses into disorganized motions. The last stage of this is turbulence, and earlier stages are considered preturbulent stages (*e.g.*, MacDonald et al., 2013).

Turbulence observations near the Kuroshio Current suggest that, on the cyclonic side of the jet at the pycnocline (Nagai et al., 2009) and also at the surface of the ocean (D'Asaro et al., 2011), strong dissipation of TKE is associated with frontogenesis (*e.g.*, Hoskins and Bretherton, 1972) and symmetric instability (*e.g.*, Hoskins, 1974). Kaneko et al. (2012) investigated the turbulence structure across the Kuroshio focusing on the difference between dissipation values near to and far from the front. The mean of the turbulent energy dissipation rate was higher near fronts on both cyclonic and anti-cyclonic sides. However, on the cyclonic side, a strong vertical shear with higher dissipation rates was observed, where large density gradients were consistent with turbulence enhancement due to frontogenesis. Beyond the physical importance of the turbulent field, it has an essential role over the biogeochemical properties exchanges. The nitrate turbulent flux promotes the high concentration of chlorophyll-a across the Kuroshio (Kaneko et al., 2013), and can supports up to 50% of the primary production in the Great Australia Bight (Doubell et al., 2018). Interior regions of high energy dissipation due to the interaction with topography and in the upper ocean are of great interest for their potential contribution to the energy budget of the general circulation, in the maintenance of the stratification, and in the exchange of (in)organic compounds that may explain the increase in primary productivity. Turbulence occurring in the upper sunlit layer of the ocean is increasingly recognized as critical to the functioning of the marine food web (Gargett, 1997).

Here, we investigate turbulent mixing processes in the stratified-shear flow of the BC-IWBC at 21.6° S. Our specific questions are: i) can the mutually opposing flows of these western boundary currents modulate vertical turbulent mixing? and ii) what magnitude of property exchanges is driven by small-scale processes? To address these questions, we perform a mixing experiment at the BC-IWBC system, sampling for the first time the microstructure of this shear-stratified environment, down to approximately 400 m, and capturing the BC-IWBC interaction (Section 2). In Section 3, we outline a potential vorticity analysis to better understand the local dynamics at mesoscale of this shear-stratified flow. The results of the TKE dissipation rates as well as vertical diffusivities and nitrate flux are given in Section 4. The discussion and the concluding remarks are posed in Section 5.

The BC-IWBC Mixing Experiment

The BC-IWBC experiment was designed to study the interaction of the BC with the reverse flow of the IWBC underneath it. South of 21° S, where the BC acquires a typical western boundary current structure, an oceanographic survey was conducted during the austral winter (August) of 2017 aboard the *R/V Alpha-Crucis* to obtain a vertical section across the BC. This study discusses the results of a zonal vertical section at 21.6° S (Figure 2.1a) from the surface to 400 m depth, where it is possible to observe the poleward flow of the BC within the mixed-layer and the equatorward flow of the IWBC below the pycnocline (Figures 2.1b and 2.1c).

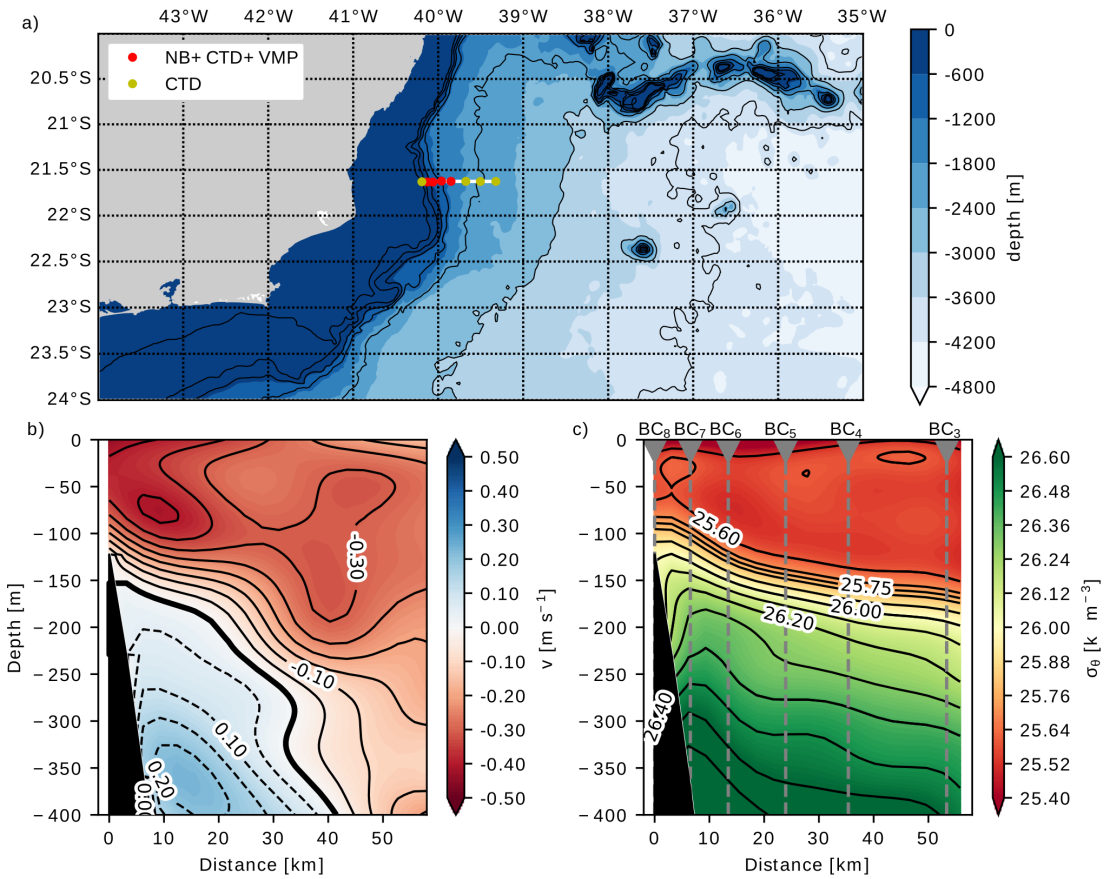

Figure 2.1: a) Station map with bathymetry from ETOPO (Smith and Sandwell, 1997) in the background (colors). Black solid lines are the isobaths. Red dots represent the stations where the VMP, CTD, and Niskin bottles were deployed. Yellow dots represent the station where only the CTD was deployed. The white line represents the track of the ship continuously measuring velocity with the ADCP. b) Vertical section of the meridional velocity estimated by the objective analysis (colors). Solid black lines represent negative isotachs, while dashed black lines represent the positive isotachs. Isotach of zero velocity is depicted as the thick solid black line. c) Vertical section of potential density (σ_θ) estimated by the objective analysis (colors). Black contours represent the isopycnals, and vertical gray and dashed lines represent the locations of the stations with their names at the top.

Velocity was continuously measured in a cross-section of the BC-IWBC system with a Vessel-Mounted Acoustic Doppler Current Profiler (VM-ADCP, RDI - 75 kHz) in 8 m bins, and data were primarily processed by CODAS (Common Ocean Data Access System) software, following the guidelines of Firing (1995). To retain higher quality results, data below 60% of the returned signal (the so-called "percent good") were excluded. Hydrographic data were obtained with a Seabird CTD - Rosette with 24 Niskin bottles. Water samples for nutrient analysis were collected every 25 m down to 400 m depth, with

the determination of nitrate concentrations performed using an autoanalyzer, following the modified Grasshoff method (Grasshoff et al., 2009). The quasi-synopticity of the samples was guaranteed by the positions of the 8 oceanographic stations, determined by the local baroclinic radius of deformation.

Turbulent parameters were estimated from measurements of the shear variance at four stations (Figure 2.1a) crossing the BC-IWBC using a vertical microstructure profiler from *Rockland Scientific* (VMP - 250) operating at 512 Hz. The VMP was equipped with two shear probes, one SBE7 micro-conductivity probe, and one FP07 thermistor. During the free-falling profile, shear variance, conductivity, and temperature were measured. The VMP operated in downcast mode, with speeds varying between $1.4\,\mathrm{m\,s^{-1}}$ near the surface and $0.2\,\mathrm{m\,s^{-1}}$ near the maximum profiled depth. For statistical reliability, two VMP casts were performed at each station. Details about turbulence measurements and its calculation are given in Section 4.

The Mesoscale Field

The estimation of the turbulent parameters (dissipation of TKE, vertical diffusivities, and vertical turbulent fluxes) was the main focus of the experiment. Nevertheless, a description of the mesoscale field is an important framework for interpreting these measurements of turbulence. An objective analysis was conducted to estimate the background mesoscale field of the meridional component (v) of the velocity (Figure 2.1b) and potential density (σ_θ; Figure 2.1c). The same correlation lengths ($\Delta x = 30\,\mathrm{km}$, $\Delta z = 100\,\mathrm{m}$) were used in both fields to reduce the error associated with different scales of the quantities in dynamic calculations, such as potential vorticity.

The selected experimental site presents a unique vertical structure among western boundary currents. Just south of 21° S, the BC begins to acquire characteristics of a western boundary current. However, the BC sampled at 21.6° S is still a surface mixed-layer (SML) jet, confined within the upper 100-150 m of the water column (Figure 2.1b). The SML depth is defined as the depth at which potential density is 0.125 kg m^{-3} greater than the potential density value at the surface de Boyer Montégut et al. (2004). The isotachs of the lower BC (Figure 2.1b) follow the high stratification layer,

$$N^2 = \frac{\partial b}{\partial z}, \tag{2.1}$$

where the buoyancy is

$$b = -\frac{g}{\rho_0}\sigma_\theta. \tag{2.2}$$

In Figure 2.1c, the sloped, western boundary currents isopycnals flatten toward the offshore direction. At intermediate levels, the equatorward flow of the IWBC opposes the poleward flow of the BC. This reverse flow creates an intense vertical shear (Figure 2.2a) within the higher stratification layer (Figure 2.2b) setting up a stratified shear flow environment.

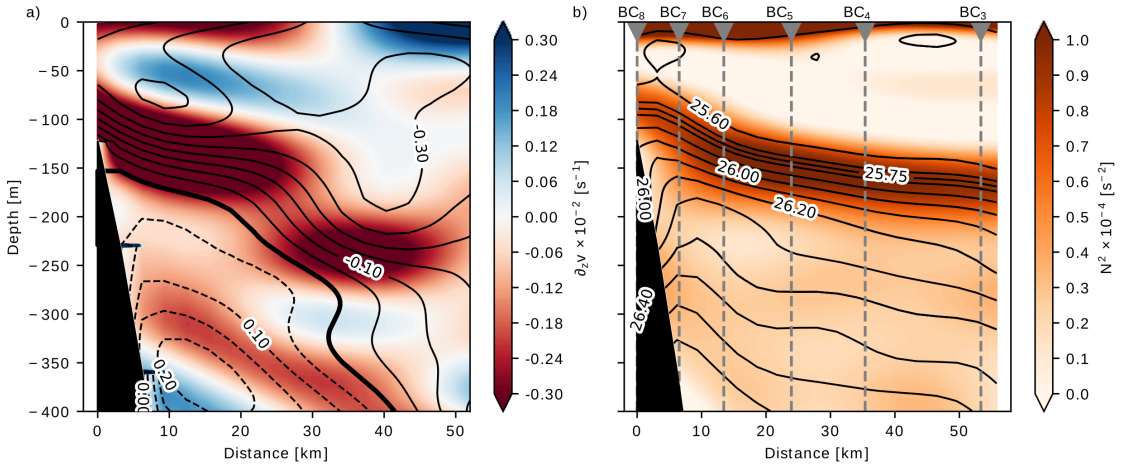

Figure 2.2: a) Vertical section of the vertical shear of the meridional velocity (colors) with contours of negative (solid black lines) and positive (dashed black lines) isotachs. b) Vertical section of the stratification (colors) with isopycnals contours. Vertical dashed gray lines show the location of the oceanographic stations.

A potential vorticity (hereafter PV) analysis is an indicative tool of the capability of the system to develop instabilities (Thomas et al., 2008; D'Asaro et al., 2011; Thomas et al., 2013). Here, a two-dimensional PV section (*e.g.,* Thomas et al., 2016; Ramachandran et al., 2018) is evaluated from the objective field, assuming that along-stream variations of quantities are negligible. However, these gradients could be significant, refuting the approximation of two-dimensional PV (see details in Thomas et al. (2016); Ramachandran et al. (2018)). The Ertel PV is given by the equation

$$q = (f\hat{k} + \nabla \times \mathbf{u}) \cdot \nabla b, \tag{2.3}$$

where f is the planetary vorticity, $\hat{k}$ is the unit vector, and $\mathbf{u} = (u, v, w)$ is the 3D velocity vector. Given the assumptions described above, the 2D version of Eq. 2.3 is

$$q \approx \left(f + \frac{\partial v}{\partial x}\right) N^2 - \frac{\partial v}{\partial z}\frac{\partial b}{\partial x}. \tag{2.4}$$

According to Thomas et al. (2016), (2.4) is expressed by a sum of two constituents that emphasizes the contrasting roles of vertical vorticity/stratification and baroclinicity. The scaled PV,

$$q \approx \frac{\left[\left(f + \frac{\partial v}{\partial x}\right) N^2 - \frac{\partial v}{\partial z}\frac{\partial b}{\partial x}\right] f}{\overline{f^2 N^2}}, \tag{2.5}$$

where the overbar denotes spatial averaging, is outlined in Figure 2.3.

No negative PV values are observed below the SML and below the pycnocline, where the IWBC flows (Figure 2.3a); $q < 0$ within the SML could suggest a specific type of SML instability (*e.g.*, Thomas et al., 2013). However, the spatial resolution of the dataset and the smoothing due to the objective field do not allow the diagnosis of these processes. However, the spatial resolution of the dataset and the smoothing due to the

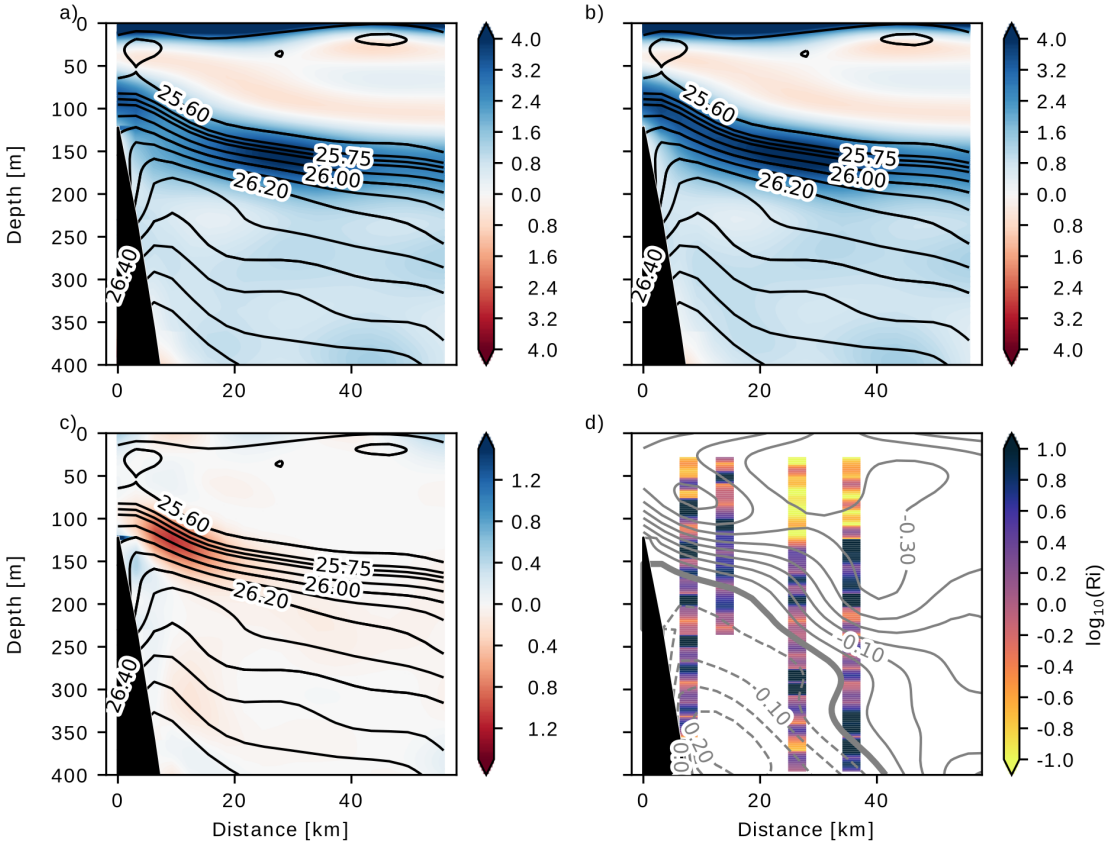

Figure 2.3: Vertical sections of a) the scaled potential vorticity (total), b) the scaled vertical vorticity/stratification term, and c) the scaled baroclinicity term. Black contours represent isopycnals. Panel d) is the 8m Richardson number (Ri) with contours of negative (solid lines) and positive (dashed lines) isotachs.

objective field do not allow the diagnosis of these processes. On the other hand, one considerable patch of relative low PV is observed within the upper stratified layer ($x \approx 5 - 15$ km, $z \approx 80 - 160$ m in Figure 2.3a), as well as low PV values occur below the pycnocline. Vertical stratification and total vorticity, dominate the cross-section structure below the SML. PV values close to zero are observed below the pycnocline (Figure 2.3b), meaning that low relative vorticity and reduced stratification may increase the potential for the development of baroclinicity-driven instabilities. The second term, which accounts for the horizontal buoyancy gradient and the vertical shear, shows an intense patch of negative values (Figure 2.3c). This patch of relatively high baroclinicity is confined to the

stratified layer. If the magnitude of the baroclinicity term is higher than the magnitude of the vertical vorticity/stratification, the water column should develop some instabilities.

The reduction of the PV values, as a consequence of the interaction between two strong flows, makes the flow to be in a dynamical regime marginally stable prone to instabilities. The 8 m Richardson number profiles (Ri hereafter) are sometimes close to Miles instability criterion and, also close to 1 even over the stabilizing effect of the stratified layer (Figure 2.3d). It can be an indicator of the formation of small-scale turbulence driven by the vertical shear of the local reversed flow (*e.g.*, Balsley et al., 2008; Taylor and Ferrari, 2009). Previous studies conducted by Silveira et al. (2008) and Rocha et al. (2014) suggest that the BC-IWBC is baroclinically unstable since the horizontal vorticity gradient changes sign in the region. This criterion for baroclinic instability is also evident (not shown) in the present study. However, the competition between shear and stratification as depicted by the Ri profiles suggest a potential to develop shear instabilities, and eventually enhanced small-scale dissipation and mixing. To elucidate the role of the vertical shear in the generation of turbulence in the region, microstructure vertical shear fluctuations along the zonal section are analyzed in Section 4.

Turbulence observations

Dissipation Analysis

In this study, dissipation rates of TKE are estimated using microstructure measurements. This technique for evaluating turbulence in oceanic flows has been employed in many previous studies (*e.g.*, Oakey, 1982; Lueck et al., 1983; Moum and Osborn, 1986; Itoh et al., 2010; Kaneko et al., 2012). Microstructure analysis relies on high-frequency

measurements to directly quantify turbulent fluctuations. TKE dissipation rates (ε) are estimated from the MATLAB toolbox provided by Rockland Scientific, which is based on the theory and techniques proposed in the literature (Oakey, 1982; Gargett, 1997; Gregg, 1999; Wolk et al., 2002). The microscale shear variance is used to obtain ε from the integration of the spectrum of velocity fluctuations (Φ) for segments of the water column,

$$\varepsilon = \frac{15}{2}\nu\overline{\left(\frac{\partial u'}{\partial z}\right)^2} = \frac{15}{2}\nu\int_1^{k_{max}} \Phi(k)dk \; [W \; kg^{-1}], \tag{2.6}$$

where ν is the kinematic molecular viscosity and k_{max} is the maximum wavenumber determined by the Fast Fourier Transform (FFT) with 50% overlap for each vertical segment. The shear variance is computed by integrating the shear power spectrum from the lowest wavenumber k_1, set to 1 cycle per meter (cpm), to the highest wavenumber k_{max}, where the shear spectrum presents a minimum between the natural spectrum and a high wavenumber peak close to noise level. If the wavenumber of minimum energy is smaller than that corresponding to the Kolmogorov turbulent scale [$\eta = (\nu^3\varepsilon^{-1})^{0.25}$], the integration is extended to k_{max} along the Nasmyth spectral form (*e.g.* Oakey, 1982). In other words, ε is proportional to the area under the shear spectrum for homogeneous and isotropic turbulence. The spectral shapes of $\Phi(k)$ in the range below k_{max} agreed well with those of the Nasmyth spectrum (not shown), indicating small systematic error (Wolk et al., 2002). The dissipation rates were assumed reliable by the mean absolute deviation (MAD) of the spectra. Estimates of ε, whose MAD were higher than 0.4, were not considered (*e.g.*, McMillan et al., 2016). This parameter is the average absolute deviation between the measured spectrum and the Nasmyth spectrum (Ruddick et al., 2000).

The choice of the bin size to determine the highest wavenumber and its respective rate of dissipation of TKE is subjective and dependent on the fall speed of the equipment

(1.4 m s^{-1} close to the surface and 0.2 m s^{-1} at approximately 400 m). Given this subjectivity, a few bin sizes are tested to obtain the best combination of the number of values and reduction of noise. In Figure 2.4, segments corresponding to 2 s (1–6 m), 4 s (2–11 m), 6 s (3–16 m) and 10 s (3–25 m) are used to convert temporal derivatives to spatial derivatives, assuming a frozen field hypothesis as proposed by Taylor (1938). The smaller the water column segment, the more highly resolved is the TKE dissipation profile, but the greater

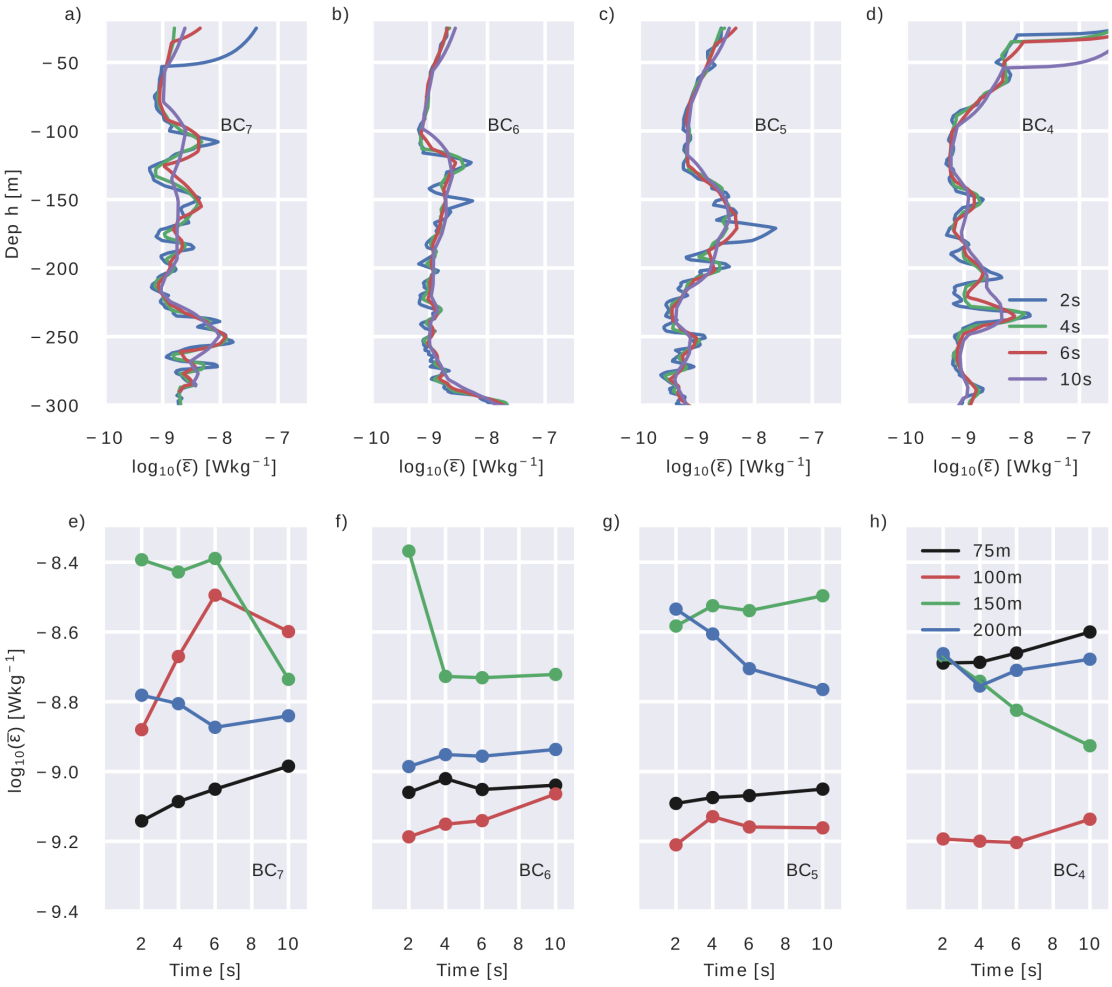

Figure 2.4: Panels are organized from left to right as a function of stations. Panels a and e represent station BC_7, b and f represent station BC_6, c and g represent station BC_5, and panels d and h represent the station BC_4. Panels a, b, c, and d represent the vertical profile of dissipation rates on logarithmic scales using 2 s (blue), 4 s (green), 6 s (red) and 10 s (purple). Panels e, f, g, and h represent the variation of dissipation rates among those segments at 75 m (black), 100 m (red), 150 m (green) and 200 m (blue).

is the noise carried by the signal (Figure 2.4). A combination of more highly resolved profiles (Figures 2.4 a-d) and the small difference between the magnitude of the dissipa-

tion rates at the same level (Figures 2.4 e-h) suggest that ε estimates from a bin size of 2 s provide the best results. Thus, the following results are derived from a bin size of 2 s.

The microstructure profiler is equipped with two shear probes giving duplicates of vertical profiles for each cast. In theory, both shear probes should measure the same microstructures with the same magnitude, though in reality, they present differences due to the sensitivity of each sensor. The contrasts in measurements of dissipation rates of TKE from the respective shear probes can be reduced by using the mean field of TKE dissipation rate estimates (*e.g.*, Doubell et al., 2018). The vertical profiles of ε of each

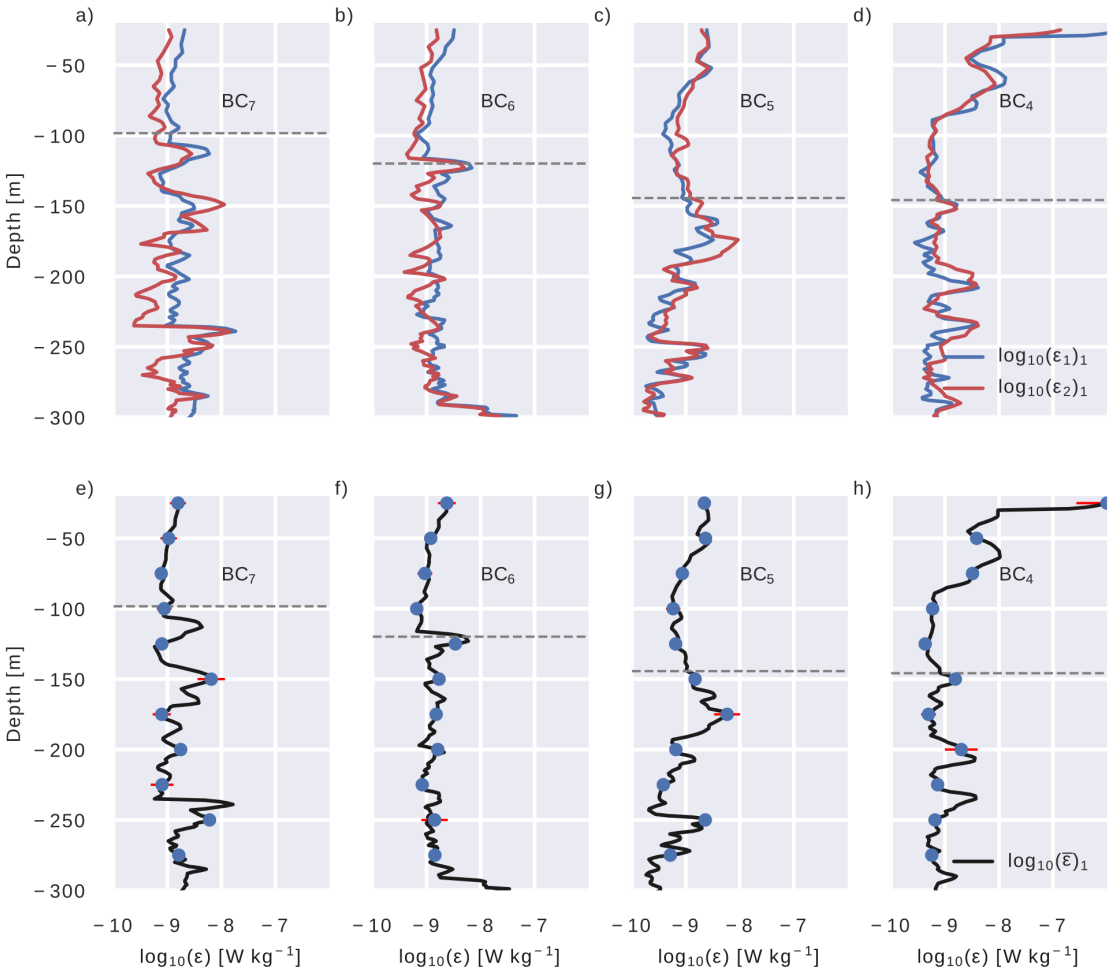

Figure 2.5: Panels a, b, c, and d show the vertical profiles of ε estimated from the shear probe 1 (blue) and 2 (red) from the first cast. Panels e, f, g, and h show the average profile of ε from the first cast with its respective error bar every 25 m (blue dots) (standard deviation, solid red line). The horizontal dashed gray lines represent the mixed-layer depth (MLD). The estimates depicted here were calculated with 2s intervals of the falling-probe in the water column.

shear probe show a similar vertical distribution of the turbulent motion peaks despite the difference between their magnitudes (Figures 2.5 a-d). Thus, employing the mean profile is satisfactory for the description of local turbulence (Figures 2.5 e-h).

As mentioned in Section 2, two VMP casts were performed at each station, resulting in two averaged profiles separated by approximately 30 minutes. This time interval is small compared to the turbulent time scale following the equation

$$\tau = T_{KH}(\partial v/\partial z), \tag{2.7}$$

where τ and T_{KH} represent the non-dimensional and dimensional Kelvin-Helmholtz billow evolution timescales, respectively, and $\partial v/\partial z$ is the ADCP cross-transect velocity vertical shear (MacDonald and Chen, 2012). The Kelvin-Helmholtz billow evolution timescales from the BC-IWBC are on the order of hours ($T_{KH_{min}} = 45$ min at the most sheared layer). Stationary turbulence could be expected, since the reverse flow is geostrophic. Thus, both casts are measuring the same turbulent feature, although peaks of ε may occur with a slight difference in depths at the same station. To avoid capturing peaks of ε at different depths due to the heaving of isopycnals – to filter the internal-wave signal –, ε is interpolated into an isopycnal coordinate (Figure 2.6). Now, peaks of ε appear at the same density range in both casts at each station, allowing the computation of the averaged profile of both casts, which is assumed to be a reasonable measure of the TKE dissipation rate at each station.

The composite mean of TKE dissipation rate at each oceanographic station shows thin subsurface patches of O(10^{-8}) W kg^{-1} with background values of O(10^{-10}) W kg^{-1} (Figure 2.7). Two (sometimes three) marked patches of ε are well-defined at each

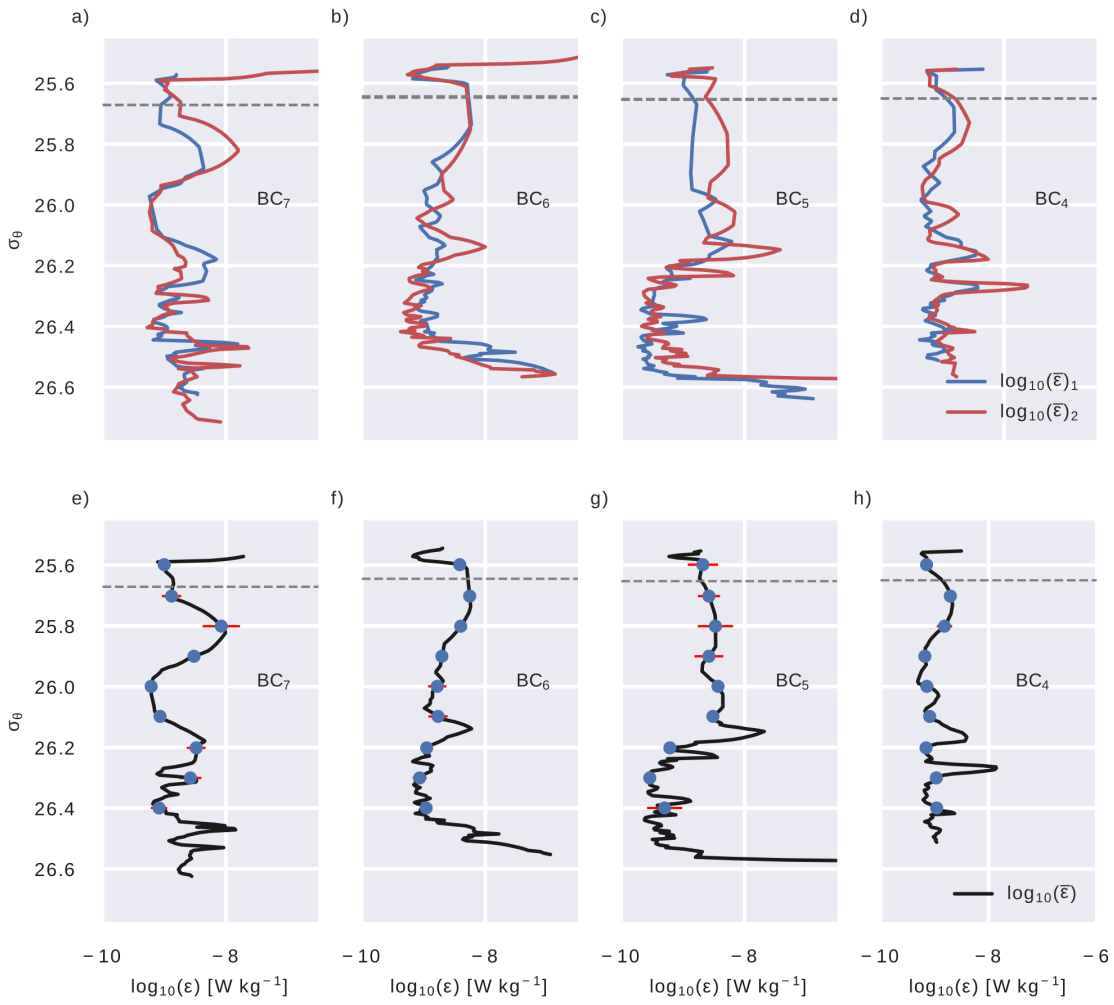

Figure 2.6: Panels a, b, c, and d represent the estimate of the TKE dissipation rates from the average of the first (red) and second (blue) casts; panels e, f, g, and h shows the average of ε and density estimate from both casts. The error bar (standard deviation, solid red line) are depicted for every 0.1 kg m^3 (blue dots). The dashed gray line in all panels represents the density at the MLD.

station. The first TKE dissipation rate peaks occur at the level of the SML depth and just below it. At station BC_7, the first peak reaches O(10^{-8}) W kg^{-1} following the highest stratification that occurs about 10 m below the lower limit of the SML, between 1025.7 kg m^{-3} and 1025.9 kg m^{-3}. The second peak of energy dissipation rate at station BC_7 reaches O(10^{-9}) W kg^{-1} and occurs between 1026.1 kg m^{-3} and 1026.3 kg m^{-3} at approximately 150 m. At the other three stations (BC_6, BC_5 and BC_4) (Figure2.7), the first peak of ε at each station is at the same density interval as the SML depth, and the second peak occurs also between 1026.1 kg m^{-3} and 1026.3 kg m^{-3}. It is important to note that

the base of the SML (peaks of ε) gets deeper in the offshore direction (Figure 2.5), following the stronger signals of vertical shear (stratification) (Figure 2.2). As the stratification becomes weaker below the SML, the magnitude of the vertical shear becomes stronger between 70 and 160 m in the western portion of the section and between 120 and 250 m in the eastern portion of the section. In turn, the zonal variation of the depth of greater vertical shear coincides with the depth of the BC and IWBC inversion.

In summary, the upper peaks of TKE dissipation rate coexist with strong stratification below the SML in the BC-IWBC domain (Figure 2.7). On the other hand, lower peaks of TKE dissipation rate are generally in the region of lower stratification but more intense shear due to the reversal flow. This relationship highlights the role of vertical shear in developing turbulent motions within the interface between the BC and the IWBC. Thus, small-scale processes at the pycnocline may generate turbulent mixing and provide exchanges of properties between the salty and nitrate-poor surface water and the fresher and nutrient-rich subsurface water mass of the western South Atlantic.

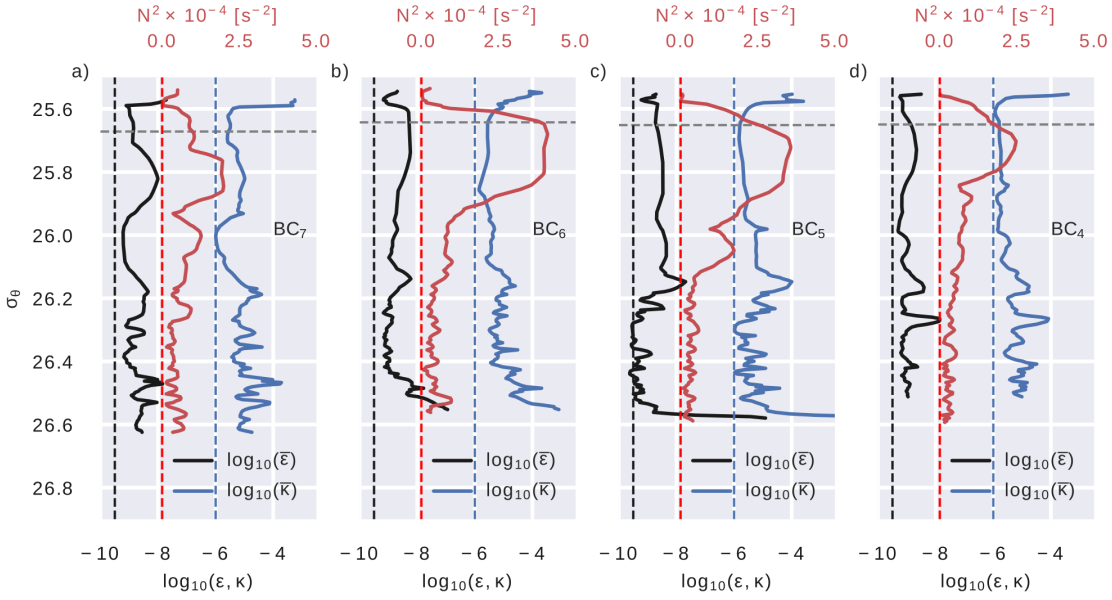

Figure 2.7: Vertical profiles of TKE dissipation rates (solid black lines), vertical diffusivity profiles (solid blue lines), and stratification profiles (solid red lines). Dashed gray, red, black and blue lines represent the density at the MLD, the zero of the stratification ($N^2 = 0$), the background value for TKE dissipation rates, and the background value for vertical diffusivity, respectively.

Mixing and turbulent vertical fluxes

A turbulent flow is diffusive and dissipative, which means that there is rapid mixing of fluid properties and kinetic energy is irreversibly lost through friction (Thorpe, 2007). The magnitude of the diffusivity in the interior ocean affects a wide range of processes, from the dispersion of non-conservative properties such as nutrients to the vertical transport of salt and heat, affecting ultimately the stratification of the water column. To verify whether or not the subsurface turbulence in the BC-IWBC domain may drive mixing processes at the interface of these two jets, the Osborn model (Osborn, 1980) is used to compute the vertical diffusivity (*e.g.*, Itoh et al., 2010; Kaneko et al., 2013; Doubell et al., 2018):

$$\kappa_\rho = \Gamma \frac{\varepsilon}{N^2}, \tag{2.8}$$

where $\Gamma = 0.2$ is the mixing efficiency parameter (Imberger and Ivey, 1991; Gregg et al., 2018). Turbulent diffusivity was also expressed in terms of the turbulence activity parameter ($\varepsilon/\nu N^2$), which exhibits a linear relationship at the stationary and intermediate turbulence regime (Shih et al., 2005).

Figure 2.7 shows that κ_ρ values within the SML are of O(10^{-4}) m^2 s^{-1}. These values decrease below the SML depth, where high stratification creates a physical barrier to vertical exchanges. Like the vertical distribution of TKE dissipation rates, peaks of vertical diffusivities, higher than the background values, are observed at the pycnocline. However, even with strong stratification, an intense relative vertical diffusivity O(10^{-5}) m^2 s^{-1} is observed at station BC$_7$ at density surfaces below the SML (Figure 2.7a). Below the pycnocline, multiple peaks of strong diffusivity are observed with orders of magnitude higher than the background, particularly close to the isopycnal 1026.2

$\mathrm{kg\,m^{-3}}$, where a burst of turbulence is observed. According to the turbulence activity parameter, the intermediate regime of turbulence dominates between the base of the SML and the 26.2 isopycnals (not shown). At those depths, vigorous patches of κ_ρ play an important role in the turbulent flux of conservative and non-conservative properties, which can be estimated from

$$F_c = -\kappa_\rho \frac{\partial C}{\partial z}, \tag{2.9}$$

where $\partial C/\partial z$ is the vertical gradient of a scalar property C (*e.g.*, Kaneko et al., 2013; Rumyantseva et al., 2015; Doubell et al., 2018).

Based on the higher values of turbulence observed below the SML, which are caused by the interaction of the nitrate-poor BC with the nitrate-rich IWBC, high levels of mixing and property exchange are expected near and below the pycnocline. Thus, we hypothesize that mixing at the interface of BC-IWBC may bring new nutrients (NO_3) to the upper ocean, promoting an increase in new production. To test this hypothesis, an estimate of the vertical turbulent nitrate flux (F_{NO_3}) was conducted based on Eq. (2.9). As the VMP was not equipped with a nitrate profiler, a density-nitrate relationship was built using the hydrographic data from the CTD and water samples from Niskin bottles for the lower half of the chlorophyll-a fluorescence maximum signal (Figure 2.8a). Chlorophyll-a fluorescence is the most commonly used index of phytoplankton biomass which is controlled primarily by the nutrient (nitrate) transport within the ocean (Sarmiento and Gruber, 2006). The density-nitrate relationship was applied to the microstructure-derived density to estimate the microscale vertical distribution of nitrate (*e.g.*, Sharples et al., 2007; Rumyantseva et al., 2015). One advantage of having a reliable density-nitrate relationship is that measurements of the nitrate gradient and turbulent diffusivity can be obtained via the same instrument at the same time. This avoids the uncertainties associated with spatio-

temporal differences that arise when the turbulent diffusivity and the nitrate gradient are obtained through different releases (Sharples et al., 2001, 2007). Following Sharples et al. (2007), Figure 2.8 shows the vertical level of the nitrate samples used to build the linear density-nitrate relationship. Using Eq. (2.9) and the microstructure-derived density data, the nitrate flux is estimated as

$$F_{NO_3} = -\kappa_\rho \frac{\partial NO_3(\rho)}{\partial z}. \tag{2.10}$$

Negative vertical gradients of nitrate appear throughout the whole water column. A prominent vertical gradient occurs between the SML depth and the isopycnal 1025.7 kg m^{-3}, which marks the upper level of the nitrate-rich subsurface water mass (Stramma and England, 1999). The value of the F_{NO_3} is estimated from the average of each quantity in Eq. (2.10) along the isopycnals that presented the highest peaks of turbulence. Figures 2.9a and 2.9c show the average of these quantities, as well as the average of N^2 and S^2 in the form of the bulk Richardson number (Ri_b)

$$Ri_b = \frac{\langle N^2 \rangle_\rho}{\langle S^2 \rangle_\rho}, \tag{2.11}$$

where $\langle \cdot \rangle_\rho$ denotes the average between the 1025.65 kg m^{-3} and 1025.75 kg m^{-3} isopycnals.

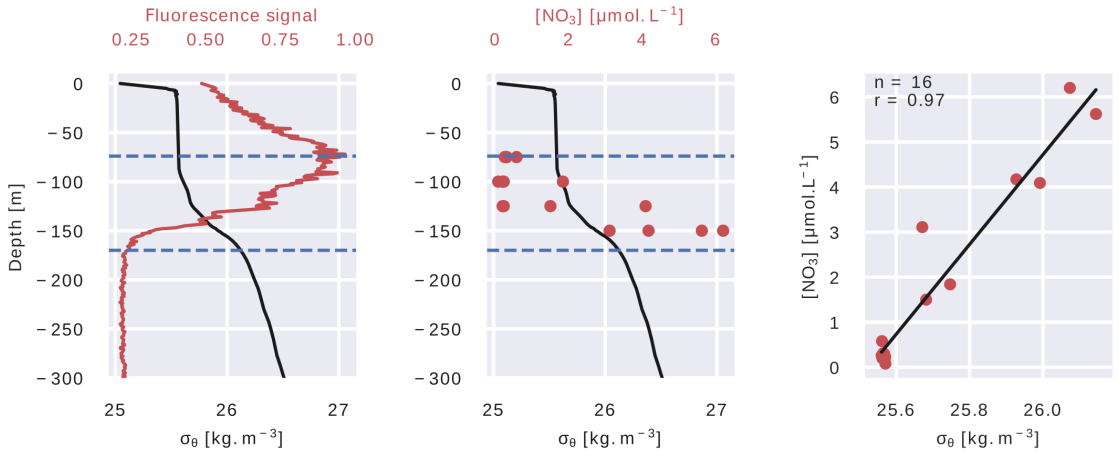

Figure 2.8: a) and b): The average density profiles (black) and the fluorescence signal from the CTD (red). Blue dashed horizontal lines delimit the lower half of the maximum fluorescence subsurface. Red dots represent the concentrations of nitrate. c) shows the scatter plot of the nitrate and density samples and its linear regression.

Shear (stratification) becomes weaker (stronger) in the offshore direction. The relation between the magnitudes of these two terms becomes clear when we look at the zonal variation of the Ri_b, which shows greater susceptibility to the development of instabilities in the stations to the west (Figure 2.9a). This pattern is followed by the magnitude of the vertical diffusivity, with higher values in the western portion of the section, resulting in more mixing. Westernmost stations are closer to the BC core—which contains the highest-shear layer, trapped between the SML depth and the zero isotach. Moreover, the nitrate gradient shows a maximum at station BC_6, producing a more intense turbulent flux (Figure 2.9c). Figures 2.9b and 2.9d show the average of terms of Eq. (2.10) and Eq. (2.11) for the density range of 1026.1 kg m^{-3} to 1026.2 kg m^{-3}, corresponding to the maximum dissipation of TKE. The variations in the average N^2 and S^2 are more subtle at the sub-pycnoclinic levels than at the pycnoclinic levels, *i.e.*, while the stratification remains approximately constant over the section, the vertical shear shows a slight decrease in its intensity in the offshore direction. On average, the Ri_b below the pycnocline is lower than the Ri_b into the SML depth triggering shear-instability, which in turn results in the strong vertical diffusivities at these density levels. In this case, the vertical nitrate gradient values were minimal, resulting in the pattern of zonal variation of the turbulent flux being similar to that of the diffusivity rates. Despite the small gradient of nitrate at deeper levels, the deep turbulent flux has the same magnitude of those acting on the main source of nitrate—the subsurface water— and in the lower limit of the SML.

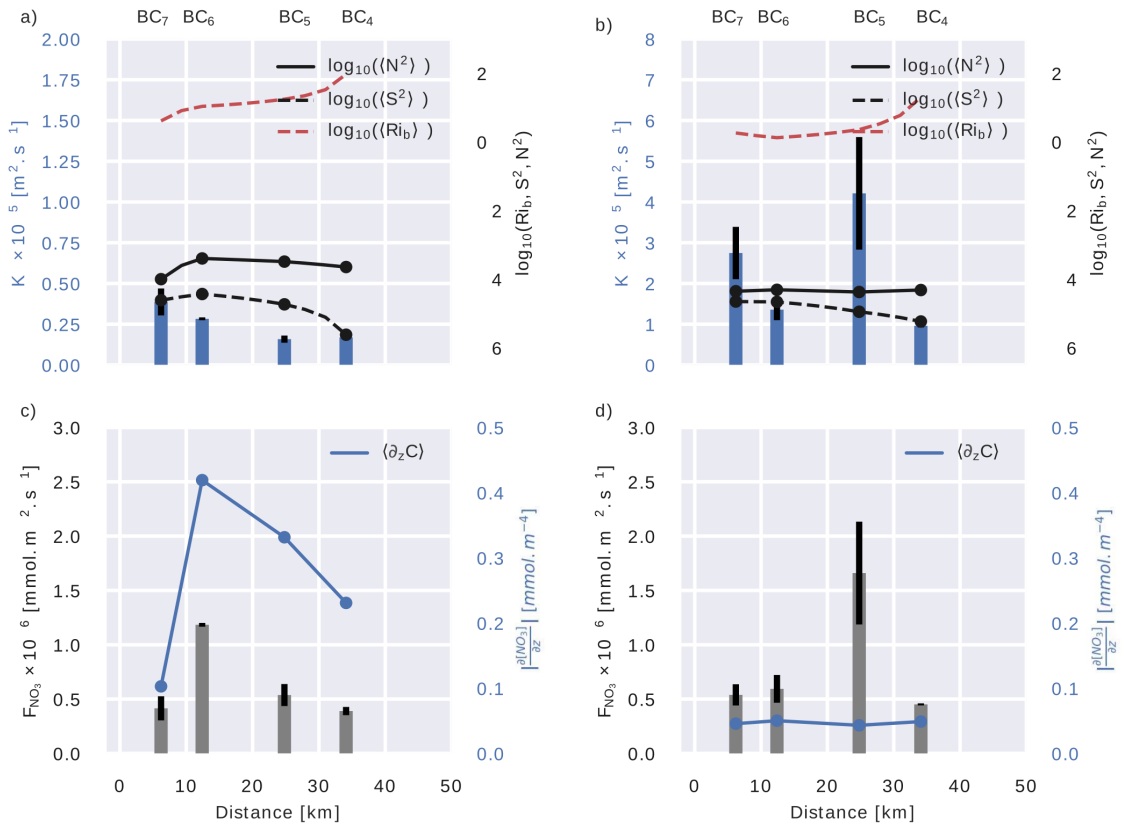

Figure 2.9: Vertical diffusivity (a;b) and turbulent nitrate flux (c;d) at pycnoclinic (a;c) and sub-pycnoclinic (b;d) levels. Blue bars in panels a and b represent the mean values of the vertical diffusivity between isopycnals of 1025.65 – 1025.75 kg m^{-3} (left) and 1026.1–1026.2 kg m^{-3} (right), while gray bars in panels c and d represent the mean of the vertical turbulent nitrate flux in the same intervals of density. Vertical black lines are the standard deviation of its respective quantities. Dashed red and black lines represent the zonal variation of Ri_b, and the vertical shear intensity, respectively. Solid black and blue lines represent the buoyancy frequency and vertical nitrate gradient, respectively.The bars represent stations BC_7, BC_6, BC_5 and BC_4, as indicated in the top.

Discussion and Concluding Remarks

In this study, microscale measurements in a region of interaction between the mutually opposing flows of two western boundary currents in the southwestern Atlantic Ocean are used to explore the role of the vertical shear on the mixing processes and nitrate exchange. Shear instabilities analysed from vertical microstructure observations

below the SML may drive an intense turbulent mixing activity, possibly supplying the upper ocean with new nutrients.

Instabilities of the upper ocean may occur on more refined horizontal scales (Mahadevan and Tandon, 2006) than that captured by the measurements during the BC-IWBC mixing experiment. However, at the measured scale, the destabilizing influence of the BC-IWBC shear overcomes the stabilizing stratification influence ($Ri \leq 1$). This tendency is further supported by the destabilizing effect of the baroclinicity. To evaluate the unstable water column motion further, horizontal high-resolution *in situ* data is required as well as the sampling of meridional variations of quantities assumed to be negligible in the present study. Nevertheless, previous studies conducted by Silveira et al. (2008) and Rocha et al. (2014) suggest that the BC-IWBC is baroclinically unstable. The flow structure measured in our section satisfies the baroclinic instability criterion, and in addition, the microstructure also shows that shear instability may also occur within the BC-IWBC system at finer vertical scales.

Instabilities in the upper ocean have an important role in the global energy budget, maintaining small-scale processes by the forward energy cascade. In the BC-IWBC mixing experiment, enhanced turbulent motions were observed at the isopycnals within the lower limit of the SML and underneath it. There, high vertical shear may erode strong stratification, resulting in a relevant peak of turbulence. According to Whitt and Taylor (2017), dissipation rates may remain elevated throughout the strong mean stratification and have important implications for the energy budget. Due to the attachment of the cores of the BC and the IWBC to the continental slope (Silveira et al., 2004), it is possible to see the zonal variation in depth of the turbulence signal, following enhanced vertical shear and the stratified layer as well as the SML depth (Figure 2.10). Nonetheless, weaker strat-

ification below the pycnocline combined with more intense vertical shear suggests greater mixing and potential for exchange of properties.

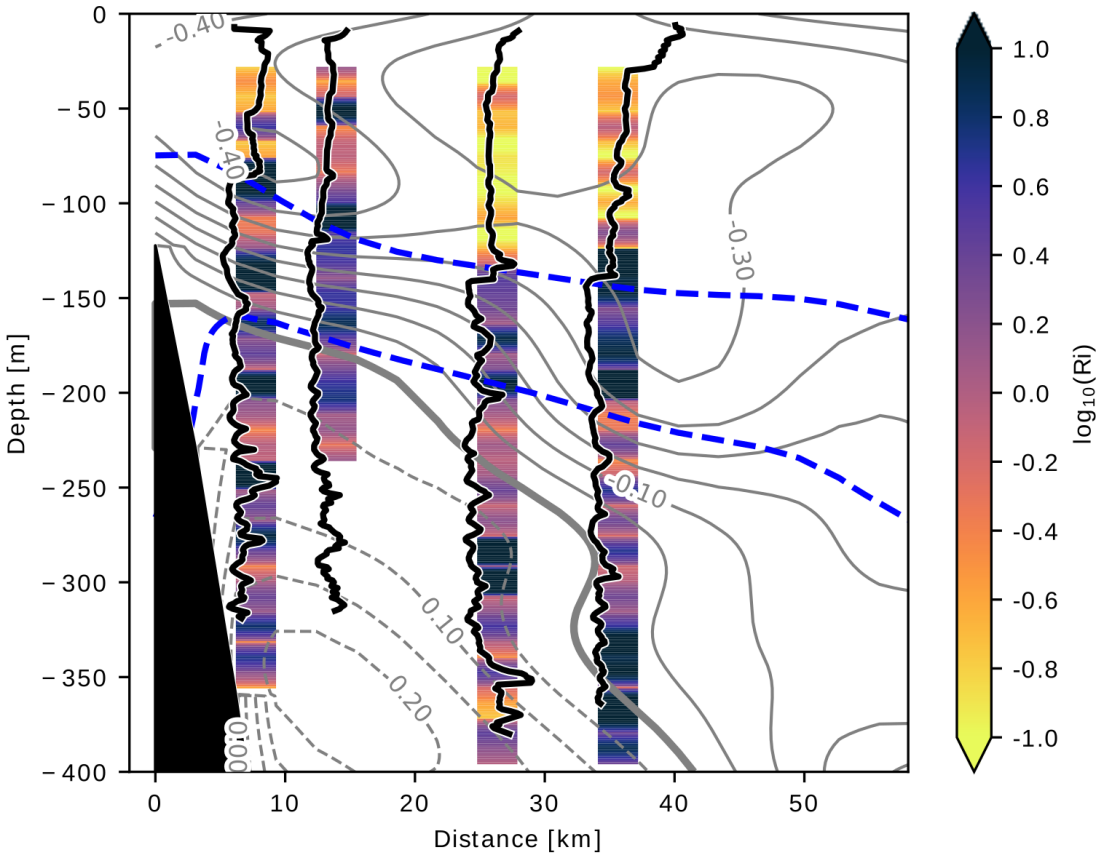

Figure 2.10: The background color represents the 8m Richardson number (Ri) with gray contours of negative (solid lines) and positive (dashed lines) isotachs. Dashed blue lines represent the isopycnals of the base of the SML (upper) and the isopycnal of 26.2 kg m^{-3} (lower). Black lines represent the vertical profiles of the vertical diffusivity on logarithmic scale.

Maximum values of vertical diffusivity of O(10^{-4}) m^2 s^{-1} were observed trapped in the SML by the high stratification in the lower SML. Moreover, values of O(10^{-5}) m^2 s^{-1} were observed below the pycnocline (Figure 2.7). This pattern agrees well with those obtained by (Dunckley et al., 2012), who tested different models for estimating vertical diffusivities. One of the most important points of the present study is the verification of strong vertical diffusivity occuring below the SML. Peaks of one order of magnitude higher than the background values emphasize the importance of the vertical shear under the weakly stratified condition. This relationship becomes clear when we

observe the zonal variation of turbulent diffusive processes, which agrees well with the Ri_b variation, evidencing the propensity of the flow to develop shear instabilities linked to the BC-IWBC interaction. The shear at the interface of this system may also be enhanced through internal waves (*e.g.*, Pereira et al., 2005). However, further studies should be conducted to reveal their role in producing turbulence since the observed amount of turbulence indicates stationary turbulence. Small-scale turbulence is an ubiquitous feature on the residual layer and is also shown to exist in regions with significantly larger Ri (Balsley et al., 2008). However, due to relatively weaker mixing at the isopycnal of the base of the SML, vertical turbulent nitrate flux occurs in a less expressive way, even in the presence of a stronger nitrate vertical gradient (Figure 2.9). Even with relative weaker mixing below the SML, it has the potential to bring nitrate to the upper layer. This implies a potential enhancement in primary productivity within an oligotrophic region. The magnitude of the nitrate flux observed in the present study is the same as that noted at the Great Australia Bight (Doubell et al., 2018) and in the southern side of Kuroshio front where low nitrate gradient was also observed (Kaneko et al., 2013). This mechanism can also be enhanced by the passage of an atmospheric system (Rumyantseva et al., 2015; Thomas et al., 2016), as well as by the net seasonal heat flux variability, not discussed in the present study.

Intense mixing near and below the pycnocline enhance turbulent fluxes and hence increase the upward supply of nutrients. However, unlike high nitrate vertical gradients close to the base of the SML, low nitrate gradients in deeper levels show comparable turbulent nitrate flux driven by the more intense mixing due to the BC-IWBC system. These deeper fluxes could prove more important with photosynthetically active radiation reaching these depths and should be investigated in future studies.

Acknowledgments

C.Z. Lazaneo acknowledges support from Coordenação de Aperfeiçoamento de Pessoal de Nível Superior - Brasil (CAPES) - Finance Code 001, and from Conselho Nacional de Desenvolvimento Científico e Tecnológico - CNPq (Processo 205857/2018-3). I.C.A. da Silveira acknowledges support from CNPq (grant number 307814/2017-3), Projeto SUBMESO (Processo CNPq 442926/2015-4) Projeto REMARSUL (Processo CAPES 88882.158621/2014-01), and Projeto VT-Dyn (Processo FAPESP 2015/21729-4). A. Tandon acknowledges support from NSF grant OCE1434512, OCE1558849, and OCE1755313. P. H. R. Calil acknowledges support from Projeto ILHAS (Processo CNPq 458583/2013-8). The authors are very grateful to the crew of *R/V Alpha Crucis* and, in particular, Captain José H. M. Rezende. C. Z. Lazaneo is greatful to Justine McMillan (Rockland Scientific) for her help with the microstructure data processing. We sincerely thank the anonymous Reviewer's for their comments which helped improve and clarify this manuscript. The data analyzed in this study can be obtained at https://jmp.sh/72IEgOV.

CHAPTER 3.

SUBMESOSCALE COHERENT VORTICES IN THE SOUTH ATLANTIC OCEAN: A PATHWAY FOR ENERGY DISSIPATION

Manuscript submitted in December 2020 and resubmitted in June 2021, to the *Journal of Geophysical Research: Oceans*. This manuscript is co-authored by Paulo H. R. Calil, Amit Tandon, and Ilson C. A. Silveira

Abstract

Mesoscale eddies propagate westward across the South Atlantic basin. As they reach the westernmost part of the basin, at approximately 20° S, they interact with a quasi-zonal seamount chain, the Vitória-Trindade Ridge. Flow-topography interaction is a primary candidate for the formation of subsurface coherent vortices such as those described in the present study for the first time in the VTR region. The two adjacent observed submesoscale coherent vortices present a marginally stable regime in their cores. This dynamic regime suggests small-scale turbulence cascading energy down to dissipation, which is diagnosed from turbulent kinetic energy dissipation estimates within one of the SCVs. The thermohaline signatures of each SCV reveal homogenized waters in their cores but with small thermohaline anomalies compared to the surrounding waters, suggesting a remote generation site. Here, we elucidate the role of such vortices cascading energy down to dissipation and speculate that they were possibly formed due to the eddy-topography interaction along the VTR and advected by the meandering South Equatorial Current to the location of field observations.

Introduction

The majority of the ocean's kinetic energy remains at mostly balanced mesoscale and large-scale flows. While geostrophically balanced eddies transfer energy to larger scales via an inverse cascade (Charney, 1971), different mechanisms can remove energy from geostrophic flows and transfer it to unbalanced motions at smaller scales. This forward cascade is modulated by submesoscale motions that act as a transition from the mostly two-dimensional, geostrophically balanced dynamics to the full three-dimensional flows where dissipation occurs (McWilliams, 2016; Thomas et al., 2008).

Among the processes that lead to submesoscale instabilities, flow-topography interaction can disturb the geostrophic balance. The incoming flow against the sloping topography develops highly asymmetrical vertical vorticity due to the bottom drag. The asymmetry of the vertical vorticity distribution, with anticyclonic dominance within isolated topographic wakes, induces centrifugal instability, leading to enhanced mixing and energy dissipation (Molemaker et al., 2015). Moreover, observations reveal the development of vortices due to flow-topography interaction in most of the world's oceans (D'Asaro, 1988; Molemaker et al., 2015; Vic et al., 2015; Srinivasan et al., 2017, 2019; Gula et al., 2016, 2019). The vorticity filaments merge into the topographic wake to eventually form submesoscale coherent vortices (called SCV hereafter, following McWilliams (1985)).

Such vortices, also called intrathermocline eddies (Dugan et al., 1982), are often described as swirl-like currents and are predominantly associated with distinct, convex-lens-shaped tracer anomalies (Frenger et al., 2018; Gula et al., 2019). The convex-lens-shaped anomalies are only for anticyclonic SCVs. Though less abundant, SCVs can also

be cyclonic (e.g., de Marez et al., 2020). The SCVs are characterized by radii smaller than the Rossby baroclinic deformation radius, with Rossby (*Ro*) and Burger (*Bu*) numbers of $\mathcal{O}(1)$ (McWilliams, 1985). Once formed, SCVs can wander in the interior of the ocean for many years (McWilliams, 2016), thus acting as important agents of tracer transport since they retain waters from their formation sites as they propagate as coherent structures.

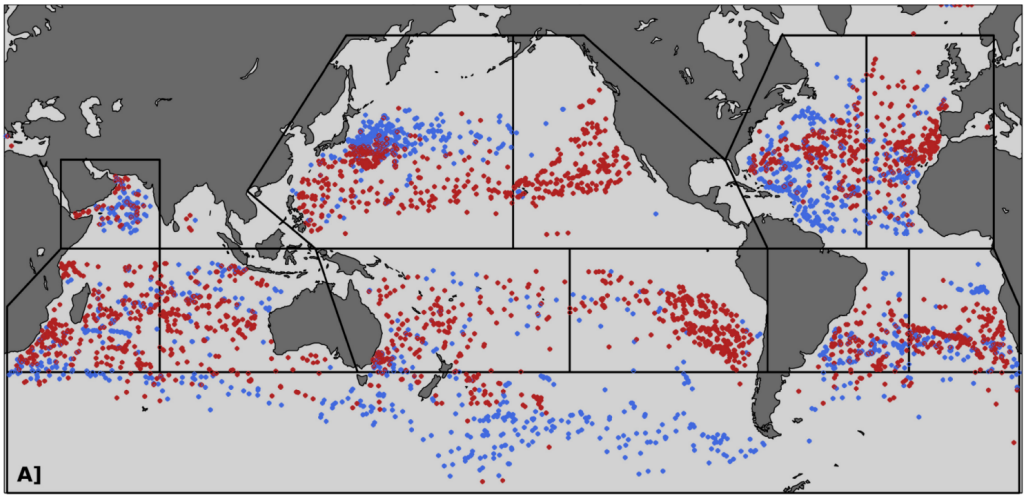

Figure 3.1: Locations of all spicy-core (red) and minty-core (blue) SCVs detected from Argo floats over the period of August 1997 to January 2020. From McCoy et al. (2020)

SCVs are present in all of the world's oceans (Figure 3.1, e.g., McCoy et al., 2020). Meddies, for example, are SCVs that flow from the Mediterranean Ocean, transporting a great amount of salt into the Atlantic Ocean (McDowell and Rossby, 1978). Puddies, which are SCVs typically formed in the eastern boundary poleward undercurrents, tend to maintain their coherence for hundreds of kilometers while propagating westward and feeding the subtropical gyres with nutrient-rich waters (Frenger et al., 2018). SCVs are also formed due to the interaction of boundary currents with topography as in the Beaufort Gyre (D'Asaro, 1988), the Charleston Bump and Cape Hatteras (Gula et al., 2019), and the Mid-Atlantic Ridge (Vic et al., 2018). Despite the widespread observation of SCVs, their generation mechanisms, as well as their role in the general ocean circulation, are still not fully known.

Most SCVs do not have a surface expression, and it is challenging to detect them due to their small horizontal scale (Assassi et al., 2016). They are usually either sampled by a single profile or observed by glider measurements or seismic images (e.g., Gula et al., 2019). Thus, observations at high spatial resolution, able to capture more than a single profile inside one of these features are still challenging. Since one of the generation mechanisms of SCVs is related to flow-topography interaction, the Vitória-Trindade Ridge (VTR) in the South Atlantic Ocean (Figure 3.2) may be a hotspot for SCV generation due to the presence of many shallow seamounts, banks, and islands (Alberoni et al., 2019) along the path of the Brazil Current, which is formed just a few degrees north of the VTR.

In order to search for signals of SCVs in the vicinity of the VTR, we conducted an oceanographic survey in the austral summer of 2017. In this work, we describe the structure of two anticyclonic SCVs observed near a shallow seamount, the Columbia Seamount, which is part of the VTR. We also present the turbulent regime inside one of the features. To the best of our knowledge, this is the first time microstructure measurements of mixing were taken inside an SCV.

The article is organized as follows. In Section 2, we present the data collection methods that allowed us to sample an SCV. In Section 3, we describe the vertical structure of two submesoscale coherent vortices near the VTR. In Section 4, we present the first microstructure measurements within one SCV observed in the real ocean. In Section 5, we address one of the possible regions of origin of the captured SCVs. Summary and concluding remarks are presented in Section 6.

The Ilhas 1 Survey Data Set

During the austral summer of 2017, we conducted an oceanographic survey (Ilhas 1) aboard the *R/V Alpha-Crucis* (University of São Paulo) as part of the "Islands" experiment in the vicinity of the VTR. The main purpose of this survey was to elucidate the role of seamounts in the generation of submesoscale features due to the interaction of the rich mesoscale eddy field with the local topography.

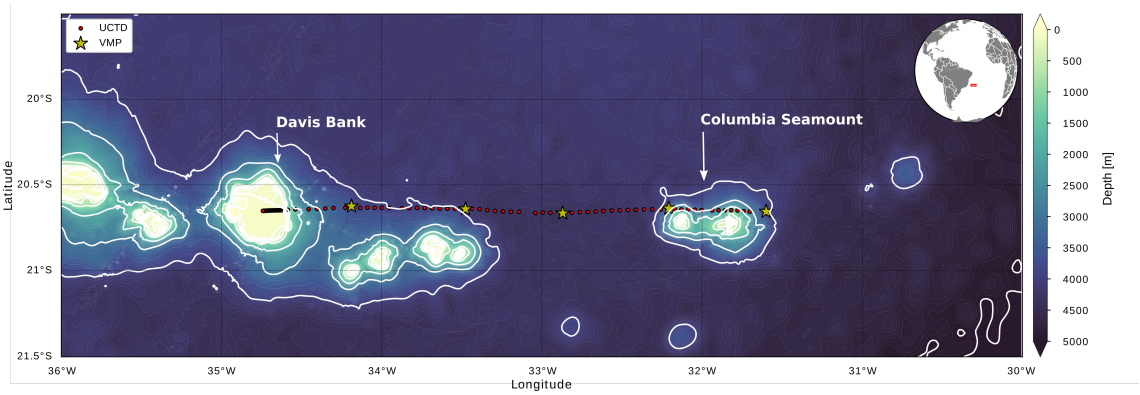

Figure 3.2: The Ilhas 1 austral summer survey. Map of the Vitória-Trindade Ridge region, with the light yellow shading representing depths shallower than 300 m. Red dots and yellow stars indicate the locations of UCTD and VMP stations, respectively. The thick white lines represent the 4000, 3000, 2000, 1000, 500, 250, 100, and 50 m isobaths. Long-time-averaged shipboard-ADCP velocities were measured along the transect beginning at the Davis Bank in the west, and ending at the Columbia Seamount.

The VTR is a quasi-zonal ridge that extends 1120 km from the Abrolhos shelf to the Trindade and Martin-Vaz Islands. Except for these islands, the ridge is entirely submerged and composed of flat-top seamounts and banks, most of them with summits between 55 and 75 m below the surface (Alberoni et al., 2019). The eddy activity on the VTR makes it an ideal place to study mesoscale flow-topography interaction.

Throughout the cruise, starting at the Davis Bank and ending at the Columbia Seamount (CS), we measured the velocity continually with a Vessel-Mounted Acoustic Doppler Current Profiler (VM-ADCP, *Teledyne RDI - 75* kHz) set to sample at 8m vertical bins. Data were processed using the CODAS (Common Ocean Data Access

System) software, following the guidelines of Firing (1995). To retain higher quality results, data below 60% of the returned signal (the so-called "percent good") were excluded. Hydrographic data were obtained using an Underway Temperature, Conductivity, and Depth (UCTD, *Teledyne Oceanscience*) probe at a high spatial resolution. Over the Davis Bank, the spatial resolution of temperature and salinity profiles was approximately 1 km. Over deep regions, the spatial resolution of profiles was around 5 km, but reaching deeper levels (approximately 450 m). We estimated the turbulent parameters from microscale shear variance measurements at five oceanographic stations (Figure 3.2). A Vertical Microstructure Profiler (VMP - 250 *Rockland Scientific*), operating at 512 Hz, was equipped with two shear probes, one SBE7 micro-conductivity probe and one FP07 thermistor. The VMP operated in downcast mode (free-falling profile), and for statistical reliability, we performed at least three casts at each station (e.g., Doubell et al., 2018; Lazaneo et al., 2020). The mesoscale surface field was estimated using the altimeter measurements distributed by the Copernicus Marine and Environment Monitoring Service (CMEMS, http://marine.copernicus.eu).

The SCV Vertical Structure

During the Ilhas 1 survey, we observed a mesoscale anticyclone over the CS through the objective mapping (correlation lengths: $\Delta x = 30\,\mathrm{km}$ and $\Delta z = 50\,\mathrm{m}$) of the horizontal velocity measured by the ADCP along the zonal section depicted in Figure (3.2).

The measured surface velocity agrees with the surface geostrophic velocity field from the altimeter (Figure 3.3). The subsurface maximum velocity occurred embedded in the anticyclonic meander, driving the anomalous values of the relative vorticity, obtained,

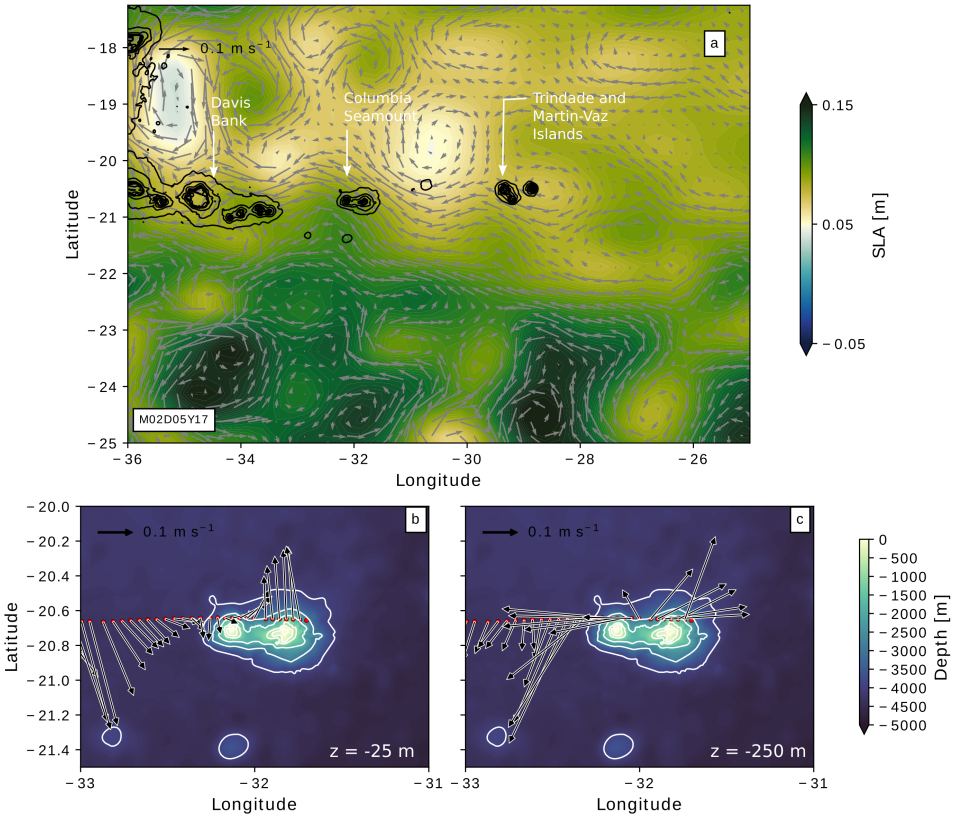

Figure 3.3: (a) Vitória-Trindade Ridge region map for February 5, 2017, with the background color representing sea level anomaly, and gray arrows indicating the geostrophic velocity. Bottom panels are the Columbia Seamount region map, with the light yellow shading representing depths shallower 300 m, and with the (b) surface and (c) subsurface velocities obtained by the ADCP. The black (a) and white (b and c) lines represent the 4000, 3000, 2000, 1000, 500, 250, 100, and 50 m isobaths.

in this case, from the zonal gradient of the meridional velocity ($\zeta = \partial v/\partial x$). The $\mathcal{O}(1)$ gradient Rossby number ($Ro = \zeta/f$, where f is the planetary vorticity) indicates the deviations from the dominant geostrophic balance (Figure 3.4).

It is indicative of a subsurface submesoscale phenomenon, bounded by double convex-lens-shaped isopycnals. This flow configuration indicates the existence of two interacting anticyclonic SCVs. In order to illustrate the eddy interaction, we present in Figure (3.5) a schematic of two adjacent anticyclones (see supporting information 6), as well as the associated vertical component of the relative vorticity and horizontal divergence. We notice alternating bands of anomalous values of both quantities (Figures 3.5b and 3.5c), such as those depicted in the fields of the observed SCVs (Figure 3.4).

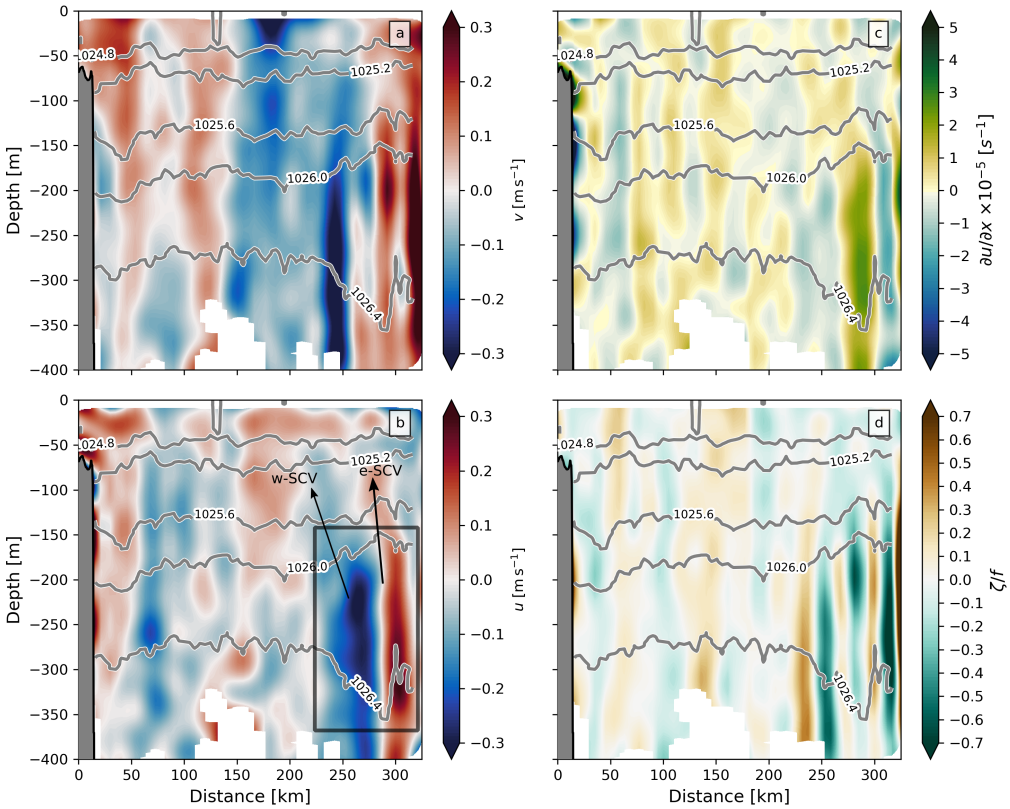

Figure 3.4: Vertical section of the (a) meridional velocity component, (b) zonal velocity component, (c) divergence considered as $\partial u/\partial x$, and (d) ζ/f. Gray contours represent the isopycnals [kg m^{-3}] along the section. The origin of the transect starts at the Davis Bank ($\sim$ 20.6° S, 34.7° W). The black rectangle encloses the location of the SCVs.

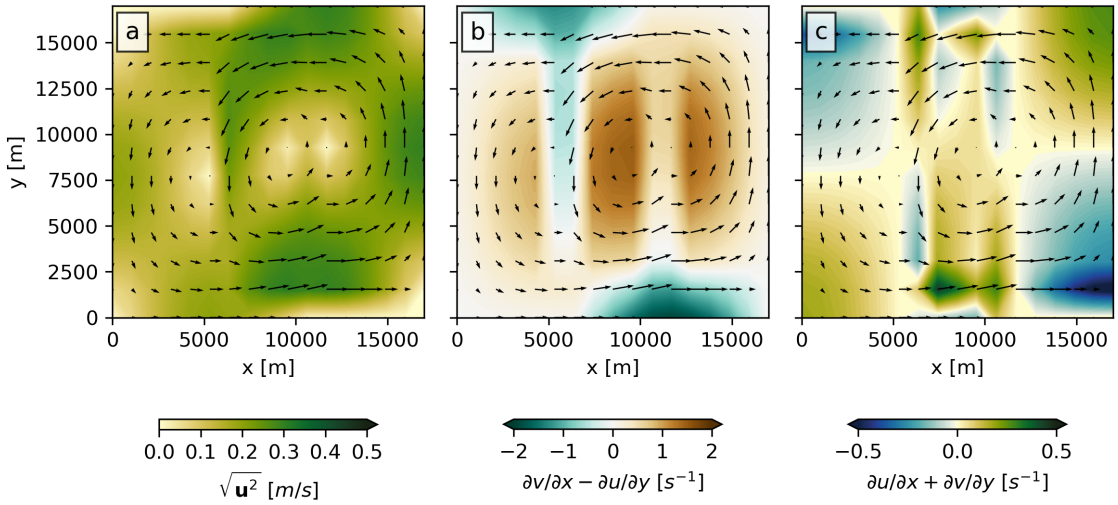

Figure 3.5: (a) Two-dimensional depiction of two adjacent anticyclones, as well as (b) the associated vertical component of the relative vorticity and (c) horizontal divergence. Black arrows are the velocity vectors from the velocity field.

Indeed, our observations show these alternating bands of $(\partial v/\partial x)$ and $(\partial u/\partial x)$ bounded by the isopycnal inflections that delimit the vortical features. We therefore interpret this

interaction of two vortices with the same rotation sense as a submesoscale version of the Fujiwhara effect in the ocean.

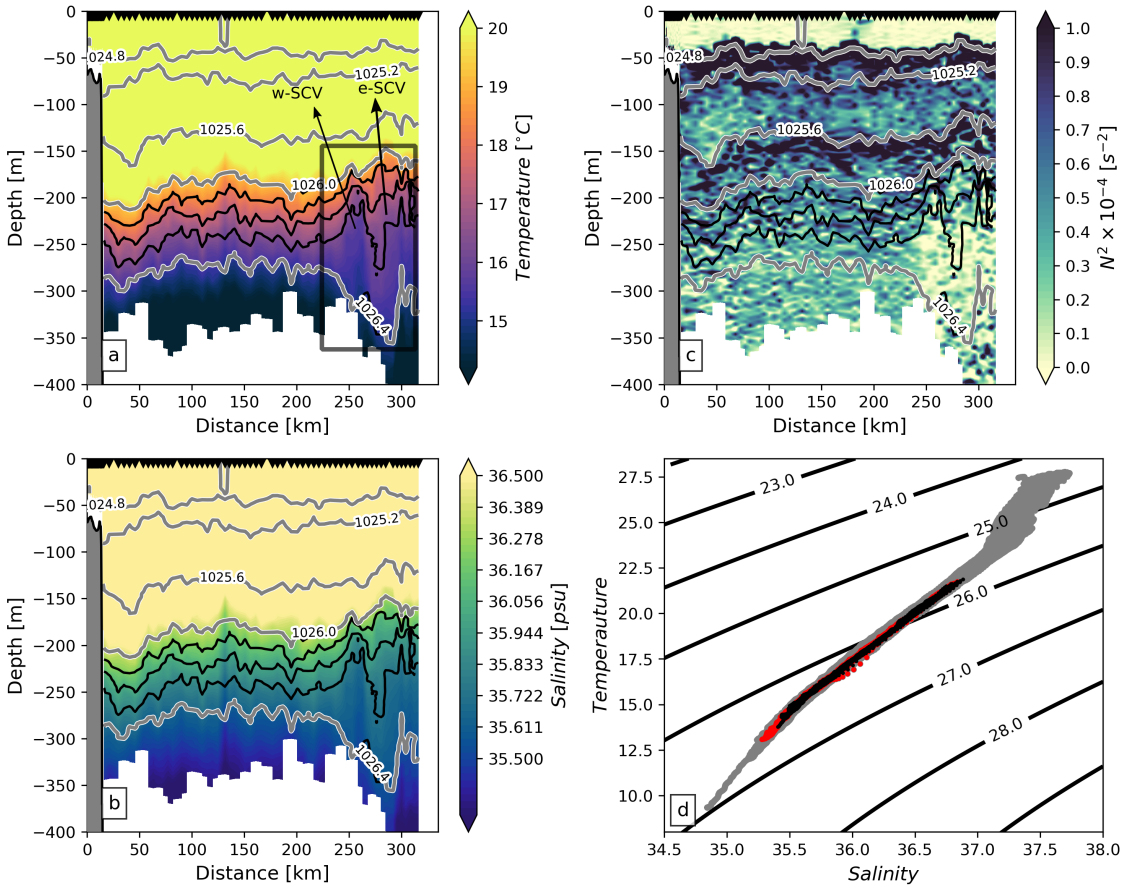

Figure 3.6: Vertical section of (a) temperature, (b) salinity, and (c) stratification. Gray and black contours represent the isopycnals [kg m^{-3}] along the section. (d) T-S diagram. Gray dots represent points along the whole section, while red and black dots represent T-S pairs within the e-SCV and w-SVC respectively. The origin of the transect starts at the Davis Bank ($\sim$ 20.6° S, 34.7° W). The black rectangle encloses the location of the SCVs.

In order to identify the intersection region between the SCVs and their limits with the surrounding waters, next we characterize the temperature and salinity signatures along the transect. Temperature (Figure 3.6a) and salinity (Figure 3.6b) present a heterogeneous horizontal distribution, with the most consistent variations associated with the location of subsurface velocity maximum. However, the deepening of isopycnals at $\sim$ 268 km from the origin of the transect – Davis Bank – demarcates the horizontal limit of the two adjacent SCVs. Despite the sharp inflections of the isopycnals in between the SCVs, weak stratification prevails within both convex lens-shaped isopycnals (Figure 3.6c). Further,

both SCVs present the same water mass content, which ultimately suggests that their generation sites may have been within the South Atlantic Central Water domain (see Stramma and England, 1999) (Figure 3.6d). The anomalous patterns in the temperature and salinity zonal distributions along some selected depths (-200 m, -250 m, -300 m) within the two SCVs not only elucidates their boundaries relative to the surrounding waters but also can be indicative of density compensation and mixing processes (Figures 3.7b – d). Aiming to verify the occurrence of density compensation at the SCV boundaries, we compute the spiciness variation ($\Delta\tau$)(Veronis, 1972; Munk, 1981; Ferrari and Rudnick, 2000)

$$\Delta\tau = (\alpha\Delta T) + (\gamma\Delta S), \tag{3.1}$$

where α is the thermal expansion coefficient, and γ is the saline contraction. Our results show that spicy waters (warm and salty) mark the contact region between the SCVs, while minty waters (fresh and colder) are found in both SCV cores (Figure 3.7a). These spiciness signatures are indicative of double-diffusion processes and mixing. The temperature and salinity profiles at the center of each SCV highlight the density compensation processes and mixing (Figure 3.7e – g). The SCV core to the west (w-SCV) has colder and fresher waters compared to the vortex waters to the east (e-SCV). Noting the temperature and salinity of the profile outside the vortices between -200 and -350 m, we observe that these profile segments have thermohaline properties different from the SCV core waters (Figure 3.7e – g). These signatures suggest that the SCVs were generated remotely but not necessarily distant from the observation site (e.g., Gula et al., 2019; McWilliams, 1985).

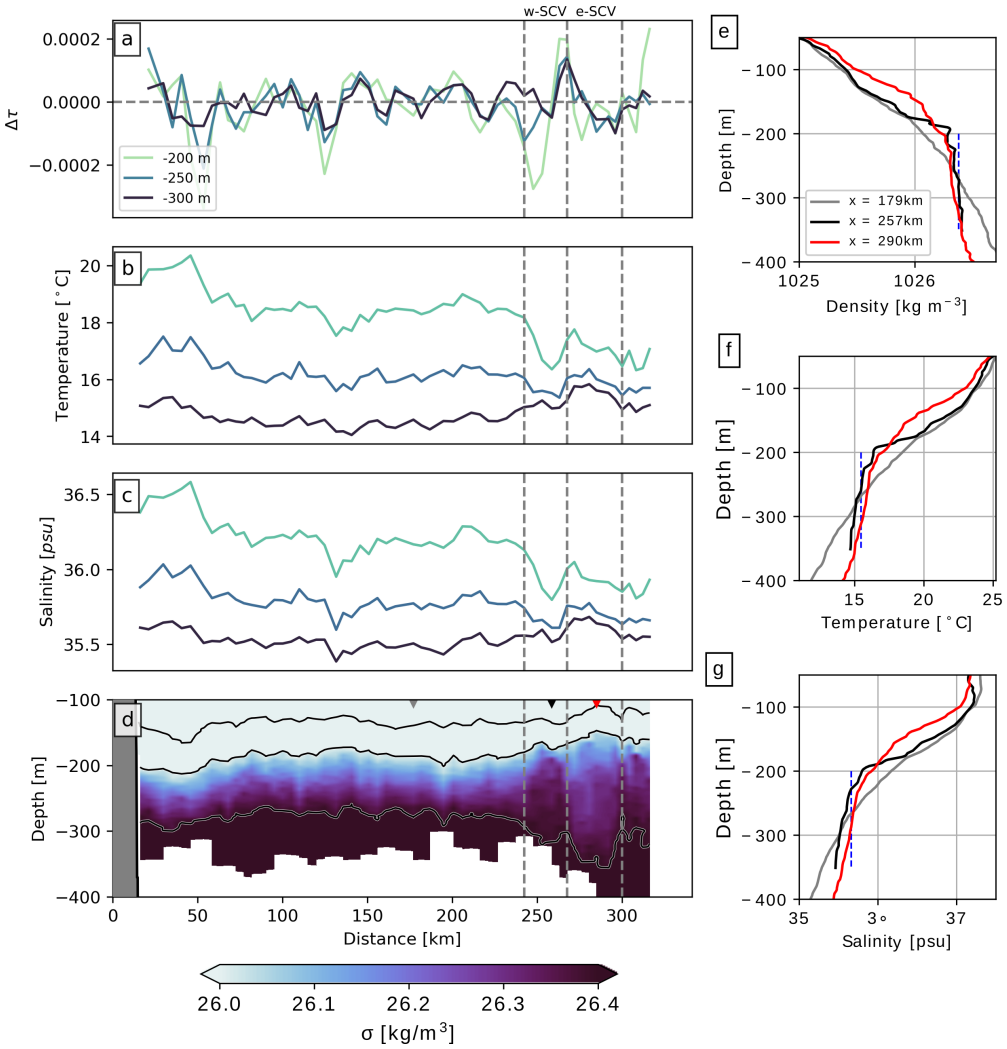

Figure 3.7: (a) The spiciness, (b) temperature, and (c) salinity variation along-track transect, at z levels. Cyan contours represent z = -200 m depth, blue contour represent z = -250 m depth, and dark blue represent z = -300 m depth. (d) Along-track transect of salinity anomaly S' along isopycnals. The horizontal dashed gray line in (a) represents the 0 of spiciness variation. The horizontal dashed gray lines in (d) represent the upper and lower isopycnal limiting the vertical extension of the e-SCV. The vertical grey dashed lines separate the w-SCV from the e-SCV. The origin of the transect starts at the Davis Bank ($\sim$ 20.6° S, 34.7° W). (e) Density, (f) temperature, and (g) salinity profiles in the center of the w-SCV (black) and e-SCV (red) and outside the SCVs (gray). The vertical blue dashed line represents the average value of properties of the profile outside de SCVs. The location of each profile is shown in panel (d) (top triangles).

Given the horizontal limits of the SCVs shown in Figure (3.7), the w-SCV has an l =12 km radius, and the e-SCV has an l =16 km radius. These values correspond respectively to about 20% and 28% of the full-depth first baroclinic deformation radius $R_D \sim 56$ km, which was estimated from the climatology following Houry et al. (1987). By combining the length and depth scales obtained by the thermohaline data analysis with

Table 3.1: Characterization of the SCVs in relation to the dimensionless numbers.

Number	Symbol	Expression	w-SCV Value	e-SCV Value
Rossby	Ro_b	$\overline{U}/fl$	0.46	0.27
Burger	Bu	$(Nh/fl)^2$	1.76	0.78

the velocity measurements, we estimate dimensionless numbers of the SCVs observed in the VTR during the Ilhas 1 survey. We calculate the bulk Rossby number ($Ro_b = \overline{\mathrm{U}}/fl$, where $\overline{\mathrm{U}}$ is the mean value of the velocity magnitude) and the "submesoscale " Burger number ($Bu = (Nh/fl)^2$, where h=150 m is the SCV thickness) for each SCV and present the results in Table (3.1). We then compare the results obtained for the VTR SCVs to those presented in the classical work by McWilliams (1985) for SCVs observed and advected by the Gulf Stream: $Ro_b \sim 0.25$ and Bu=0.3. While the Ro_b values found here are close to the former author's estimates, the Bu are larger. This is probably due to the fact that we are analyzing intrapycnoclinic SCVs (larger N) while McWilliams (1985) examined subpycnoclinic SCVs (smaller N). Nevertheless, the Bu values reflect a more important role for the relative vorticity (in contrast to the stretching vorticity) in our SCVs since they inhabited a region of stronger stratification.

We now seek to describe the potential vorticity (PV) structure of the SCVs captured near the CS. We know that the PV of an anticyclonic SCV core is low due to the strong vertical vorticity and weak stratification (Meunier et al., 2018). Low PV values are prone to instabilities (D'Asaro et al., 2011; Thomas et al., 2008, 2013). Here, we evaluate the two-dimensional PV (e.g., Lazaneo et al., 2020; Napolitano et al., 2020; Ramachandran et al., 2018; Thomas et al., 2016) from the objectively mapped field. It is

not possible to calculate the full Ertel PV since we have only a transect of data (Figure 3.8a). The consideration of the two-dimensional PV here is equivalent to assume that alongstream variations of quantities are negligible, which may be questionable. However, Napolitano et al. (2020) showed that the approximation is reasonable for submesoscale phenomena along the VTR.

The full Ertel PV is given by

$$q = (f\hat{k} + \nabla \times \mathbf{u}).\nabla b, \tag{3.2}$$

where $\hat{k}$ is the unit vector, $\mathbf{u} = (u, v, w)$ is the three-dimensional velocity vector, and $b = -g\rho/\rho_0$ is the buoyancy. The two-dimensional version of (3.2) for our section is

$$q \approx \left(f + \frac{\partial v}{\partial x} - \frac{u}{r}\right) N^2 - \frac{\partial v}{\partial z}\frac{\partial b}{\partial x}, \tag{3.3}$$

where $N^2 = \partial b/\partial z$ is the stratification and r is the radii of the SCV. The two-dimensional PV takes into account the curvature of the SCV. We use the radius of curvature of the captured w-SCV, r = 12 km, to estimate the greatest curvature effect in the potential vorticity.

To remove the ambiguity in the definition of PV in either the northern or southern hemisphere, we use the scaled PV instead

$$q \approx \left[\left(f + \frac{\partial v}{\partial x} - \frac{u}{r}\right) N^2 - \frac{\partial v}{\partial z}\frac{\partial b}{\partial x}\right] \frac{f}{\overline{f^2 N^2}}, \tag{3.4}$$

where the overbar denotes spatial averaging. Hence, q becomes a nondimensional quantity, and positive values mean a stable dynamic regime.

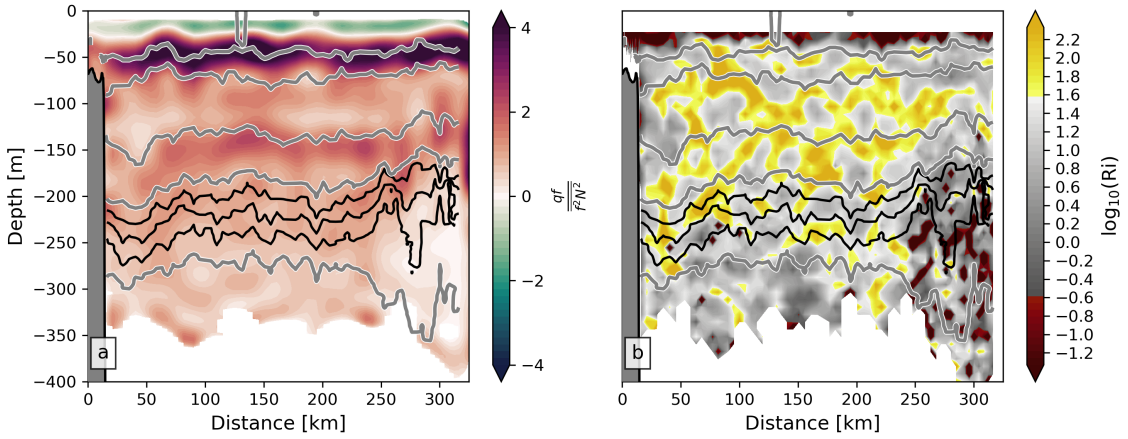

Figure 3.8: (a) Vertical section of the potential vorticity scaled by $f/(\overline{f^2N^2})^{-1}$. (b) Vertical section of 8 m Richardson number, in logarithmic scale. Values less than the Miles (1961) criterion are depicted in reds. The origin of the transect starts at the Davis Bank ($\sim$ 20.6° S, 34.7° W).

The PV reduction within the observed SCVs (Figure 3.8a) is driven by the vertical vorticity/stratification, as this term is more than an order of magnitude greater than the baroclinicity (not shown). While the baroclinicity term is small, the stratification within the SCVs is also low (Figure 3.6c). The comparison of these two terms provides a direct competition between the local stratification and the vertical shear. The generation of turbulence and mixing occurs when the destabilizing influence of shear overcomes the stabilizing influence of stratification, which is revealed by the Richardson number. The 8m-resolution Richardson number (*Ri* hereafter) is sometimes smaller than the Miles instability criterion (Miles, 1961), and also close to 1 within the SCVs (Figure 3.8b). It is indicative of the formation of small-scale turbulence in the SCVs' interiors, which may provide a significant amount of energy dissipation.

Pathway for Energy Dissipation

One of the defining characteristics of anticyclonic SCVs is that they exhibit anomalously low potential vorticity, as do those observed during the Ilhas 1 survey (e.g.,

Gula et al., 2019). The origin of this marginally stable regime in their cores comes from their site of origin. PV reduction can occur from convective and frontal processes at the surface (Thomas, 2005; Thomas et al., 2013) and subsurface frictional forces due to flow separation near topography (D'Asaro, 1988; Gula et al., 2019). In both cases, the manifestation of instabilities in this dynamical regime involves smaller-scale turbulence that cascades energy down to dissipation (McWilliams, 2016). Our in-situ, microstructure measurements reveal that turbulent kinetic energy (TKE, ε) dissipation within the SCVs is two orders of magnitude larger than in surrounding waters (Figures 3.9a – f), thus showing that SCVs are important agents for energy dissipation.

From the integration of the spectrum of velocity fluctuations (Φ), we estimated the TKE dissipation rates for segments of the water column,

$$\varepsilon = \frac{15}{2}\nu\overline{\left(\frac{\partial u'}{\partial z}\right)^2} = \frac{15}{2}\nu\int_1^{k_{max}} \Phi(k)dk \ [\mathrm{W\ kg^{-1}}], \tag{3.5}$$

where ν is the kinematic molecular viscosity, and k_{max} is the maximum wavenumber determined by the fast Fourier transform with a 50% overlap for each vertical segment. For this study, we chose segments of the water column corresponding to 1 s to convert temporal derivatives to spatial derivatives, assuming a frozen field hypothesis (Taylor, 1938). Lazaneo et al. (2020) showed that there is no significant ε variation from the different lengths of segments. Since the VTR presents very abrupt changes of depth, using a bin size of 1 s to estimate ε provides a reasonable number of values, mainly over shallow regions. The shorter the segment length, the greater the noise of the estimation. However, using an average from multiple microstructure profilers deployed at the same station, we can reduce the noise while keeping the strongest signal (e.g., Doubell et al., 2018; Lazaneo et al., 2020). Comparing the measured spectrum with the theoretical Nasmyth spectrum (Figure 3.9g), we achieve better reliability.

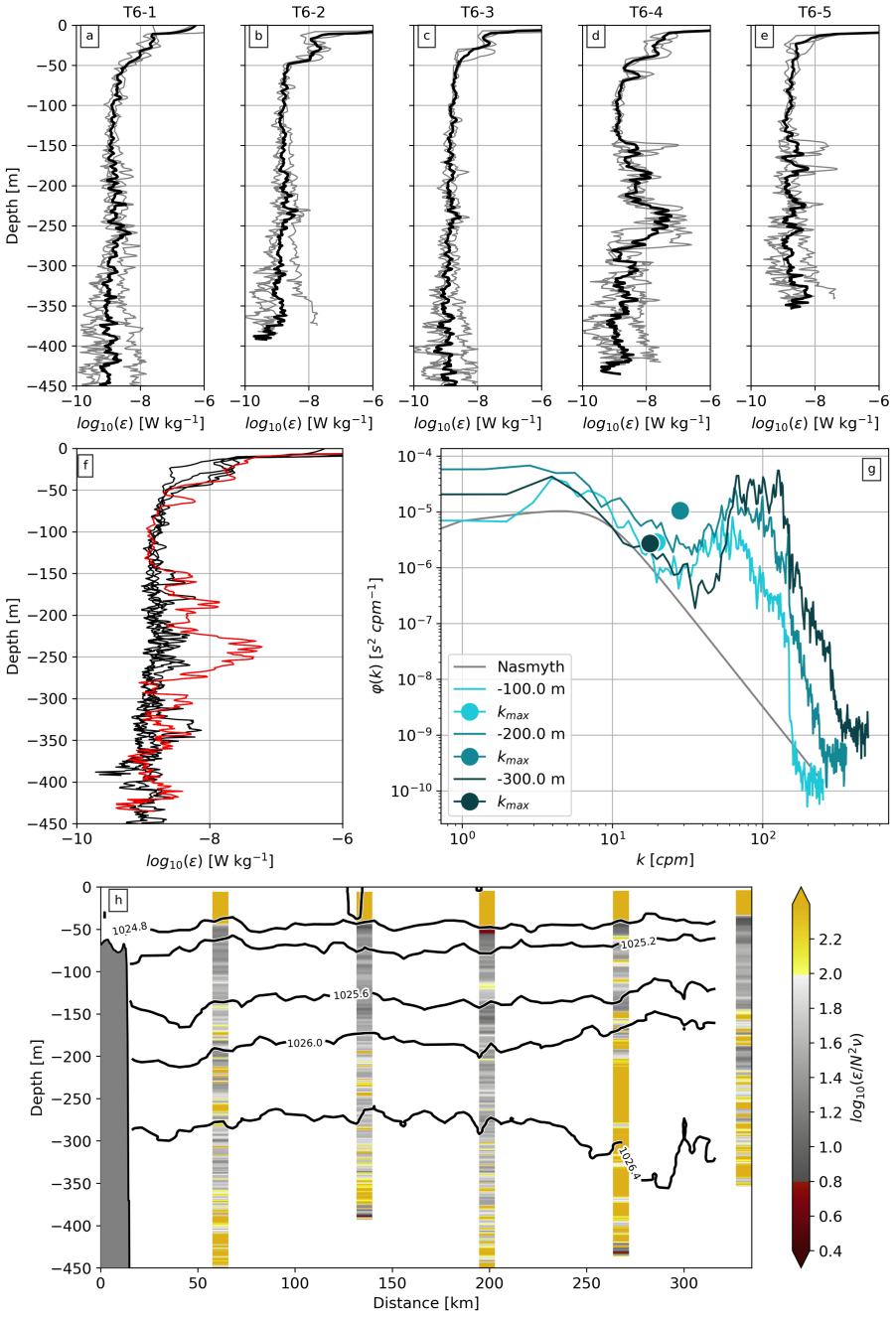

Figure 3.9: (a) to (e) Vertical profiles of TKE dissipation rates. Gray lines represent n-cast deployed at each oceanographic station, while black lines show the average profile at each station.(f) Shows the average profiles presented in top panels together, highlighting the amount of energy dissipation rates within the SCV at station T6-4 (red). (g) Shear spectrum observed by a VMP at different depths at station T6-4 superimposed on the Nasmyth spectrum (gray curve), where k_{max} is the integration cutoff wave number. (h) Spatial distribution of the buoyancy Reynolds number ($Re_b = \varepsilon/\nu N^2$) superimposed on the isopycnal surfaces (black contours).

The composite mean of the TKE dissipation rate shows a nearly constant amount of energy dissipation along the water column (Figure 3.9). However, the last two stations nearby the CS show a significant increase in the amount of energy dissipation at the sub-

thermocline level. From -150 m depth to -300 m depth at station T6-4, a great burst of energy dissipation reaches values typical of the mixed layer. The turbulence activity parameter ($\varepsilon/\nu N^2$), also called buoyancy Reynolds number (Re_b), provides an additional indication of the degree of turbulence in the SCV core. This parameter scales with turbulent diffusivity from the Osborn model (Osborn, 1980) for the intermediate regime. On the other hand, the diffusivity scales with $(Re_b)^{1/2}$ for the energetic regime, corresponding to higher values of Re_b and growing turbulence (Shih et al., 2005). For the e-SCV, Re_b is extremely high, in fact comparable to the turbulent regime of the mixed layer (Figure 3.9h).

The distance between consecutive microstructure profilers along the transect does not permit the estimation of the TKE dissipation of both SCVs. However, the combination of weak stratification, high vorticity, low PV, and low *Ri* corroborates the hypothesis of intense mixing and energy dissipation within such features. Finally, the evidence of the anomalous amount of energy dissipation in the e-SCV core evinces the role of SCVs in the ocean energy budget. Nevertheless, it remains an open question where these vortices have been generated, and another unsettled issue is whether or not the VTR is prone to form such small features. To address these questions, we inspect the mesoscale circulation pattern using altimetry data and compare this scenario with the previous findings from the Ihas 1 survey.

Mesoscale circulation pattern along the VTR

In this section, we address the possibility that the SCVs captured by the Ilhas 1 survey sampling had been formed through interaction of an ocean current with the VTR. Mesoscale eddies contain the majority of the kinetic energy of ocean currents. The term

"eddies" is used here to represent the various forms of ocean current variability at the mesoscale: vortices, rings, and current meanders (e.g., Fu, 2006). The VTR is located in the northwestern limb of the South Atlantic subtropical gyre circulation (Stramma and England, 1999). The region is potentially along the path of the southern branch of the South Equatorial Current (SEC) (Garzoli and Matano, 2011; Nencioli et al., 2018). Surface data obtained through altimeters provide a two-dimensional synoptic view of mesoscale eddies (Chelton et al., 2011). From the altimetry data, it is possible to map the pathways of the mesoscale eddies reaching the VTR along with the SEC.

The surface circulation pattern through the period of the austral summer via altimetry data shows a mesoscale anticyclonic signal over the CS (Figure 3.3). From the daily output of the absolute dynamic topography, we tracked this signal backward in time to investigate its pathway prior to reaching the sampled area (Figure 3.10). In early November 2016, the anticyclonic meander was observed southeast of Trindade Island, centered at 22° S 27.5° W (Figures 3.10a and 3.10e). We defined the eddy as a region with values of Okubo-Weiss parameter $W < -0.2\sigma_W$, where σ_W is the spatial standard deviation of W. This definition is shown to be appropriate to detect mesoscale eddies from sea level anomaly (e.g., Isern-Fontanet et al., 2006; Zhang et al., 2016). In December, the northern edge of the anticyclone obliquely hits the island, deforming itself and enhancing its absolute dynamic topography (Figures 3.10b and 3.10f). After the interaction with the island, the geostrophic vorticity of the anticyclone decayed, keeping its core south of the island. In mid-January, this anticyclonic signal appears as a westward-propagating meander reaching the CS (Figures 3.10d and 3.10h). While the surface mesoscale circulation pattern depicted from the altimeters shows the anticyclone passing across the CS, the

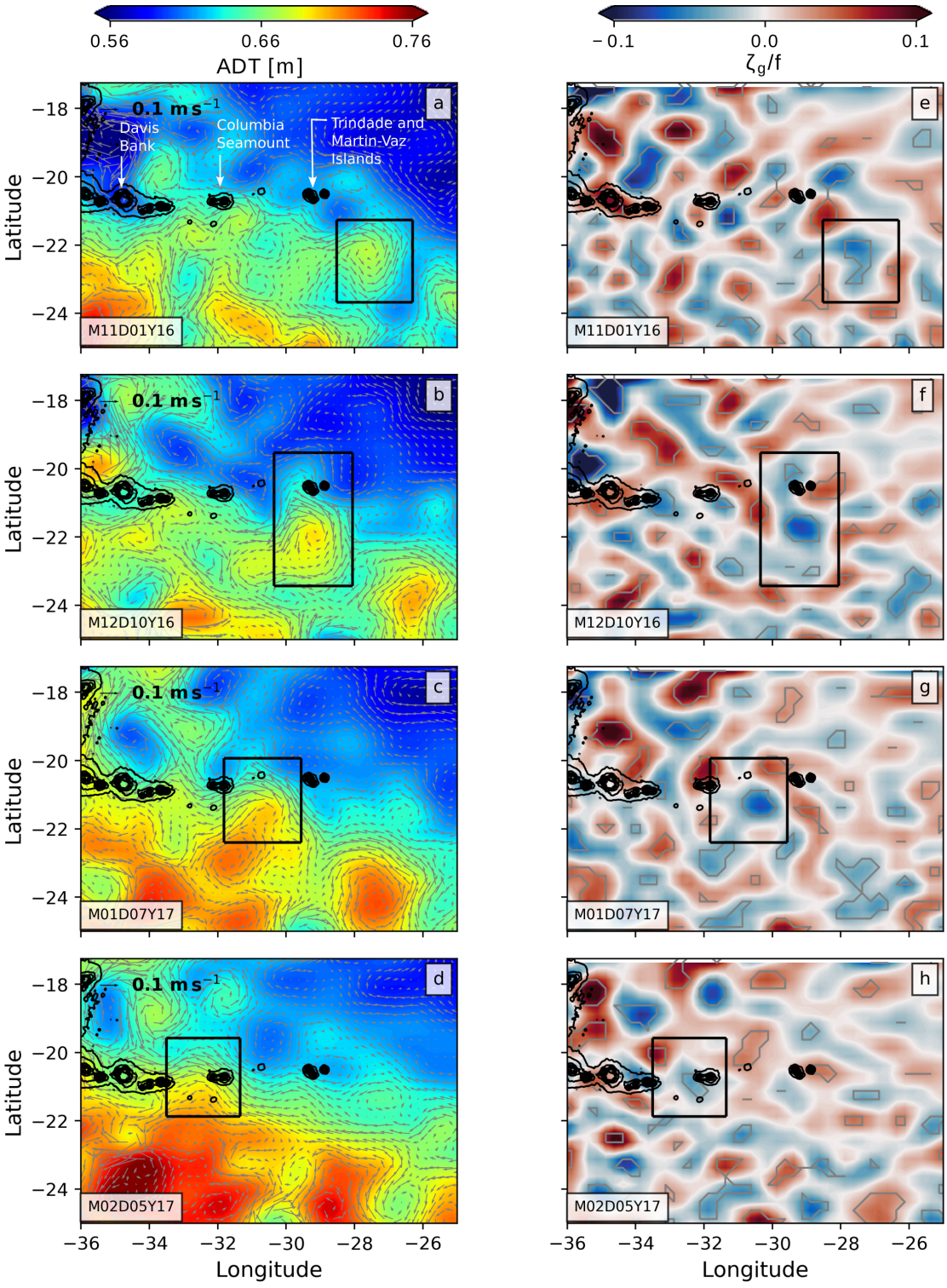

Figure 3.10: (a – d) Daily snapshots of the absolute dynamic topography (background color) with its respective velocity field (gray arrows). (e – h) Daily snapshots of ζ_g/f (background color), where $\zeta_g = \partial v_g/\partial x - \partial u_g/\partial y$. u_g and v_g are the geostrophic velocity components derived from CMEMS. Gray contours represent the Okubo-Weiss parameter for eddy detection. Black contours represent the isobaths around the VTR. The area used to calculate the standard deviation is the area shown on the maps.

ADCP measurements show this eddy signal at the surface, with the maximum subsurface velocity related to the SCVs embedded in its flow (Figure 3.3).

According to Gula et al. (2016), as a (mesoscale) jet passes across a topographic obstacle, submesoscale relative vorticity grows downstream. The combination of intense relative vorticity and low stratification may lead to centrifugal instabilities at the island wakes (e.g., Srinivasan et al., 2019). The bottom boundary condition imposed by the physical barrier of topography triggers the intense horizontal shear in a low-stratified environment below the pycnocline. Under certain conditions, these unstable wakes evolve to form SCVs (Srinivasan et al., 2019) without a surface signature (Gula et al., 2019). The tendency toward instabilities in the anticyclonic SCV cores (low PV values) may come from their generation sites. The impermeability theorem states that PV is conserved across two isopycnal surfaces (Haynes and McIntyre, 1987). Thus, the PV reduction should occur through diabatic processes or frictional forces within the two bounded isopycnals (Thomas, 2005), leading to negative PV anomalies within the SCV cores (see Gula et al., 2019). Despite the low, but positive values of PV, mainly driven by the high horizontal shear, the weak stratification can be sporadically overcome by the vertical shear, leading to small-scale turbulence and mixing.

Long-lived SCVs may also reach the VTR region from remote locations (e.g., McCoy et al., 2020). Analysis of Argo float data has revealed that SCVs are ubiquitous in the ocean, and thus of great importance in the large-scale transport of tracers (McCoy et al., 2020). The authors argued that tracked SCVs are, in part, generated in eastern boundary upwelling systems, in marginal sea overflows – influenced by capes and promontories – along open ocean fronts, and ultimately travel across the ocean basins. Here, we show the trajectory of two Argo floats that captured SCV-like structures in their

pathways (Figure 3.11). The first Argo float trajectory shows the presence of one SCV away from the VTR (Figures 3.11a and 3.11c). The westward flow of the South Equatorial Current (SEC) can advect the SCV-like structure along the South Atlantic basin since the β effect has a relatively minor influence on its trajectory (Dewar and Meng, 1995). On the other hand, the trajectory of a second Argo float shows the occurrence of one SCV to the south of the VTR (Figures 3.11b and 3.11d). We cannot determine whether or not the latter SCV, captured by the Argo float, was generated at the VTR. Therefore, SCV-like structures can not only reach the VTR region by the SEC advection, but can also be locally generated.

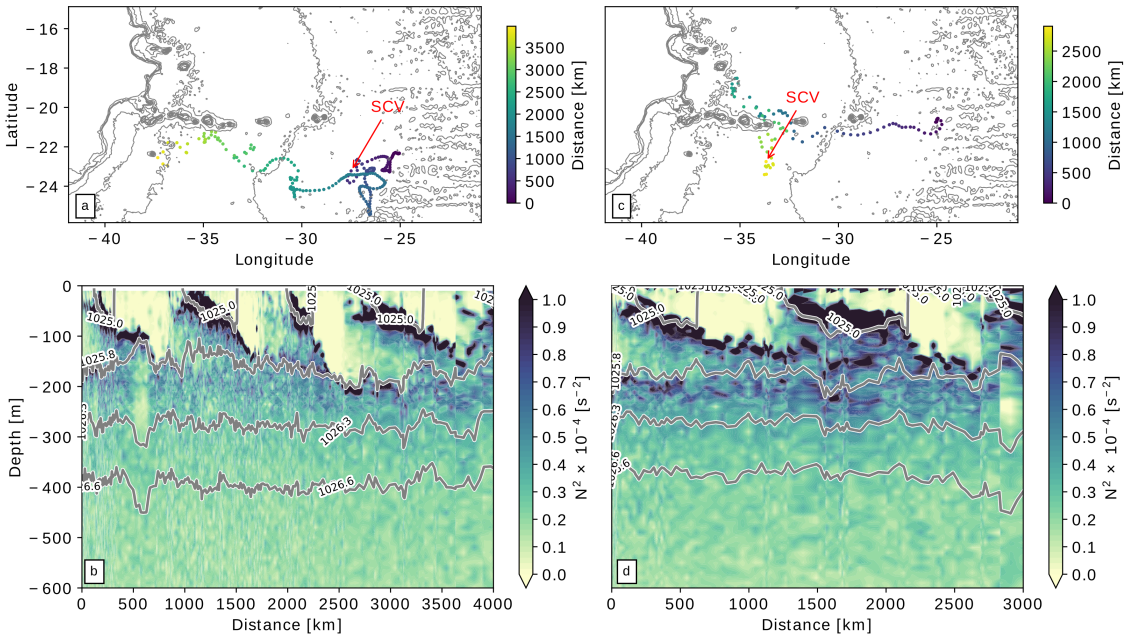

Figure 3.11: Trajectories of the ARGO floats (a) 3901496, and (c) 3902125 based on the distance from their origin. Vertical section of the stratification from ARGO floats (b) 3901496, and (d) 3902125. The red arrows represent the location of the SCV in each ARGO float trajectory. (Data source: http://www.coriolis.eu.org/).

Observations of these small structures in the ocean, such as the SCV captured during the Ilhas 1 survey, are challenging due to the vortices' small size and the portion of the water column they occupy (below the mixed layer). Nevertheless, we see them as keys to understanding the ocean interior variability since they transport water mass

from their site of origin (life cycle on the order of years) (McWilliams, 1985, 2016) and lead to energy dissipation enhancement through centrifugal instabilities (Srinivasan et al., 2019). Most of these findings gathered from the literature evinced the importance of submesoscale features to the ocean energy budget. However, these studies employed numerical simulations and computed the energy budget from the outputs. The present study is observational, and neither the energy budget nor the SCV site of origin estimate can be determined from our data. Despite that, we see as likely that the captured SCVs near the CS are a result of the interaction of the meandering SEC with the VTR.

Summary and Concluding Remarks

In this study, we describe unprecedented observations of two adjacent SCVs embedded in the SEC as it flowed across the VTR. These intrapycnoclinic features occupied the density range of 1026 and 1026.4 kg/m^3, and presented a vertical extension of approximately 150 m. The radii of the two submesoscale vortices were 12 km and 16 km. They presented Ro_b as 0.46 and 0.27, and Bu as 1.76 and 0.78. The SCVs were characterized by homogenized SACW waters bounded by two convex-lens-shaped isopycnals and intense relative vorticity. The combination of temperature, salinity, and velocity measurements allowed us to determine the marginally stable dynamic regime inside the SCVs, which ultimately suggests small-scale turbulence cascading energy down to dissipation. Our *in situ* observations revealed that the e-SCV contained dissipation rates at least two orders of magnitude higher than the surrounding waters, comparable to turbulence of the mixed layer. This anomalous energy dissipation rate confirms the occurrence of turbulence inside the e-SCV.

The limited spatial distribution of sampling data does not permit the determination of the place of formation of the captured SCVs. Temperature and salinity signatures within each SCV exhibit homogenized SACW in their cores, with tiny deviations relative to the surrounding waters. These results suggest a remote site for the SCVs' generation, but not necessarily out of the VTR region, since flow-topography interaction is one of the principal candidates for SCV generation. We provide evidence of the flow-topography interaction by tracking an SEC meander passing by the Trindade Island two months earlier than the period of the Ilhas 1 survey (austral summer). This mesoscale anticyclonic meander was observed over the CS through altimetry and ADCP measurements during our oceanographic survey. The pathway of such a mesoscale anticyclone indicate its crossing of the Trindade Island two months earlier. The archipelago of Trindade and Martin-Vaz is the easternmost isolated set of islands along the SEC pathway in the western South Atlantic basin. Such interaction could result in SCV generation through centrifugal instability in the island wakes (D'Asaro, 1988). Submesoscale-resolving simulations are already under development to verify if the interaction of the eddy-rich SEC with the VTR is indeed prone to generate SCVs. However, the lack of observations in the region is still the main constraint on a better comprehension of SCV dynamics and their roles in the local dynamics.

Moreover, since SCVs have been observed throughout the world's oceans, they may make a significant contribution to the energy budget of the oceans. The research presented here, therefore, encourages further research into better understanding the role of SCVs in (global) ocean circulation, including their impacts on tracer and energy fluxes.

Supporting Information

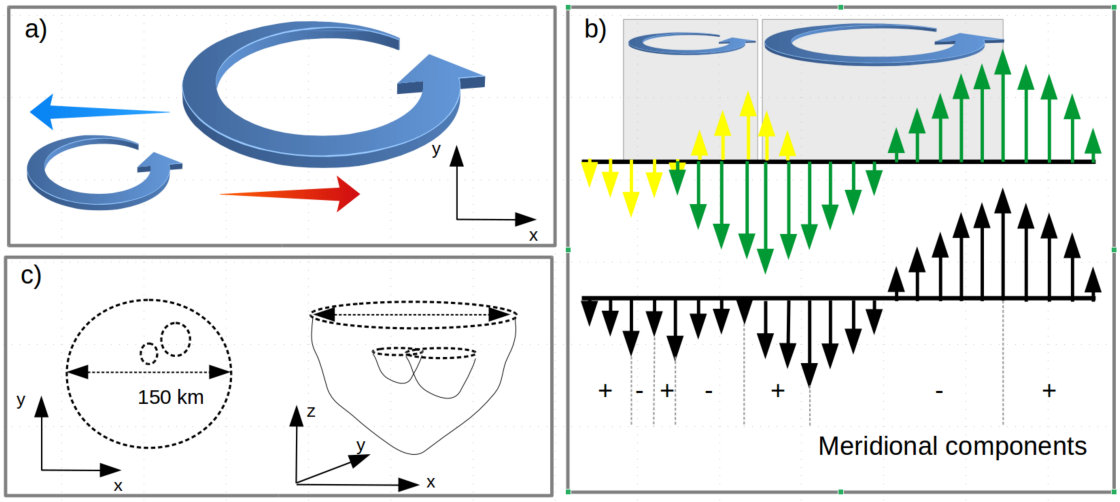

Figure 3.12: Panel (a) is a depiction of two adjacent anticyclones with different radii in the horizontal plane. The blue and red arrows indicate the divergence within the intersection region of them. Panel (b) illustrates the meridional velocity vectors from the adjacent vortices (yellow arrows represent the vortex on the left, and the green arrows represent the vortex on the right side). Black arrows represent the sum of the green and yellow arrows. The positive and negative signs highlight the alternation bands of $\partial v/\partial x$. Panel (c) depicts the two adjacent vortices embedded in a larger eddy.

Acknowledgments

We thank Frank O. Smith for copy editing and proofreading this manuscript. We also thank Dante C. Napolitano for the help in the ADCP data processing. This study is part of the “Projeto Ilhas ”(Processo CNPq 458583/2013-8). C. Z. Lazaneo acknowledges support from Coordenação de Aperfeiçoamento de Pessoal de Nível Superior - Brasil (CAPES) - Finance Code 001, and from Conselho Nacional de Desenvolvimento Científico e Tecnológico - CNPq (Processo 205857/2018-3). P. H. R. Calil acknowledges support from Projeto ILHAS (Processo CNPq 458583/2013-8). A. Tandon acknowledges support from NSF Grant OCE1755313 and ONR N000141812799

I. C. A. da Silveira acknowledges support from CNPq (Grant 307814/2017-3), Projeto SUBMESO (Processo CNPq 442926/2015-4), Projeto REMARSUL (Processo CAPES 88882.158621/2014-01), and Projeto VT-Dyn (Processo FAPESP 2015/21729-4). The authors are very grateful to the crew of R/V Alpha Crucis and, in particular, Captain José H. M. Rezende.

CHAPTER 4.

SUBMESOSCALE COHERENT VORTEX GENERATION AT THE VITÓRIA-TRINDADE RIDGE

Manuscript in preparation for submission to the *Journal of Geophysical Research–Oceans*. This manuscript is co-authored by Amit Tandon, Ilson C. A. Silveira and Paulo H. R. Calil

Abstract

Meanders and eddies of the South Equatorial Current (SEC) are routinely observed passing through the Vitória-Trindade Ridge (VTR). Here, we analyze the influence of islands and seamounts of the ridge in the formation of submesoscale coherent vortices (SCV) through eddy-topography interaction using a high-resolution regional ocean model simulation. The meandering pattern of the SEC interacts with the VTR topography resulting in SCV generation with both polarities (cyclonic/anticyclonic). The bottom drag amplifies the vortical wake and changes the potential vorticity of the flow. Eventually, the vortical filaments roll up by forming an SCV, whose polarity is defined by the side of the inshore edge of the SEC meander that interacts with topography. We diagnose that, regardless of the topographic feature or depth (below the mixed layer), SCVs are often generated in the VTR owing to the flow-topography interaction. For that reason, we conclude that the region can be considered a hot spot of SCV formation. Once they are detached from the topography, they are advected by the SEC towards the South American continent carrying waters from their origin site.

Introduction

Submesoscale coherent vortices (SCVs) are subsurface eddies with radii smaller than the first baroclinic radius (R_D) and can wander in the interior ocean for months to

years (McCoy et al., 2020; McWilliams, 1985, 2016). They are defined as submesoscale flow not only because of their size ($< R_D$) but also because of relatively large Rossby numbers associated with them, which suggests that they are not necessarily geostrophic.

Larger scale flows determine their trajectory since the β effect over their small size has a limited impact (Dewar and Meng, 1995). SCVs are predominantly generated by flow separation downstream of topographic features (D'Asaro, 1988; Gula et al., 2019; Srinivasan et al., 2019; Vic et al., 2018). This generates a vertical vorticity influx into the flow that ultimately creates potential vorticity anomalies (e.g., de Marez et al., 2020; Gula et al., 2019). Thus, the rotation sense of SCVs is prescribed by the inshore edge of the flow that interacts with the topography (see D'Asaro, 1988; de Marez et al., 2020; Gula et al., 2019). For anticyclonic SCVs, the resulting potential vorticity values are close to zero – negative anomalies – due to the anticyclonic vertical vorticity (D'Asaro, 1988; Gula et al., 2019, Lazaneo et al., "In revision"; hereinafter L21 [1]). For cyclonic SCV's, not as commonly observed as the anticyclonic ones (McWilliams, 2016), the anomalies of potential vorticity are positive due to cyclonic vertical vorticity (de Marez et al., 2020). The SCV structure acquired at the topographic wake prevents property exchanges with surrounding waters. Once developed, they carry water properties and dynamic characteristics from their generation site into the interior of the ocean's basins, where they are able to coherently propagate from months to years (McWilliams, 2016; McCoy et al., 2020).

Seamounts and islands are ubiquitous in the ocean and may be hotspots for SCVs generation with consequences for the dissipation of the kinetic energy in the ocean (L21, Srinivasan et al., 2019). These topographic features are poorly represented in global climate models because of their small size and the relatively low horizontal resolution of the

[1]This reference is related to Chapter 3 of this dissertation. The manuscript is in revision in the Journal of Geophysical Research: oceans. Hereinafter: L21

models. Therefore, their effect on the circulation is not resolved in such models. In this study, we show the role of the Vitória-Trindade Ridge (20.5° S, hereon VTR) in the formation of SCVs by using a high-resolution regional ocean model. Previous studies have shown that SCVs reach the VTR region following the South Equatorial Current (SEC) pathway (McCoy et al., 2020), but they also indicate the region as prone to SCV formation (L21) due to the interaction between the SEC and the seamounts. From high-resolution thermohaline and horizontal velocity measurements over the VTR in the South Atlantic Ocean, L21 captured two adjacent anticyclonic SCVs interacting within the ridge. The SCVs were embedded in a propagating mesoscale anticyclonic SEC meander. Using altimetry data, they showed that the meander passed through the Trindade Island (20.5° S, 29.5° W) two months before the measurements were taken.

The VTR seamount chain is located along the pathway of the southern branch of SEC, which connects the eastern to the western portion of the South Atlantic Ocean (Luko et al., 2021; Rodrigues et al., 2007; Soutelino et al., 2013; Stramma and England, 1999). The upper SEC circulation presents an intense level of eddy kinetic energy associated with the frequent propagation of mesoscale eddies in the open ocean (Chelton et al., 2011). The SEC pathway has been attributed as a corridor for mesoscale eddies that may dissipate part of their energy at the VTR region through the interaction with the shallow and isolated topographic features (Garzoli and Matano, 2011; Guerra et al., 2018; Nencioli et al., 2018).

Weaker currents and eddies similarly generate downstream vorticity even in the open ocean, where flows encounter isolated topographic features like islands and seamounts (Srinivasan et al., 2019, e.g.,). Even in these cases, the mechanism of SCVs generation has been shown to occur in the same manner as described by D'Asaro (1988).

For a scenario where a meandering jet passes through a shallow seamount or island, the angle of attack of the incoming non-stationary flow related to the isolated topography changes and determines the rotation sense of the vortical wake. Thus, it suggests that meandering flows passing through isolated topography features are be prone to generate both cyclonic and anticyclonic SCVs (Figure 4.1).

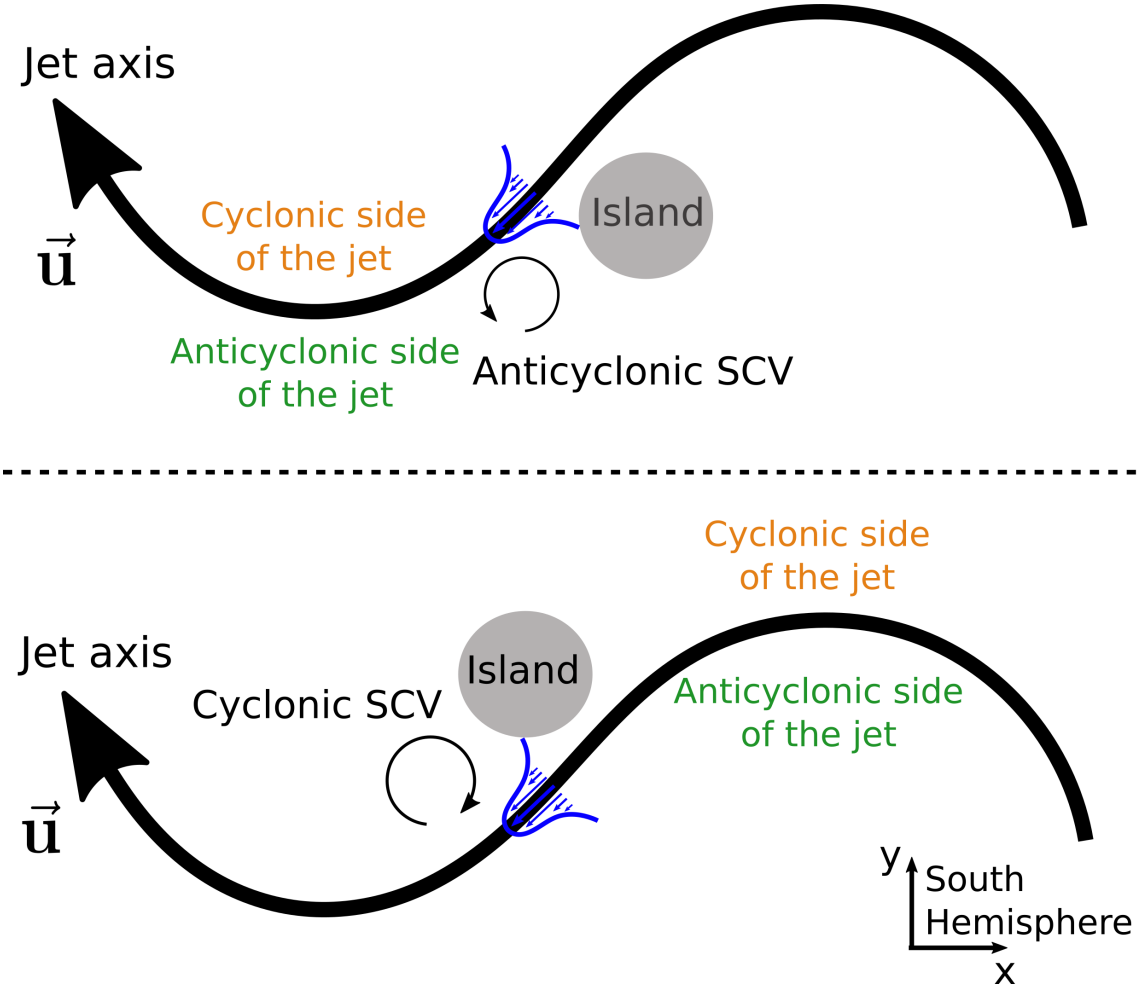

Figure 4.1: Illustration of the interaction between a meandering flow ($\vec{u}$) and an island in the South Hemisphere (f <0). The picture suggests a formation of anticyclonic or cyclonic SCVs depending on the inshore edge of the flow that hits the island. In this graphic, x and y correspond to along-front and cross-front displacements, consistent with the meandering SEC flow.

In this work, we test the hypothesis whether the VTR region is prone to SCV generation, like those observed by L21 nearby the region and discuss the dynamics of SCV generation near topographic features. Section 2 defines the numerical setup and presents the evaluation of the model results. Section 3 describes the generation of an SCV

from a SEC meander in the lee of the Trindade Island. Section 4 explores the Columbia Seamount along the VTR as a possible site prone to SCV generation. Section 5 presents the main findings and conclusions.

The submesoscale-resolving simulation

We use the Coastal and Regional Ocean Community Model (CROCO) (https://www.croco-ocean.org), an oceanic modeling system built upon the Regional Ocean Modeling System (ROMS) (Shchepetkin and McWilliams, 2005). A high-resolution simulation was conducted with about 1 km of horizontal resolution and 50 sigma levels in the vertical to simulate the circulation in the western South Atlantic, with the VTR in the center of the domain (Figure 4.2). Thus, there is no direct influence of the open boundaries in the local dynamics.

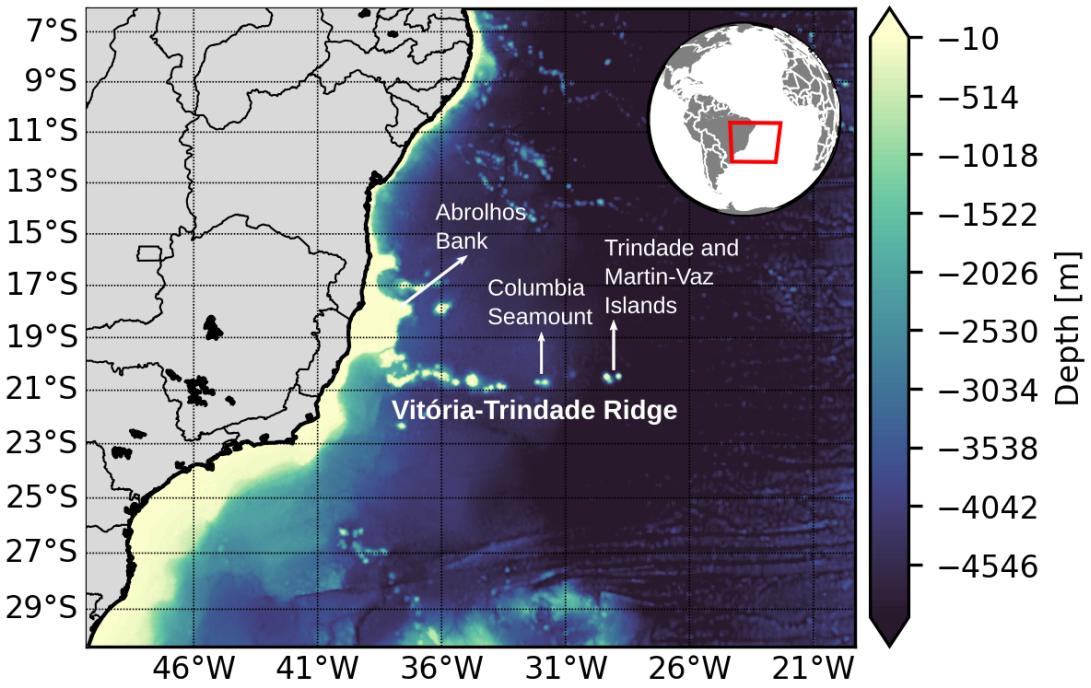

Figure 4.2: Topography (m) of the western South Atlantic Ocean from the ETOPO2 Smith and Sandwell (1995) data set. The VTR lies at the south end of the Abrolhos Bank. The The topography has been interpolated on the grid of the CROCO simulation ($\Delta x \sim 1$ km).

The model is forced with the daily QuickSCAT wind stress for the year 2000 and climatological air-sea fluxes from COADS (Comprehensive Ocean-Atmosphere Data Set). At the open boundaries, we use the Simple Ocean Data Assimilation (SODA) reanalysis (Carton et al., 2018) for the year 2000. SODA is also used as the initial condition for the whole domain. Barotropic tidal forcing is obtained from the OSU TOPEX/POSEIDON Global Inverse Solution TPXO (Egbert and Erofeeva, 2002). The horizontal and vertical advection schemes used for tracers and momentum are the 5^{th} order weighted essentially non-oscillatory scheme (WENO5). Vertical mixing processes in the model are parameterized with the k-profile parameterization (KPP), both in the surface and bottom boundary layers (Large et al., 1994). The model is run for four years, where the first three years are the spin-up. We analyze the fourth year of the simulation in the present work.

The numerical scheme and the input data sets used to set our experiment are the same as those used in recent numerical studies in the western South Atlantic Ocean (e.g., Calil et al., 2021; Napolitano et al., 2019, 2020). The main difference is the higher 1 km grid resolution in our work. While the numerical experiments of the aforementioned studies had been already validated, we also opt to validate our modeled fields with observations. We compare them with available data for the region that was either made available to us or were analyzed and reported in previous works.

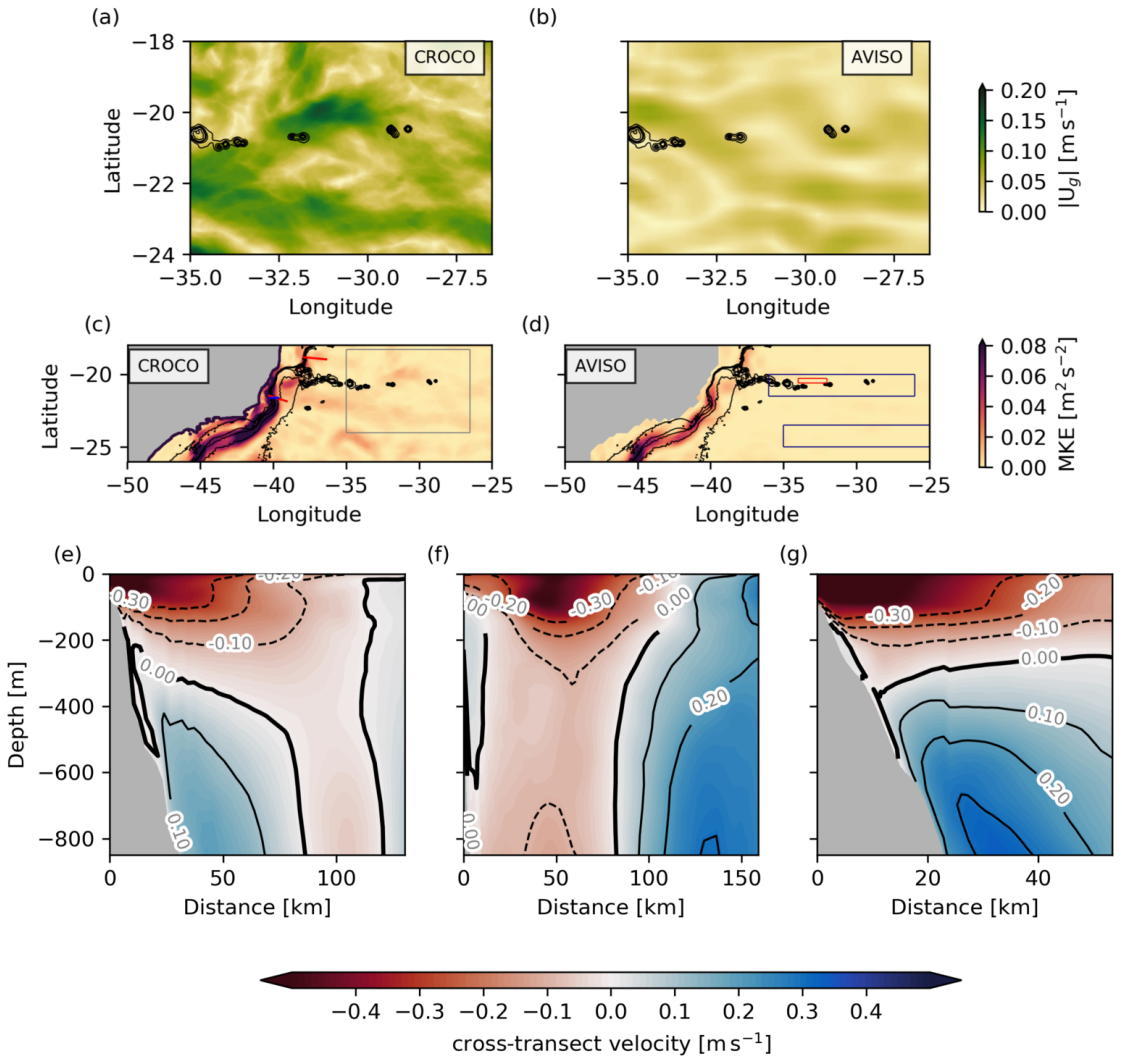

Figure 4.3: Annual mean velocity field (a) from the fourth year of simulation and (b) from the altimeter observation from the year 2000. Annual mean (same year as mentioned before) kinetic energy field (c) from the simulation and (d) altimeter along the VTR. The gray box represented in panel (c) corresponds to the area depicted in panels (a) and (b). Panels (e), (f), and (g) are vertical sections of the cross-transect velocity component at the VTR from the model. Panel (e) and (f) are related to observations presented by Napolitano et al. (2019). The locations of those transects are depicted if the panel (a) in red lines. Panel (g) corresponds to the observations presented by Lazaneo et al. (2020). Its location is shown in panel (a) (blue line). Altimeter data were obtained in http://marine.copernicus.eu. Navy blue and red rectangles in panel (d) represent the location for the ζ/f distribution, and the T-S diagram in Figure 4.4.

We verify the modeled surface circulation by comparing it with geostrophic velocity components obtained by measurements derived from the altimeters (CMEMS, http://marine.copernicus.eu). Here, we estimate the geostrophic velocity components (u_g,

v_g) from the model using the sea surface high output,

$$u_g = -\frac{g}{f}\frac{\partial \eta}{\partial y} \tag{4.1}$$

$$v_g = \frac{g}{f}\frac{\partial \eta}{\partial x} \tag{4.2}$$

where g is the gravitational field, and f is the planetary vorticity. We filter the resulting geostrophic velocity with a low pass filter (8 days) to remove the high temporal variability compared to the altimeter data.

As shown in Figure 4.3, the modeled geostrophic circulation of the numerical experiment is well-represented by the model. The annual average of the geostrophic velocity field ($\left|U_g\right| = \overline{\sqrt{u_g^2 + v_g^2}}$), near the VTR depicts the SEC meandering pattern passing through the VTR (Figures 4.3a and 4.3b). We track the Brazil Current by its signature of mean kinetic energy (MKE= $(\overline{u_g}^2 + \overline{v_g}^2)/2$) along the South American continental margin. This signature is limited by the isobaths of the continental slope (h $\sim$ 200 - 1000 m in both modeled and AVISO maps, Figures 4.3c and 4.3d). Since the submesoscales contain greater amounts of kinetic energy and spatial variability compared to the motions resolved by altimeter measurements, we expect the model output to be more energetic and variable than the AVISO counterpart.

We validate the BC structure in the numerical domain by comparing the modeled velocity with synoptic measurements reported by Lazaneo et al. (2020) and Napolitano et al. (2019). The cross-transect velocities reported in the aforementioned studies captured a typical snapshot of the Brazil Current and the Intermediate Western Boundary Current (BC-IWBC) system (e.g., Silveira et al., 2004) at 21.5°S and 19°S. The BC-IWBC system is well-reproduced in our model in all three analyzed transects, as shown in Figures 4.3e–4.3g. South of the VTR, the Brazil Current in Figures 4.3e and 4.3g is a poleward jet

barely reaching 400 m, while the Intermediate Western Boundary Current is an equatorward flow underneath the Brazil Current. North of the VTR, both BC and IWBC appear detached from the slope owing to their meandering patterns (Costa et al., 2017; Napolitano et al., 2019). Indeed, the monthly average of this transect crossed the feature known as the Abrolhos Eddy (Soutelino et al., 2011). The modeled velocity magnitude of the BC and IWBC (-0.4 m s^{-1} and 0.2–0.3 m s^{-1}, respectively) agrees with the previously reported measurements. Moreover, the position of both western boundary flows cores and the behavior of both jets show that our model reproduces the western South Atlantic Ocean circulation correctly.

Next, to validate the temperature and salinity structures near the VTR, we present the modeled water characteristics in the T-S diagram depicted in Figure 4.4a. Here we include the temperature and salinity data set from the recent observations (L21) which described the occurrence of SCVs in the vicinity of the VTR. According to Mémery et al. (2000) the top 500 m of water column is composed of Tropical Water – marked by the 1025.6 kg/m^3 isopycnal – and the South Atlantic Central Water in pycnoclinic levels – marked by the 1026.9 kg/m^3 isopycnal. Thus, the modeled temperature and salinity signatures depicted in Figure 4.4a are in accordance with the descriptions in the literature. In addition, we show in Figure 4.4b the average stratification ($N^2 = \frac{\partial b}{\partial z}$, where $b = \frac{-g\rho}{\rho_0}$ is the buoyancy, and $\rho_0 = 1025$ kg/m^3 is the density reference) profiles of the modeled water column near the Columbia Seamount and from the observations presented by L21. We observe a reasonable agreement of between modeled and observed N^2 profiles in the region, with the seasonal pycnocline at about 70 m depth, and the maximum density vertical gradient associated with the permanent pycnocline at about 150–200 m depth.

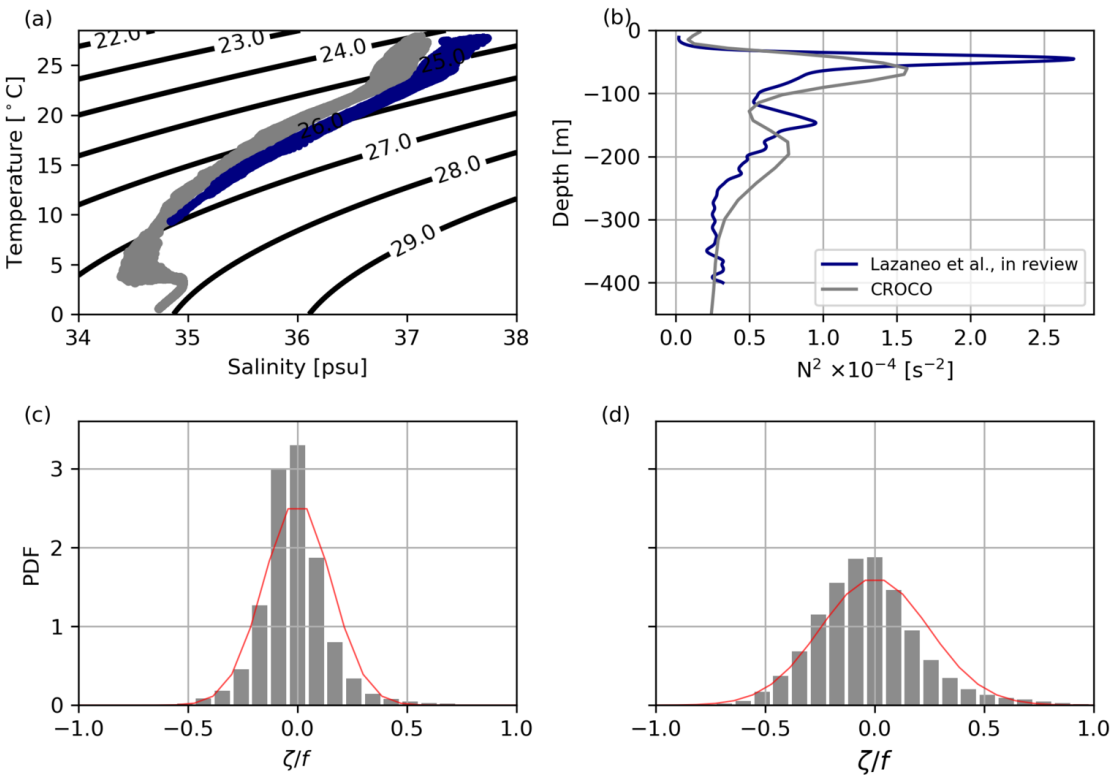

Figure 4.4: (a) T-S diagram and (b) the average profile of the stratification from the region shown in the red rectangle in Figure 4.3b. Gray dots/curve represent the model output, and the navy blue dots/curve represent the data set presented by L21. Distribution of ζ/f in the region (c) without the topography influence and (d) considering the VTR topography. Both regions are depicted in Figure 4.4b.

Finally, we evaluate the ability of our model to simulate submesoscale phenomena based on the probability density function (PDF) of the gradient Rossby number (Ro; Figures 4.4c and 4.4d)

$$Ro = \frac{\zeta}{f} = \frac{\left(\partial_x v - \partial_y u\right)}{f}, \tag{4.3}$$

where Ro $\mathcal{O}(1)$ is indicative of submesoscale dynamics (Mahadevan and Tandon, 2006). Our results show the occurrence of $\mathcal{O}(1)$ Ro, and the asymmetry in the PDF of Ro values (Figures 4.4c and 4.4d). Here, we compute the Ro values within the mixed-layer of two regions. The first region is away from the VTR and the western boundary flow (Ocean Region – OR). And the second region includes the VTR islands and seamounts (Ridge Region – RR). These regions are depicted in Figure 4.3d. At the OR, the modeled vorticity presents values at the submesoscales with a predominance of cyclonic motions

– skewness of 1.23. The tail of Ro in the PDFs towards cyclonic motions exemplifies the ability of our model to reproduce submesoscale phenomena (e.g., Calil and Richards, 2010; Molemaker et al., 2015; Rudnick, 2001). On the other hand, the PDF for the RR highlighs the importance of topography toward anticyclonic motions – with a skewness of 0.59. The the higher frequency of occurrence of anticyclonic motions of large Ro is indicative that the VTR region is prone to submesoscale instabilities (see Napolitano et al., 2020; Thomas et al., 2016).

SCV formation at the Trindade Island

This Section shows how SCVs are formed at the Trindade Island wake. We choose one particular scenario of eddy-island interaction from the numerical simulation, which is similar to the pre-conditions described by L21 from observations.

Submesoscale Vortical Wake

At the beginning of the fourth year of simulation (austral summer, January 6), we observe a SEC mesoscale cyclonic meander approaching the north of Trindade Island (Figure 4.5a). This mesoscale cyclonic meander is characterized by: i) $KE > 0.04\,\mathrm{m^2 s^{-2}}$ at its edges (where $KE = \frac{1}{2}(u^2 + v^2)$), ii) a radius of 50 km, and iii) being centered at 19.75° S and 29.6° W.

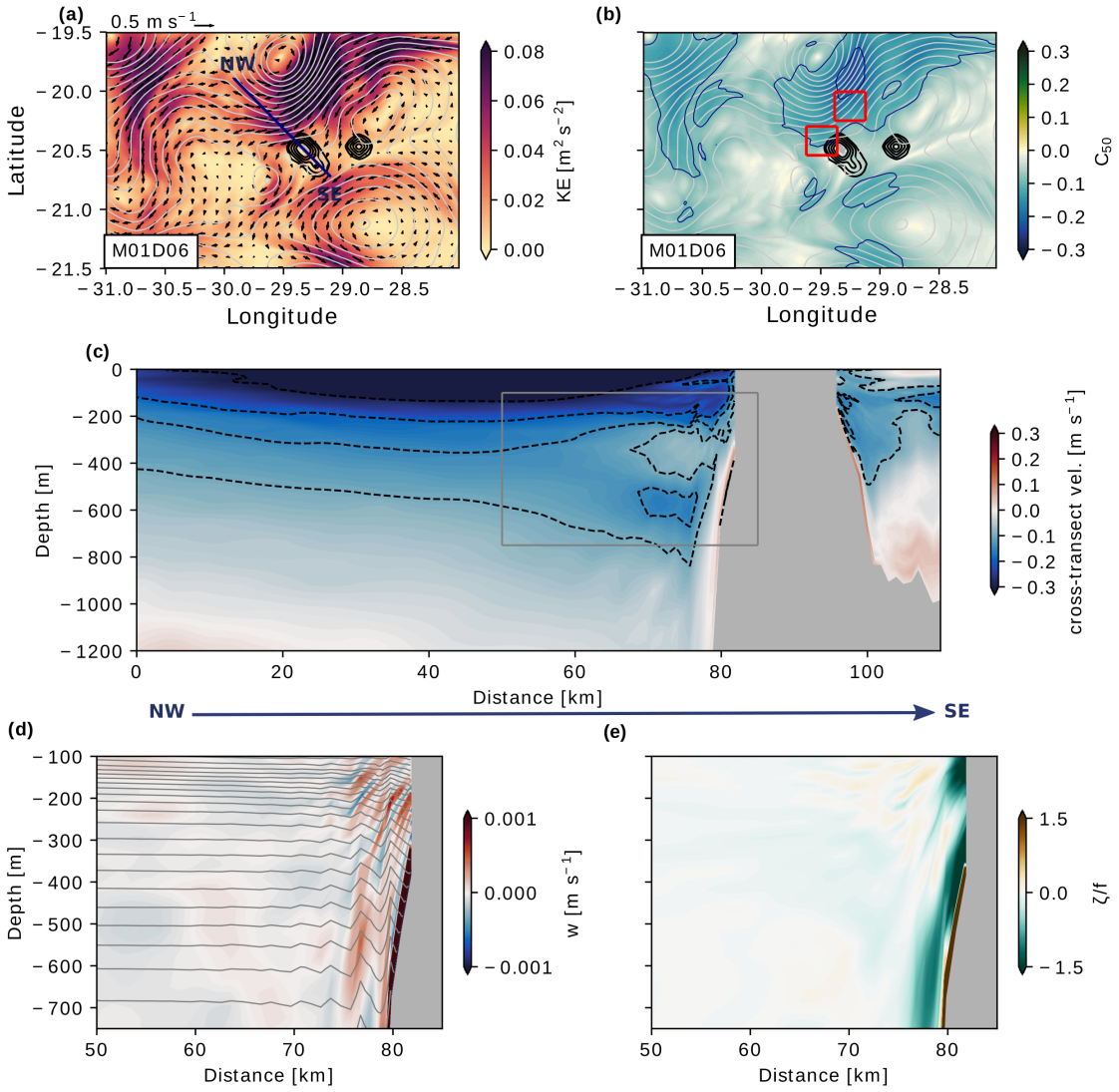

Figure 4.5: Snapshot of the (a) surface kinetic energy ($KE = \frac{1}{2}(u^2 + v^2)$) field from day 6 of the fourth year of simulation, where vectors represent the horizontal components of the surface velocity. Snapshot of the surface cyclogeostrophic Rossby number field (eq. 4.4), considering $r_0 = 50\,\text{km}$ (C_{50}). The gray isolines in panels (a) and (b) represent the respective sea surface height, and black contours are isobaths (3000, 2000, 1000, 500 and 250 m). Blue contours in panel (b) represents isolines of C_{50} (0.1 and 0.2) Panel (c) represents the vertical section of the cross-transect velocity day 6 of the transect presented in blue in panel (a). Black solid (dashed) contours represent the northeastward (southwestward) horizontal velocity. The location of the transect (blue line in panel (a)) correspond to an orthogonal section from the SEC flow (monthly-averaged, January). Red boxes in panel (b) represent the locations where the energy conversion analysis is conducted in Section 3.3. Panels (d) and (e) is the vertical velocity and the vertical relative vorticity scaled by the planetary vorticity, respectively, for the area depicted in the gray rectangle in panel (c).

The relevance of its cyclonic curvature is assessed by computing the cyclo-geostrophic Rossby number (C)

$$C = \frac{v_\theta}{f r_0}\,, \tag{4.4}$$

where v_θ is the angular horizontal velocity and r_0 is the eddy curvature radius. The instantaneous values of $C \sim 0.1-0.2$ for an $r_0 = 50$ km are obtained for the portion of the cyclonic meander presenting the most intense kinetic energy (Figures 4.5a and 4.5b). Similar numbers to those simulated for the SEC have been reported for different regions in the ocean. According to Liu and Rossby (1993), the Gulf Stream meanders present $C \sim 0.1-0.3$, while Niiler et al. (2003) shows that $C \sim 0.25$ for the Kuroshio. Centrifugal forces can arise from the tilting of the vorticity vector by the meander curvature, which can potentially destabilize the meandering edge (Buckingham et al., 2020). Thus, the non-negligible modeled C values highlight the importance of centrifugal forces to the SEC meander stability even before hitting the island (Figure 4.5b). On the other hand it is known that the centrifugal-force influx from the upstream meander is not a necessary condition for the wake destabilization (see Srinivasan et al., 2019). However, this influx can act as an additional input to make the system less stable as it interacts with the topography. The SEC ever-meandering pattern correctly reproduced by our model causes temporal changing of the angle of attack relative to the island. Successive meanders can hit it with different phases. As consequence, the coherent vortices can be generated at a different locations near this island at different times.

In other to verify the influence of the Trindade Island on the incoming meandering flow, we first choose a transect orthogonal to the monthly average position of the SEC, depicted in Figure 4.5a. On day 6 of the fourth year of the simulation, we observe the cross-transect velocity of the cyclonic meander leaning against the island northern

slope. As the meander hits the island, bottom friction changes the velocity at the slope (Figure 4.5b), resulting in a horizontally sheared, divergent flow. The associated up-slope flow is indicated in Figure 4.5c, accompanied by the perturbation of the density field. The dynamic consequence of such interaction is the generation of vortical filaments of Ro $\mathcal{O}(1)$ (Figure 4.5d), which are advected downstream by the larger-scale flow (Figure 4.6). This process was investigated by Hasegawa et al. (2004), who stated that the flow blockage by the island mass induces horizontal and vertical flow separation, and subsequently the creation of a vortical wake.

In Figure 4.6 we show the flow separation and the vortical wake evolution to form an anticyclonic SCV at the lee of the Trindade Island in a sequence of daily snapshots of the subsurface Ro field. On day 6, we observe the beginning of the generation of the anticyclonic filament adjacent to the north face of the Trindade Island slope (Figure 4.6a). On day 11, the anticyclonic vortical filament is elongated ($\zeta <$ -0.5f) downstream of the island and starts rolling up (Figure 4.6b). On day 22 (Figure 4.6c), the filament roll-up is completed and the SCV is formed. Since the SCV is developed in the anticyclonic lobe of the cyclonic SEC meander through interaction the northern slope of the Trindade Island, its polarity is anticyclonic as sketched in Figure 4.1. The result of the SCV formation process displayed in Figure 4.6 corroborates those described by Srinivasan et al. (2019) for islands and seamounts, as well as those resulting from other types of topographic features (D'Asaro, 1988; de Marez et al., 2020; Gula et al., 2019; Molemaker et al., 2015; McWilliams, 2016). In summary, the process of SCV generation occurs in the following sequence of events: (i) generation of relative vorticity in the bottom boundary layer, (ii) filament separation from the slope, (iii) vigorous instability, (iv) mixing, and finally, (v)

the formation of SCVs. A diagnosis of the instability phenomenon and its role in the SCV formation is addressed in the next Section (Section 3.2).

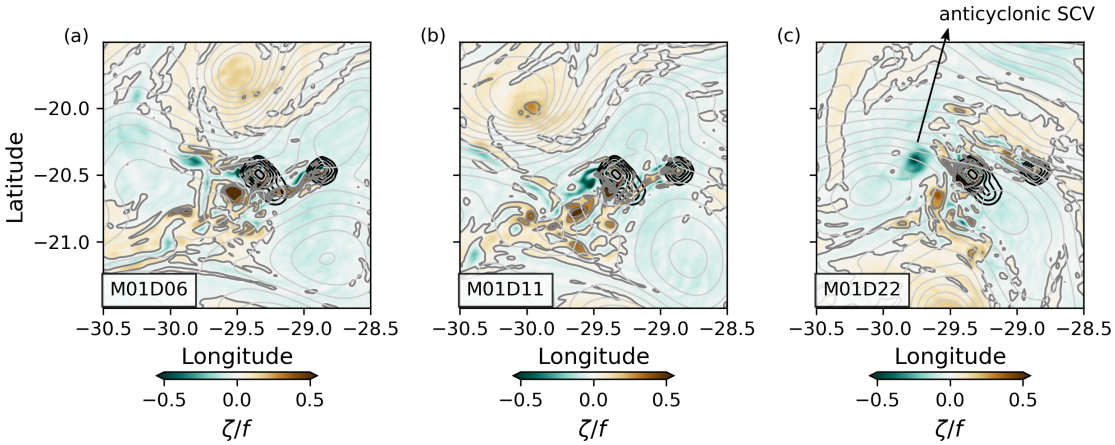

Figure 4.6: Snapshots of the horizontal slice of ζ/f at z = -230 m. Panel (a) represents day 6, when the SEC meandering hit the Trindade Island. Panel (b) represents day 11, when the anticyclonic filaments at downstream are wrapping up. Panel (c) represents day 22, showing the recently formed SCV attached to the basic flow. Gray contours represent isolines of η, and black contours are isobaths (3000, 2000, 1000, 500 and 250 m).

Ertel's Potential Vorticity

Ertel's potential vorticity theorem is a powerful tool for analyzing fluid motion and its potential to develop unstable flow, mainly when the fluids' baroclinicity is well-resolved as is the case in our submesoscale-resolving simulation. A variety of instabilities can arise when the PV (q) takes the opposite sign of the Coriolis parameter (Hoskins, 1974),

$$fq = f\left(f\hat{k} + \nabla \times \mathbf{u}\right).\nabla b < 0. \tag{4.5}$$

This criterion is also valid for the southern hemisphere, where $f < 0$). The PV equation is multiplied by f to make Equation 4.5 more general and hemisphere-independent.

The different types of instabilities depend on the predominance of one of the terms that constitute the scalar quantity q, which is responsible for lowering the PV value.

By assuming that $\frac{\partial w}{\partial(x,y)} << \frac{\partial(u,v)}{\partial z}$ in the interior ocean, we can split Equation 4.5 in two different parts given by

$$fq = f\underbrace{(f\hat{k}+\zeta)N^2}_{q_{vert}} + f\underbrace{\left(\frac{\partial u}{\partial z}\frac{\partial b}{\partial y} - \frac{\partial v}{\partial z}\frac{\partial b}{\partial x}\right)}_{q_{bc}}, \tag{4.6}$$

and separate the mechanisms that drives instability. The first term on the right-hand side emphasizes the role of vertical vorticity and stratification. Whether q_{vert} dominates over q_{bc}, two different instabilities may arise: i) if $f(f\hat{k}+\zeta)N^2 < 0$, N^2 can be negative giving rise to gravitational instability, or ii) if $N^2 > 0$, ζ should be anticyclonic, giving rise to centrifugal instability (Gula et al., 2015, 2019; McWilliams, 2016; Thomas et al., 2013). On the other hand, the second term on the right-hand side (q_{bc}) emphasizes the flow baroclinicity. The combination of prominent horizontal buoyancy gradient and tilted vortical tube can overcome the strength of the vertical vorticity/stratification resulting in baroclinic instabilities involving vertical vorticity of either polarity – cyclonic or anticyclonic (see Napolitano et al. (2020) and Thomas et al. (2013) for details). Here, we are assuming that the flows are in geostrophic balance. For a geostrophic flow, $\mathbf{U_g}$, it can be displayed using the thermal wind relation that reduces q_{bc} to

$$q_{bc} = -f\left|\frac{\partial \mathbf{U_g}}{\partial z}\right|^2 = -\frac{1}{f}\left|\nabla_h b\right|^2. \tag{4.7}$$

Figures 4.7a–4.7c show three snapshots of the PV field subsurface. The snapshots exhibit the spatial and temporal evolution of low PV filaments intersecting the local topography during the SEC meander crossing of the Trindade Island. Figures 4.7d–4.7f display vertical sections of fq, fq_{bc}, fq_{vert} along the detaching filament at day 11 of the fourth year of the simulation. The comparison between the three latter panels clearly shows that the low PV strip (sometimes negative) is driven by q_{vert} (Figure 4.7f), and that it corresponds to the anticyclonic vortical filament in the wake of the island captured in

Figure 4.6. The combination of the weakly-stratified environment (not shown) and the anticyclonic vorticity, which achieves values comparable to the planetary vorticity, is responsible for reducing the PV values. On the other hand, the q_{bc} is a negative quantity. It indicates that the baroclincity of the flow always reduce the PV.

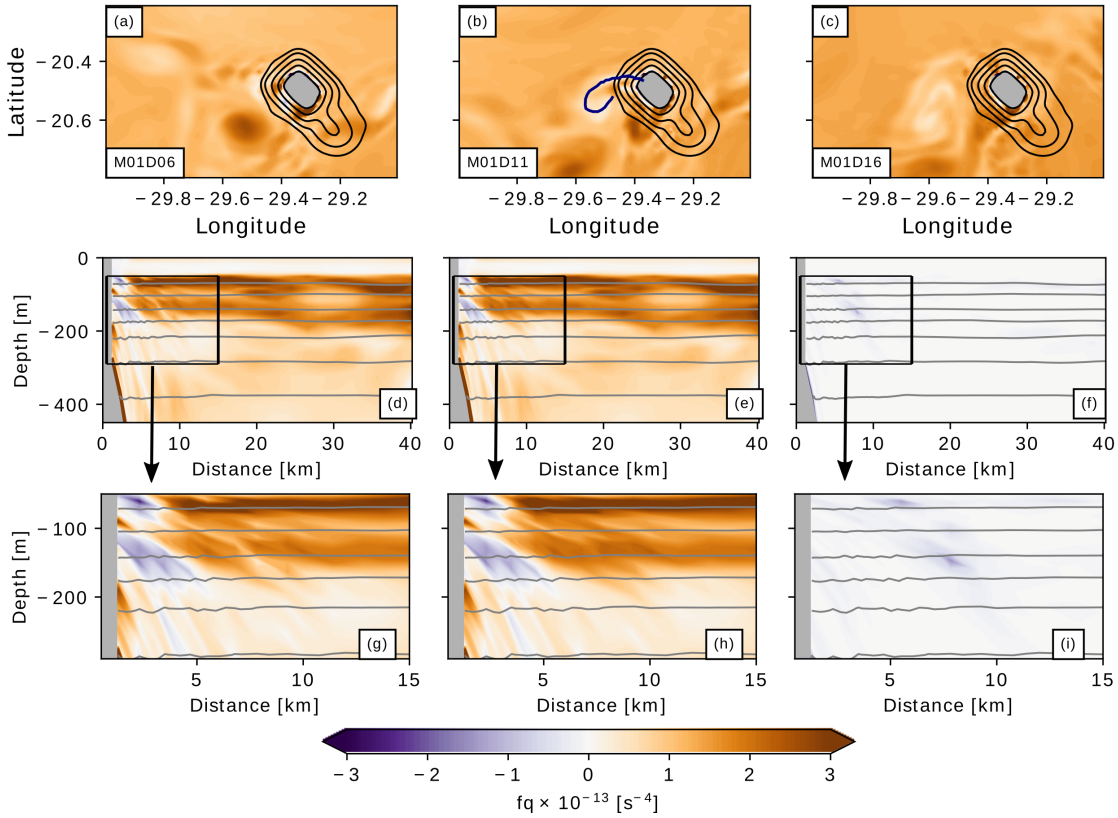

Figure 4.7: Panels (a), (b) and (c) are snapshots of fq at $z =$ -230 m showing the evolution of filaments of low PV which evolves to the SCV formation. Black contours are isobaths. Panels (c), (d) and (e) represent the vertical section of the low PV filament depicted in panel (b). They represent the (d) total PV as in Equation 4.5, (e) the role of the vertical vorticity and stratification on the total PV, and (e) the role of the baroclinicity of the flow. Panels (g), (h), and (i) are the zoom-in of panels (d), (e) and (f), respectively, with the intent to highlight the near-topography region where baroclinic instability dominates over centrifugal instability. Gray contours are sigma levels.

It is evident from Figure 4.7 that the unstable flow at wake of the island is mainly driven by q_{vert}, but the baroclinicity (q_{bc}) triggers strong mixing locally lowering the Richardson number (not shown). As first suggested by D'Asaro (1988), SCVs can be generated through PV reduction due to frictional forces and the development of centrifugal instability. The same process is addressed by Gula et al. (2019), which determines the

role of the Charleston Bump on the formation of SCVs in the wake of the bump. Thus, our simulation indicates that the same mechanism addressed by these former studies also occurs at Trindade Island.

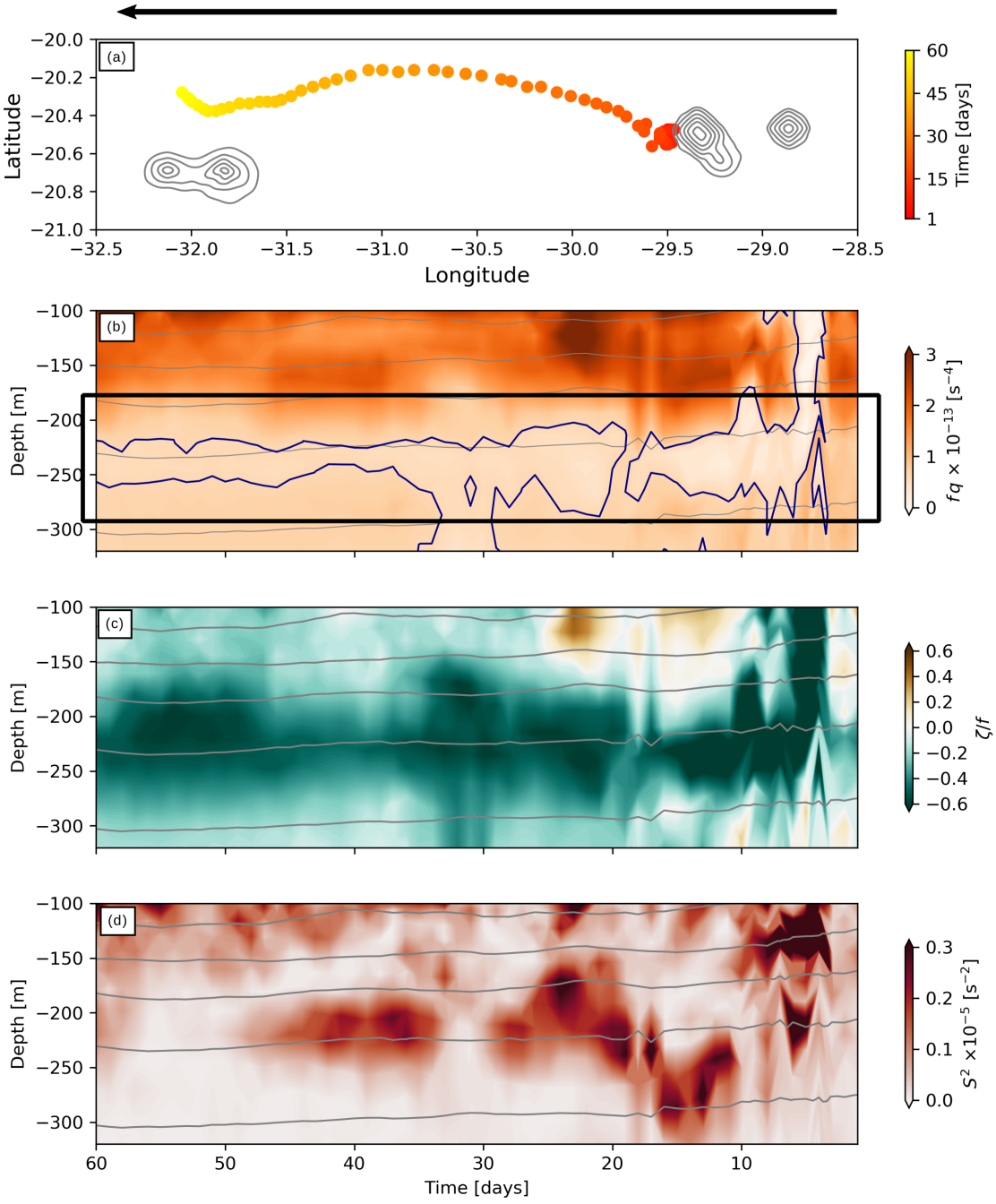

Figure 4.8: (a) Trajectory of the centroid, defined as the minimum value of ζ/f within he SCV at $z =$ -230 m. Vertical profile of (b) the PV, (c) ζ/f and (e) the shear intensity ($S^2 = (\partial u/\partial z)^2 + (\partial v/\partial z)^2$) at the location of the centroid of the SCVs. Blue contours in panel (b) represents the values of 0.6×10^{-13} s^{-4}.

To verify whether the low PV signature of such an anticyclonic SCV is kept after its detachment from the island wake, we track this SCV for two months following its centroid. Here, we define the centroid of the SCV as the patch of most intense vertical vorticity within the SCV. The trajectory of the SCV is shown in Figure 4.8a. The SCV departs from Trindade Island wake and it takes about two months to reach the region near the Columbia Seamount, about 350 km west of its origin site. The trajectory of the SCV centroid follows a SEC meander stream line. The SCV once formed and detached is clearly advected by the mesoscale structure associated with the SEC. This is consistent with the findings by Dewar and Meng (1995), where the advection of SCVs are mainly driven by larger scale flows since the β effect over their small sizes is either reduced or negligible. L21 observed a pair of SCVs near the Columbia Seamount and embedded in a SEC meander. The results of the present simulation suggest that these SCVs eventually could have been generated remotely at the Trindade Island. Indeed, the time range of the SEC meander tracked by the daily-output from altimeters in L21 is in agreement with the time scale of the westward propagation of a mesoscale eddy departing from the Trindade Island towards the Columbia Seamount in our model.

As the SCV travels to the west and gets away from the Trindade Island, its signature becomes more evident due to its contrast with surrounding waters. As a consequence of the flow-topography interaction at about day 6, the PV is reduced to values around zero occupying the top 300 m (Figure 4.8b). After a few days, the marginally stable low PV tongue is advected to the west at pycnoclinic level (between 200-300 m depth). We observe that the SCV conserves the PV along its pathway. We also see the subsurface signature of the SCV become more evident by observing the Ro number of the structure (Ro $\mathcal{O}(1)$), which ultimately means that the anticyclonic vorticity is the main factor to main-

tain the low PV along the tracked period (Figure 4.8c). Furthermore, we notice patches of intense vertical shear squared ($S^2 = (\frac{\partial u}{\partial z})^2 + (\frac{\partial v}{\partial z})^2$) related to the SCV trajectory. The relationship of vortical shear layers in a weekly-stratified environment may provide a favorable condition for small-scale processes toward dissipation scales. However, the 1 km resolution of our model does not solve such small-scale processes. In other words, the intense vertical shear in the SCV interior can overcome the stratification, resulting in mixing processes and energy dissipation. The high S^2 value patches can be thought as a proxy to patches of high turbulent energy dissipation. Indeed, this is the structure observed by L21 in their SCVs. This study showed from microstructure observations that the amount of energy dissipation within one SCV is as high as those observed in the mixed-layer. Thus, our results of Sections 3.1 and 3.2 support the hypothesis that: i) the Trindade Island is prone to generate SCVs due to the eddy-topography interaction, which ii) can be advected by the SEC towards western portions of the ridge, and iii) may provide mixing to the ocean interior.

Energy Analysis

It is evident from the previous Section that the SEC interacts with the Trindade Island and SCVs are formed through this interaction. Perturbations imposed by the bottom drag of the island exert strong influence on the flow, yielding the generation of those submesoscale features. Once submesoscale phenomena are generated, energy is transferred from balanced to unbalanced flows (McWilliams, 2016).

To investigate the energy sources responsible for the SCV generation, we compute the energy conversion terms for the fourth year of simulation for regions upstream and downstream of Trindade Island (the location of such regions are depicted in Figure

4.5b). We carry this energy analysis closely following the notation presented by Calil et al. (2021). From the daily-averaged output, we separate all variables as $u = \langle u \rangle + u'$, where brackets denote the annual average and primes denote deviations from those averages. The conversion from mean to eddy kinetic energy (EKE) due to the shear production (SP) is divided into the horizontal shear production (HSP) and the vertical shear production (VSP)

$$SP = HSP + VSP, \tag{4.8}$$

where

$$HSP = -\overline{u'^2}\frac{\partial \overline{u}}{\partial x} - \overline{v'u'}\frac{\partial \overline{v}}{\partial x} - \overline{u'v'}\frac{\partial \overline{u}}{\partial y} - \overline{v'^2}\frac{\partial \overline{v}}{\partial y} \tag{4.9}$$

$$VSP = -\overline{u'w'}\frac{\partial \overline{u}}{\partial z} - \overline{v'w'}\frac{\partial \overline{v}}{\partial z}. \tag{4.10}$$

These terms represent the work of Reynolds stress on the mean shear. The conversion from eddy potential energy to EKE, called the buoyancy production (BP), is defined in terms of the vertical buoyancy flux

$$BP = \overline{w'b'}. \tag{4.11}$$

Hence, the EKE equation, neglecting transport, vertical mixing and horizontal diffusion terms is,

$$\frac{\partial}{\partial t}EKE \; = \; SP \; + \; BP, \tag{4.12}$$

where $\frac{\partial}{\partial t}EKE$ is the EKE local rate of change. Each term of Equation 4.12 is box-averaged within the area depicted in Figure 4.5b and in the 180–280 m depth range. This depth interval corresponds to the occurrence of the SCV described in Section 3.1. The predominance of one of these terms (HSP, VSP, or BP) indicates if the eddy generation mechanism is primarily through barotropic (HSP > 0), baroclinic (BP > 0), or vertical shear (VSP > 0) instability.

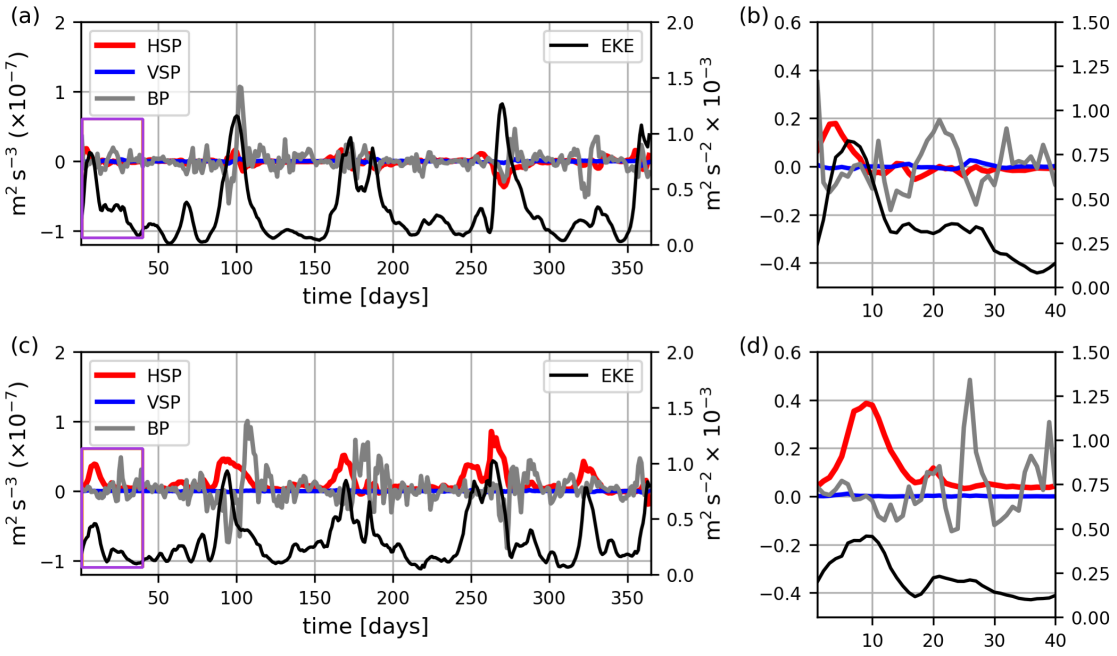

Figure 4.9: Time-series of the terms shown in Equations 4.9–4.11 for (a) the upstream and (c) the downstream areas near the Trindade Island. All terms are calculated within the rectangles shown in Figure 4.5b and averaged between 180 and 280 m depths. This depth range corresponds to the portion of the water column where SCV formation occurred. Panels (b) and (d) zoom into the first 40 days (purple rectangles in panels (a) and (c)), which is the period of SCV occurrence.

Figure 4.9 shows the time-series of each spatially-averaged term along the fourth year of simulation. The EKE peaks are attributed to the kinetic energy input through the passage of mesoscale eddies in the region. But, once the angle of attack of the SEC changes relative to the island location, the position of the lee is also changed. Therefore, there are mesoscale eddies passing through the Trindade Island whose advection effect is not considered in this analysis. On the other hand, co-occurrence of EKE peaks upstream (Figures 4.9a and 4.9b) and downstream (Figures 4.9c and 4.9d) shows multiple events of mesoscale eddy-island interaction.

In general, we observe: i) the predominance of eddy potential energy conversion towards EKE through baroclinic instabilities upstream in the absence of stronger SEC meanders (BP $>$ 0, Figures 4.9a and 4.9b), and ii) the predominance of mean kinetic energy conversion towards EKE through barotropic instabilities downstream (HSP $>$ 0, Figures

4.9c and 4.9d). The occurrence of vertical shear instabilities (VSP), on the other hand, is negligible throughout the year, given that VSP ~ 0 both upstream and downstream. The first peak of EKE in Figures 4.9a and 4.9b corresponds to the passage of the cyclonic meander upstream described along Section 3. During the passage of this meander, we see an increase and the predominance of the HSP term that reaches $0.2 \times 10^{-7}\,\mathrm{m^2\,s^{-3}}$ (Figure 4.9b). This means that barotropic instabilities arise along the meander even before hitting the island. We attribute the rise of HSP upstream to the increase of centrifugal acceleration, which occurs due to the curvature of the meander (see Section 3.1). We also observe that the change of HSP due to the passage of the SEC meanders occurs in all of the EKE peaks captured upstream.

As EKE increases downstream, HSP also increases reaching values two to three times greater than those observed upstream. Whether we look at the first peak of EKE downstream, we observe that HSP reaches $0.4 \times 10^{-7}\,\mathrm{m^2\,s^{-3}}$ (Figure 4.9d). We interpret this peak of HSP as the cause of the SCV formation, since the anticyclonic filaments at submesoscales ($Ro\ \mathcal{O}(1)$) occurs within the downstream box. This is another indication of barotropic instabilities (e.g., Gula et al., 2016), which ultimately are considered a necessary condition for the SCVs' generation (McWilliams, 2016). From the analysis of energy conversion (this Section) and potential vorticity (Section 3.2), the role of the Trindade Island in the development of barotropic instability (e.g., centrifugal instability), and eventually, in the formation of SCVs is evident.

Nevertheless, we examined and explored a single event of SCV formation at the lee of the Trindade Island in all of Section 3. This event represents only one of the several EKE peaks displayed in Figure 4.9. The other peaks and other seamounts along the VTR as possible sites prone to SCV generation are explored next. Moreover, we extend the use

of HSP as a tool for diagnosing SCV formation. We also perform our analysis at different depths and at different isolated topographic features along the VTR. These results are presented in Section 4.

The VTR as a Hotspot for SCV Generation

In this Section, we show that, in addition to the Trindade Island, other seamounts of the VTR also influence of the formation of SCV-like structures. To investigate the occurrence of SCVs at different locations in the VTR and at different depths, we examine the maximum peaks of HSP, which we assume as indicative of barotropic instabilities (c.f., Calil et al., 2021).

As described in Section 3.3, we associate EKE and HSP peaks with the interaction between mesoscale eddies and the topography of the Trindade Island. We understand that this interaction results in the formation of submesoscale filaments, which eventually gives rise to SCVs. In Figure 4.9c, we observe multiple peaks of HSP downstream of the island at different times during the fourth year of our simulation.

We select the EKE-HSP peaks displayed between days 80 and 105, and 160 – 180. Figures 4.10a and 4.10d show the anticyclonic side of the incoming, meandering SEC interacting with the barrier imposed by the Trindade Island. Two anticyclonic SCVs are formed during these peaks as seen in the gradient Rossby number maps in Figures 4.10b and 4.10e. The generation process in both cases very closely resembles that described in Sections 3.1 and 3.2. Anticyclonic vortical patches with $\mathcal{O}(1)$ *Ro* evolve to become anticyclonic SCVs (Figures 4.10b and 4.10e). Vertical sections crossing the center of these SCVs show their low PV signature (Figures 4.10c and 4.10f). Their vertical PV and velocity structures are similar to those reported in the literature (e.g., Gula et al.,

2019, L21). A cyclonic SCV-like structure is detected based on HSP peaks observed during dates 260 – 275 (Figure 4.9c). In this case, we observe that the side of the energetic jet that interacts with the topography slope is cyclonic (Figure 4.10g). As a result, cyclonic vortical filaments of $Ro\ \mathcal{O}(1)$ are developed in the lee of the island (Figure 4.10h). Unlike the anticyclonic SCV, the roll-up of the cyclonic filaments in the lee of the island drives positive anomalies of the PV (Figure 4.10i). In other words, the sense of rotation of the filaments after the flow separation is the same of the Earth rotation, which results in high potential vorticity (see Equation 4.5). Thus, our model results show SCV formation of both polarities between 180 – 280 m in the lee of Trindade Island throughout the whole year as the meandering SEC branch continuously interact with Trindade and Martin Vaz Islands.

Different high Ro patches are detectable in Figures 4.10b, 4.10e and 4.10h. They can be either a consequence of the island-SEC interaction or structures coming from remote locations. However, by following the larger-scale flow pathways in Figures 4.10a, 4.10d and 4.10g, we observe that these flows have previously interacted with the islands. We also note filaments emanating from the islands' lees in all three panels. However, we should point out that not all vortical filaments necessarily evolve to form SCVs. For three SCV-like features described here, and indicated in Figures 4.10b, 4.10e and 4.10h, we present their respective development and evolution in supporting information, Section 5 (Figures 4.12, 4.13 and 4.14).

In order to check whether the SCVs can be generated at different depths than 180 – 280 m range of the previous analysis, we calculate the energy conversion terms for the 600 – 700 m depth range. We observe many defined peaks of high HSP in Figure 4.11a showing that, even at deeper levels, the island exerts influence on the impinging SEC flow.

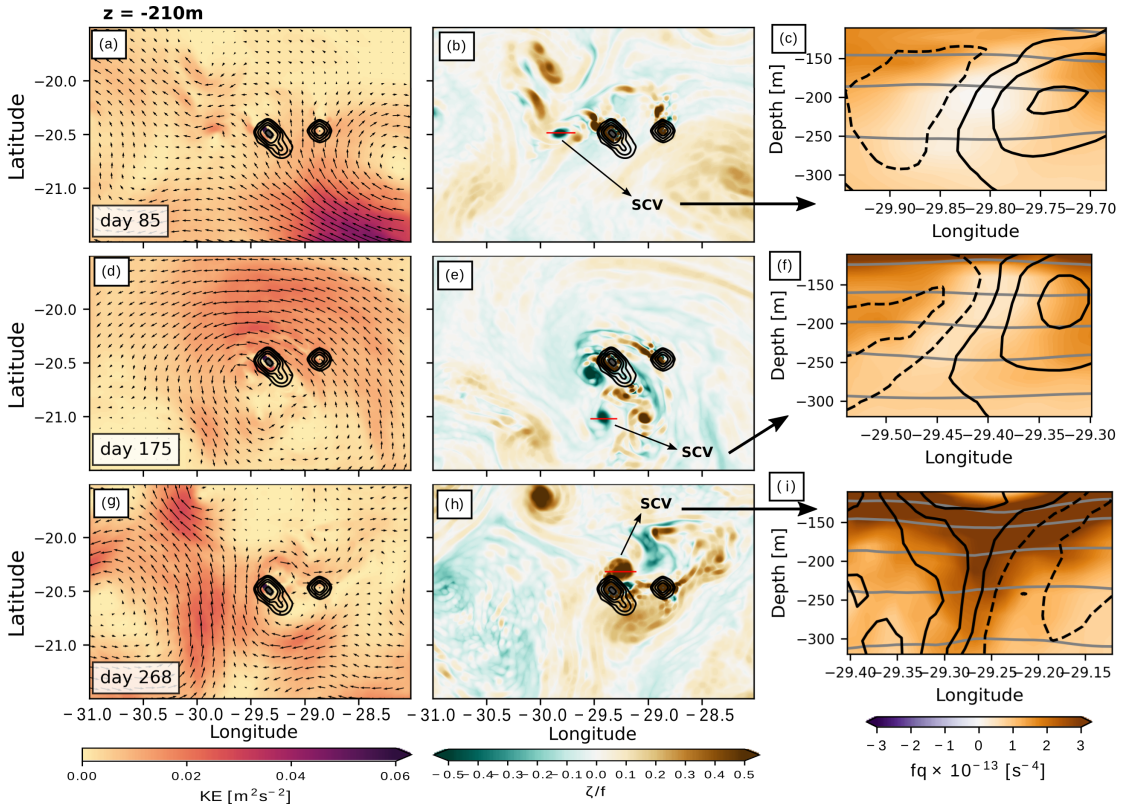

Figure 4.10: Snapshots at z = -210 m depth show periods when the energetic meanders of the SEC (KE, color shading of panels a, d and g), which are computed by the daily velocity field (black arrows), encounters the Trindade Island (black contours). As a consequence, filaments of strong vorticity develop (ζ/f, color shading of panels b, e, and h), evolving into SCVs. According to the polarity of each SCV, they carry signatures of low/high PV (fq, color shading of panels c, f, i) in their cores. The solid/dashed black and gray contours in the zonal transects (located by the horizontal red line in panels b, e and f) are the positive/negative meridional velocities and density, respectively.

It also induces the generation of submesoscale phenomena, which is detected by observing many defined peaks of high HSP in the plot. As an example, Figure 4.11b shows the rise of EKE signal followed by the maximum peak of HSP between 600 – 700 m depth in the lee of the Trindade Island, an indication of barotropic instability. The snapshot of the KE field at z = -650 m, for day 21, shows the presence of a meandering flow interacting with both islands in the region – the Trindade and Martin-Vaz Islands. The consequences of such interaction are depicted in Figure 4.11c, which shows the occurrence of at least five SCV-like structures – three anticyclones and two cyclones.

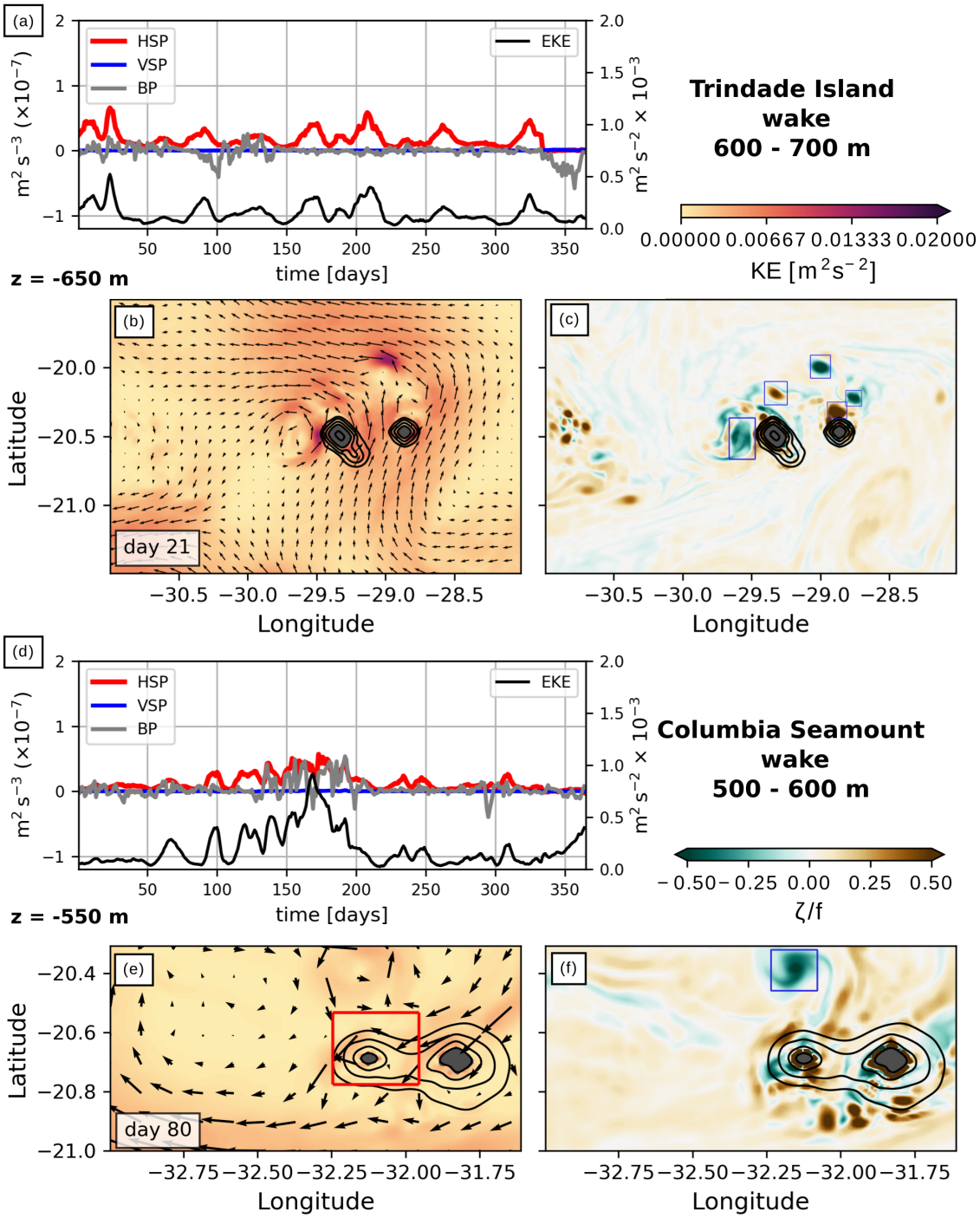

Figure 4.11: Time-series of the terms shown in Equations 4.9–4.11 for lee of (a) Trindade Island and (d) Columbia Seamount. The terms are calculated within the rectangles shown in Figure 4.5b, for Trindade Island and in panel e, for the Columbia Seamount. The depth range of each analysis is indicated in this Figure. Snapshots show periods of eddy-island interaction (KE, color shading of panels b, and e), which are computed by the daily velocity field (black arrows) that results in the formation of SCVs depicted in the ζ/f field by the blue boxes (panels c and f. The depth of the snapshots are indicated in this Figure.)

With an extension of around 900 km, the VTR is characterized by dozens of seamounts that have their tops at about 60–100 m depth. Trindade and Martin Vaz are the only features of the VTR that emerge above the ocean surface. We described SCV formation in both the intra- and subpycnoclinic portions of the water column, depths which are below the average top of all the other seamounts. As the SEC flows almost zonally through the entire ridge, it is likely that the processes involving SCV generation occur in the lee of several other topographic features. To investigate this possibility, the energy conversion analysis described in Section 3.3 is repeated, for the Columbia Seamount (20.7° S 32°W) wake, between 500 – 600 m (the area, which this analysis covers is represented in Figure 4.11e). This depth range is chosen for this analysis to ensure the local topography effect. We observe that the time-series of the EKE and HSP in the Columbia Seamount wake shows the same pattern of those observed nearby the Trindade Island (Figure 4.11c). This indicates that barotropic instabilities may occur in the interior ocean because of the SEC flow blockage by the seamount. Here we choose one event of SCV generation to exemplify that the seamount is also prone to generate SCV-like structures. During the period comprising of days 76 – 115 we observe a peak of HSP and EKE, as in all other cases described in this work (Figure 4.11d). The snapshot of the KE field at z = -550 m, on day 80 shows the presence of a cyclonic meander in the north face of the seamount slope (Figure 4.11e). This interaction results in the formation of an anticyclonic SCV centered at 24.04° S 32.2° W. This SCV was formed at the seamount and advected northward by the horizontal velocities associated with the cyclonic circulation of the SEC meander.

Our model results thus support the hypothesis that the VTR is a hotspot for the generation of both cyclonic and anticyclonic SCVs. Not all HSP peaks necessarily gener-

ate an SCV but they show the barotropic instabilities and show that roll-up of detaching PV filaments can form SCVs. Finally, our simulation highlights the importance of flow-topography interactions in generating such SCVs along the VTR. These structures can wander in the interior ocean for months to years carrying water properties from their generation sites (D'Asaro, 1988; McWilliams, 1985, 2016).

Summary and Final Remarks

In this study, a high-resolution numerical model is employed to simulate the dynamics of the western South Atlantic circulation and the interaction of the South Equatorial Current with a quasi-zonal seamount chain at about 20.5°S, the VTR. In terms of the model validation, both the modeled BC and the mesoscale eddy-rich SEC agree with the available data set and previously reported studies. This enables us to use the simulation to investigate the role of the topography on the generation of submesoscale vortices, the SCVs. From this simulation, we observe that when energetic, meandering SEC collide with the islands and seamounts of the VTR, submesoscale vortices can be generated in the topography's wake, and are advected westward by the SEC.

We initially focus on describing the SCV generation through flow-topography interaction in one event simulated in the fourth year of the simulation (we considered the first three years as spin-up) starting day 6 when a SEC meander approaches the Trindade Island slope. This event shows the formation of an anticyclonic SCV in the intrapycnocline (in the 180 – 280 m depth range). We observed the inshore edge of the anticyclonic SEC meander passing tangentially to the island north slope and defining the polarity of the vortical filaments downstream. Snapshots of the gradient Rossby number showed the formation of vortical filaments rolling up and ultimately resulting in the generation of an

anticyclonic SCV. Since the polarity of the planetary vorticity is opposite to the formed vortical wake, strips of low PV intersecting the boundary were generated downstream driven by the vertical vorticity/stratification. Thus, as the the anticyclonic SCV detached itself from the island wake, it was advected by the SEC toward the South American continent. The anticyclonic SCV carried low PV values in its interior along its trajectory. On the other hand, the generation of cyclonic SCVs due to the eddy-island interaction, requires an inshore cyclonic edge interacting with the topography. For these cases, the polarity of the relative vertical vorticity is the same as the planetary vorticity, which results in positive PV anomalies. However, the energy source for the SCV occurrence of both polarities comes from the horizontal shear production. We observe that the horizontal shear production term is indicative of the occurrence of SCV generation with both polarities. Indeed, when plotting the energy source terms (HSP, VSP and BP), we observed intermittent high HSP peaks throughout the analyzed year of the simulation. We were able to identify the peak associated to the SCV formation and to propose the occurrence of a HSP peak as tool to diagnose a likely coherent vortex generation.

By repeating the energy conversion analysis to other regions and other depths along the VTR, we diagnosed that regardless of the topographic feature or depth, vortices are often and continuously generated (simulated) in the ridge at both intra- and subpycnoclinic levels. In conclusion VTR is a hotspot for SCV generation in western South Atlantic.

Simulation presented here show that the SCVs carry potential and relative vorticity signatures in their cores, as well as vertical shear anomalies. This may establish a donwscale energy cascade by the development of small-scale processes as patches of intense vertical shear inside SCVs, where stratification is low, are indicative of ocean mixing

and energy dissipation (L21). This hypothesis is supported by microstructure measurements inside an SCV in the VTR (L21), where the authors estimated that the amount of energy dissipation inside the SCVs is comparable to the dissipation rates observed in the mixed layer.

While this study does not explore the SCVs generation frequency, the HSP peak time series yields a rough estimate of the generation of these submesoscale features in the region surrounding VTR. Since not all events of barotropic instability yield SCV, the number of HSP peaks represent an upper bound for the estimate of SCV generation.

Supporting Information

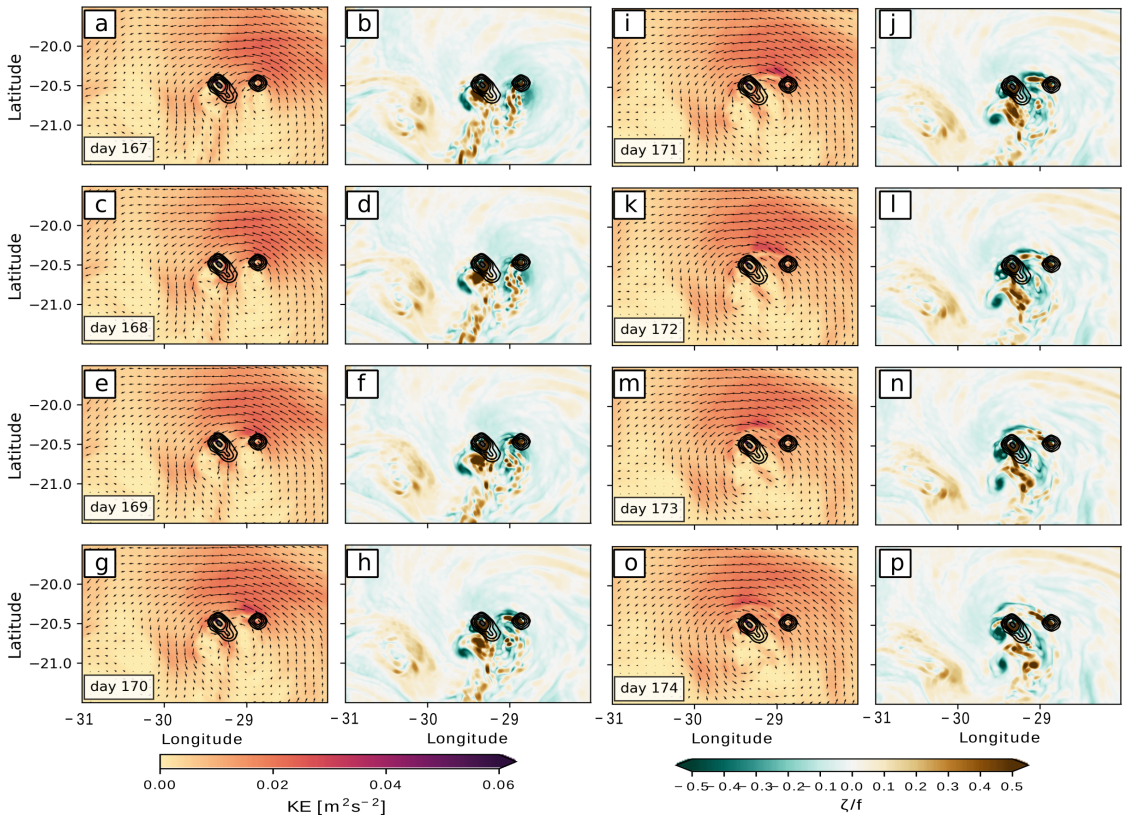

Figure 4.12: Temporal and spatial evolution of the vortical filaments downstream of the Trindade Island leading to an SCV formation. Here we show the SCV formation event shown in Figures 10 a and b. (a, c, e, g, i, k, m, o) Daily snapshots of the kinetic energy at z=-210m depth (background color)with its respective horizontal velocity field (black arrows). (b, d, f, h, j, l, n, p) Daily snapshots of the gradient Rossby number at z=-210m depth (background color). Black contours represent the isobaths of the Trindade and Martin-Vaz Islands.

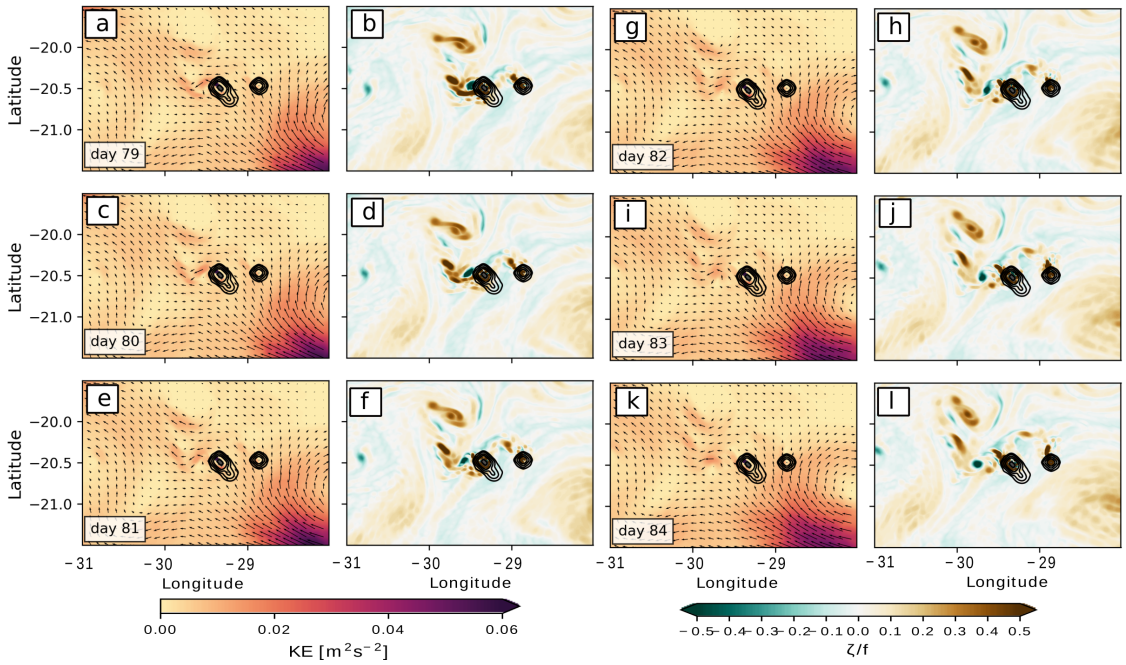

Figure 4.13: Temporal and spatial evolution of the vortical filaments downstream of the Trindade Island leading to an SCV formation. Here we show the SCV formation event shown in Figures 10 d and e. (a, c, e, g, i, k) Daily snapshots of the kinetic energy at z=-210m depth (background color)with its respective horizontal velocity field (black arrows). (b, d, f, h, j, l) Daily snapshots of the gradient Rossby number at z=-210m depth (background color). Black contours represent the isobaths of the Trindade and Martin-Vaz Islands.

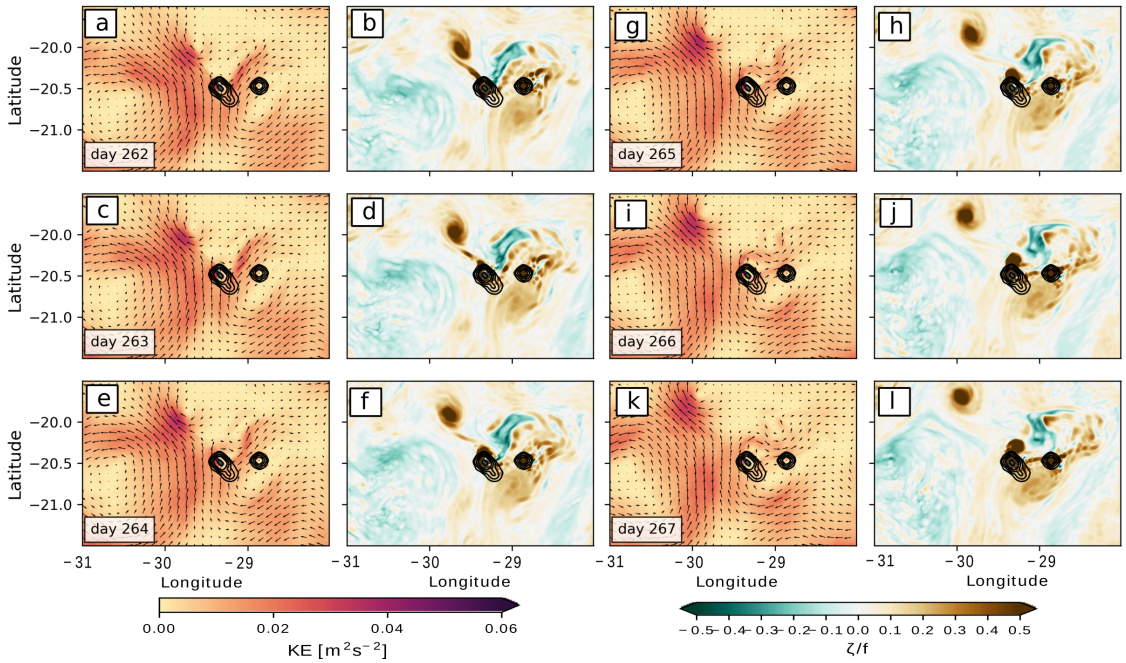

Figure 4.14: Temporal and spatial evolution of the vortical filaments downstream of the Trindade Island leading to an SCV formation. Here we show the SCV formation event shown in Figures 10 g and h. (a, c, e, g, i, k) Daily snapshots of the kinetic energy at z=-210m depth (background color)with its respective horizontal velocity field (black arrows). (b, d, f, h, j, l) Daily snapshots of the gradient Rossby number at z=-210m depth (background color). Black contours represent the isobaths of the Trindade and Martin-Vaz Islands.

CHAPTER 5.

FINAL REMARKS

In this dissertation, we addressed two different mechanisms that transfer energy toward dissipation scales. First, we investigated the potential for turbulence and mixing within the reverse flow of the Brazil Current and the Intermediate Western Boundary Current (BC-IWBC) – the two western boundary currents of the South Atlantic Ocean. Second, we investigated the occurrence and the generation of subsurface submesoscale vortices along the Vitoria Trindade Ridge owing to the interaction of the south branch of the South Equatorial Current with the shallow seamounts and islands of the ridge.

Regarding the potential of the BC-IWBC to develop turbulence and mixing, we show that the enhancement of the vertical shear in pycnoclinic levels can overcome the stabilizing effect of the stratification leading to mixing. Unprecedented microstructure measurements in the region show that the energy dissipation at the interface of the Tropical Water – carried by the BC – and the South Atlantic Central Water – carried by the IWBC at this latitude (21.6°S) – can reach greater values allowing vertical turbulent fluxes. This implies a potential enhancement of biological activity through the additional supply of nutrients in the euphotic zone.

Now, about the occurrence of submesoscale vortices in the Vitória-Trindade Ridge (VTR), we captured two adjacent Submesoscale Coherent Vortices (SCV) near the Columbia Seamount. Both structures present the same dynamical regime. That is, they present low potential vorticity in their cores – scaled by $f/(\overline{f^2N^2})$ to avoid hemispheri-

cal dependence –, which means a stable regime but prone to submesoscale instabilities. We observe that low potential vorticity in the core of the SCVs is driven by the weakly-stratified and vertical vortical layers. Despite the same dynamical regime, they present small deviations from the temperature and salinity of the surrounding waters. It is indicative that they could be formed out of the region of observation. Moreover, we show that the amount of energy dissipation inside the SCV captured by our microstructure profiler is comparable to the dissipation rates observed in the mixed layer.

In order to verify if the VTR is prone to generate SCVs, we employ a regional numerical model with high horizontal resolution. Through the interactions of the meanders of the SEC with the shallow seamounts and islands of the ridge, we observe the flow separation downstream the isolated topographic features by the formation of vertical vorticity filaments of $Ro\ \mathcal{O}(1)$. Eventually, the vortical filaments roll up and evolve to the SCV formation. The polarity of such SCVs is determined by the side of the inshore edge of the SEC that interacts with topography. Thus, both cyclonic and anticyclonic SCVs are formed in the VTR. We diagnose that, regardless of the topographic feature or depth, SCVs are often generated in the ridge. For that reason, we conclude that the region can be considered a hotspot of SCV formation. Once they are detached from the topography, they are advected by the SEC toward the South American continent.

Finally, we highlight the importance of the western South Atlantic Ocean regarding the development of small-scale processes and energy dissipation. The region is key to the comprehension of the ocean energy budget.

Bibliography

Alberoni, A. A., I. K. Jeck, C. G. Silva, and L. C. Torres, 2019: The new Digital Terrain Model (DTM) of the Brazilian Continental Margin: detailed morphology and revised undersea feature names. *Geo-Marine Letters*, doi: 10.1007/s00367-019-00606-x.

Assassi, C., and Coauthors, 2016: An index to distinguish surface- and subsurface-intensified vortices from surface observations. *Journal of Physical Oceanography*, **46 (8)**, 2529–2552, doi: 10.1175/JPO-D-15-0122.1.

Balsley, B. B., G. Svensson, and M. Tjernström, 2008: On the scale-dependence of the gradient Richardson number in the residual layer. *Boundary-Layer Meteorology*, **127 (1)**, 52—-72, doi: https://doi.org/10.1007/s10546-007-9251-0.

Boccaletti, G., R. Ferrari, and B. Fox-Kemper, 2007: Mixed Layer Instabilities and Restratification. *Journal of Physical Oceanography*, **37 (9)**, 2228–2250, doi: https://doi.org/10.1175/JPO3101.1.

Boebel, O., R. E. Davis, M. Ollitrault, R. G. Peterson, P. L. Richardson, C. Schmid, and W. Zenk, 1999: The Intermediate Depth Circulation of the Western South Atlantic. *Geophysical Research Letters*, **26 (21)**, 3329–3332, doi: http://dx.doi.org/10.1029/1999GL002355.

Buckingham, C. E., J. Gula, and X. Carton, 2020: The Role of Curvature in Modifying Frontal Instabilities. Part I: Review of Theory and Presentation of a Nondimensional Instability Criterion. *Journal of Physical Oceanography*, **51 (2)**, 299–315, doi: 10.1175/jpo-d-19-0265.1.

Calil, P. H., and K. J. Richards, 2010: Transient upwelling hot spots in the oligotrophic North Pacific. *Journal of Geophysical Research: Oceans*, **115 (2)**, doi: 10.1029/2009JC005360.

Calil, P. H. R., N. Suzuki, B. Baschek, and I. C. A. da Silveira, 2021: Filaments, Fronts and Eddies in the Cabo Frio Coastal Upwelling System, Brazil. *Fluids*, **6 (2)**, 54, doi: 10.3390/fluids6020054, URL https://www.mdpi.com/2311-5521/6/2/54.

Carton, J. A., G. A. Chepurin, and L. Chen, 2018: SODA3: A new ocean climate reanalysis. *Journal of Climate*, **31 (17)**, 6967–6983, doi: 10.1175/jcli-d-18-0149.1, URL https://doi.org/10.1175/JCLI-.

Charney, J. G., 1971: Geostrophic Turbulence. *Journal of the Atmospheric Sciences*, **28 (6)**, 1087–1095, doi: 10.1175/1520-0469(1971)028<1087:gt>2.0.co;2.

Chelton, D. B., M. G. Schlax, and R. M. Samelson, 2011: Global observations of nonlinear mesoscale eddies. *Progress in Oceanography*, **91 (2)**, 167–216, doi: 10.1016/j.pocean.2011.01.002.

Costa, V. S., G. N. Mill, M. Gabioux, G. S. Grossmann-Matheson, and A. M. Paiva, 2017: The recirculation of the intermediate western boundary current at the Tubarão Bight – Brazil. *Deep-Sea Research Part I: Oceanographic Research Papers*, **120**, 48–60, doi: 10.1016/j.dsr.2016.12.001.

D'Asaro, E., 1988: Generation of submesoscale vortices: A new mechanism. *Journal of Geophysical Research*, **93 (C6)**, 6685, doi: 10.1029/jc093ic06p06685.

D'Asaro, E., C. Lee, L. Thomas, and R. Harcourt, 2011: Enhanced Turbulence and Energy Dissipation at Ocean Fronts. *Science*, **332 (6027)**, 318–322, doi: https://doi.org/10.1126/science.1201515.

de Boyer Montégut, C., G. Madec, A. S. Fischer, A. Lazar, and D. Iudicone, 2004: Mixed layer depth over the global ocean: An examination of profile data and a profile-based climatology. *Journal of Geophysical Research C: Oceans*, **109 (12)**, 1–20, doi: https://doi.org/10.1029/2004JC002378.

de Marez, C., X. Carton, S. Corréard, P. L'Hégaret, and M. Morvan, 2020: Observations of a Deep Submesoscale Cyclonic Vortex in the Arabian Sea. *Geophysical Research Letters*, **47 (13)**, doi: 10.1029/2020GL087881.

Dewar, W. K., and H. Meng, 1995: The Propagation of Submesoscale Coherent Vortices. *Journal of Physical Oceanography*, **25**, 1745–1770.

Doubell, M. J., D. Spencer, P. D. van Ruth, C. Lemckert, and J. F. Middleton, 2018: Observations of vertical turbulent nitrate flux during summer in the Great Australian Bight. *Deep-Sea Research Part II: Topical Studies in Oceanography*, **157**, 27–35, doi: 10.1016/j.dsr2.2018.08.007.

Dugan, J. P., R. P. Mied, P. C. Mignerey, and A. F. Schuetz, 1982: COMPACT, INTRATHERMOCLINE EDDIES IN THE SARGASSO SEA. *Journal of Geophysical Research*, **87 (C1)**, 385–393, doi: 10.1029/JC087iC01p00385.

Dunckley, J. F., J. R. Koseff, J. V. Steinbuck, S. G. Monismith, and A. Genin, 2012: Comparison of mixing efficiency and vertical diffusivity models from temperature microstructure. *Journal of Geophysical Research: Oceans*, **117 (10)**, 10 008, doi: 10.1029/2012JC007967.

Egbert, G. D., and S. Y. Erofeeva, 2002: Efficient inverse modeling of barotropic ocean tides. *Journal of Atmospheric and Oceanic Technology*, **19 (2)**, 183 – 204, doi: 10.

1175/1520-0426(2002)019<0183:EIMOBO>2.0.CO;2, URL https://journals.ametsoc.org/view/journals/atot/19/2/1520-0426_2002_019_0183_eimobo_2_0_co_2.xml.

Ferrari, R., and D. L. Rudnick, 2000: Thermohaline variability in the upper ocean. *Journal of Geophysical Research: Oceans*, **105 (C7)**, 16 857–16 883, doi: 10.1029/2000jc900057.

Ferrari, R., and C. Wunsch, 2009: Ocean Circulation Kinetic Energy: Reservoirs, Sources, and Sinks. *Annual Review of Fluid Mechanics*, **41 (1)**, 253–282, doi: 10.1146/annurev.fluid.40.111406.102139.

Firing, E., 1995: Processing adcp data with the codas software system version 3.1. *Joint Institute for Marine and Atmospheric Research, University of Hawaii & National Oceanographic Data Center*.

Frenger, I., D. Bianchi, C. Stührenberg, A. Oschlies, J. Dunne, C. Deutsch, E. Galbraith, and F. Schütte, 2018: Biogeochemical Role of Subsurface Coherent Eddies in the Ocean: Tracer Cannonballs, Hypoxic Storms, and Microbial Stewpots? *Global Biogeochemical Cycles*, **32 (2)**, 226–249, doi: 10.1002/2017GB005743.

Fu, L. L., 2006: Pathways of eddies in the South Atlantic Ocean revealed from satellite altimeter observations. *Geophysical Research Letters*, **33 (14)**, doi: 10.1029/2006GL026245.

Gargett, A. E., 1997: ”Theories” and techniques for observing turbulence in the ocean euphotic zone. *Scientia Marina*, **61**, 25–45.

Garzoli, S. L., and R. Matano, 2011: The South Atlantic and the Atlantic Meridional Overturning Circulation. *Deep-Sea Research Part II: Topical Studies in Oceanography*, **58 (17-18)**, 1837–1847, doi: 10.1016/j.dsr2.2010.10.063.

Grasshoff, K., K. Kremling, and M. Ehrhardt, 2009: *Methods of seawater analysis*. John Wiley & Sons.

Gregg, M. C., 1987: Diapycnal mixing in the thermocline: A review. *Journal of Geophysical Research: Oceans*, **92 (C5)**, 5249–5286, doi: 10.1029/JC092iC05p05249.

Gregg, M. C., 1989: Scaling turbulent dissipation in the thermocline. *Journal of Geophysical Research*, **94 (C7)**, 9686, doi: 10.1029/jc094ic07p09686.

Gregg, M. C., 1999: Uncertainties and limitations in measuring ε and χ T. *Journal of Atmospheric and Oceanic Technology*, **16 (11)**, 1483–1490, doi: 10.1175/1520-0426(1999)016<1483:UALIMA>2.0.CO;2.

Gregg, M. C., E. D'Asaro, J. Riley, and E. Kunze, 2018: Mixing Efficiency in the Ocean. *Annual Review of Marine Science*, **10 (1)**, 443–473, doi: 10.1146/annurev-marine-121916-063643.

Guerra, L. A. A., A. M. Paiva, and E. P. Chassignet, 2018: On the translation of Agulhas rings to the western South Atlantic Ocean. *Deep-Sea Research Part I: Oceanographic Research Papers*, **139**, 104–113, doi: 10.1016/j.dsr.2018.08.005.

Gula, J., T. M. Blacic, and R. E. Todd, 2019: Submesoscale Coherent Vortices in the Gulf Stream. *Geophysical Research Letters*, **46 (5)**, 2704–2714, doi: 10.1029/2019GL081919.

Gula, J., M. J. Molemaker, and J. C. McWilliams, 2015: Topographic vorticity generation, submesoscale instability and vortex street formation in the Gulf Stream. *Geophysical Research Letters*, **42 (10)**, 4054–4062, doi: 10.1002/2015GL063731, URL https://onlinelibrary.wiley.com/doi/abs/10.1002/2015GL063731.

Gula, J., M. J. Molemaker, and J. C. McWilliams, 2016: Topographic generation of submesoscale centrifugal instability and energy dissipation. *Nature Communications*, **7**, doi: 10.1038/ncomms12811.

Hasegawa, D., H. Yamazaki, R. G. Lueck, and L. Seuront, 2004: How islands stir and fertilize the upper ocean. *Geophysical Research Letters*, **31 (16)**, doi: 10.1029/2004GL020143.

Haynes, P. H., and M. E. McIntyre, 1987: On the evolution of vorticity and potential vorticity in the presence of diabatic heating and frictional or other forces. *Journal of the Atmospheric Sciences*, **44 (5)**, 828–841.

Hoskins, B. J., 1974: The role of potential vorticity in symmetric stability and instability. *Quarterly Journal of the Royal Meteorological Society*, **100 (425)**, 480–482, doi: https://doi.org/10.1002/qj.49710042520.

Hoskins, B. J., and F. P. Bretherton, 1972: Atmospheric Frontogenesis Models: Mathematical Formulation and Solution. *Journal of the Atmospheric Sciences*, **29**, 11–37, doi: https://doi.org/10.1175/1520-0469(1972)029<0011:AFMMFA>2.0.CO;2.

Houry, S., E. Dombrowsky, P. de Mey, and J.-F. Minster, 1987: Brunt-Vaisala Frequency and Rossby Radii in the South Atlantic. *Journal of Physical Oceanography*, **17**, 1619–1626.

Imberger, J., and G. N. Ivey, 1991: On the Nature of Turbulence in a Stratified Fluid. Part II: Application to Lakes. *Journal of Physical Oceanography*, **21 (5)**, 659–680, doi: 10.1175/1520-0485(1991)021<0659:otnoti>2.0.co;2.

Isern-Fontanet, J., E. García-Ladona, and J. Font, 2006: Vortices of the Mediterranean Sea: An altimetric perspective. *Journal of Physical Oceanography*, **36 (1)**, 87–103, doi: 10.1175/JPO2826.1.

Itoh, S., I. Yasuda, T. Nakatsuka, J. Nishioka, and Y. N. Volkov, 2010: Fine- and microstructure observations in the Urup Strait, Kuril Islands, during August 2006. *Journal of Geophysical Research: Oceans*, **115 (8)**, 8004, doi: 10.1029/2009JC005629.

Kaneko, H., I. Yasuda, K. Komatsu, and S. Itoh, 2012: Observations of the structure of turbulent mixing across the Kuroshio. *Geophysical Research Letters*, **39 (15)**, L15 602, doi: 10.1029/2012GL052419.

Kaneko, H., I. Yasuda, K. Komatsu, and S. Itoh, 2013: Observations of vertical turbulent nitrate flux across the Kuroshio. *Geophysical Research Letters*, **40 (12)**, 3123–3127, doi: 10.1002/grl.50613.

Kemp, M., 2019: Leonardo da vinci's laboratory: studies in flow. *Nature*, **571 (7765)**, 322–324.

Kolmogorov, A. N., 1968: Local Structure of Turbulence in an Incompressible Viscous Fluid at very High Reynolds Numbers. *Soviet Physics Uspekhi*, **10 (6)**, 734–746, doi: 10.1070/PU1968v010n06ABEH003710.

Kunze, E., E. Firing, J. M. Hummon, T. K. Chereskin, and A. M. Thurnherr, 2006: Global Abyssal Mixing Inferred from Lowered ADCP Shear and CTD Strain Profiles. *Journal of Physical Oceanography*, **36 (8)**, 1553–1576, doi: 10.1175/jpo2926.1.

Large, W. G., J. C. McWilliams, and S. C. Doney, 1994: Oceanic vertical mixing: A review and a model with a nonlocal boundary layer parameterization. *Reviews of geophysics*, **32 (4)**, 363–403.

Lazaneo, C. Z., D. C. Napolitano, I. C. A. Silveira, A. Tandon, D. G. MacDonald, R. A. Ávila, and P. H. R. Calil, 2020: On the Role of Turbulent Mixing Produced by Vertical Shear Between the Brazil Current and the Intermediate Western Boundary Current. *Journal of Geophysical Research: Oceans*, **125 (1)**, doi: 10.1029/2019JC015338, URL https://onlinelibrary.wiley.com/doi/abs/10.1029/2019JC015338.

Ledwell, J. R., E. T. Montgomery, K. L. Polzin, L. C. S. Laurent, R. W. Schmitt, and J. M. Toole, 2000: Evidence for enhanced mixing over rough topography in the abyssal ocean. *Nature*, **403 (6766)**, 179–182, doi: 10.1038/35003164.

Liu, M., and T. Rossby, 1993: Observations of the Velocity and Vorticity Structure of Gulf Stream Meanders. *Journal of physical oceanography*, **23 (12)**, 329–345, doi: 10.1175/1520-0485(1993)0232.0.CO;2.

Lueck, R. G., W. R. Crawford, and T. R. Osborn, 1983: Turbulent Dissipation Over the Continental Slope Off Vancouver Island. *Journal of Physical Oceanography*, **13 (10)**, 1809–1818, doi: 10.1175/1520-0485(1983)013<1809:tdotcs>2.0.co;2.

Luko, C., I. da Silveira, I. Simoes-Sousa, J. Araujo, and A. Tandon, 2021: Revisiting the atlantic south equatorial current. *Journal of Geophysical Research: Oceans*, **126 (7)**, e2021JC017 387.

MacDonald, D. G., J. Carlson, and L. Goodman, 2013: On the heterogeneity of stratified-shear turbulence: Observations from a near-field river plume. *Journal of Geophysical Research: Oceans*, **118 (11)**, 6223–6237, doi: 10.1002/2013JC008891.

MacDonald, D. G., and F. Chen, 2012: Enhancement of turbulence through lateral spreading in a stratified-shear flow: Development and assessment of a conceptual model. *Journal of Geophysical Research: Oceans*, **117 (5)**, C05 025, doi: 10.1029/2011JC007484.

Mahadevan, A., and A. Tandon, 2006: An analysis of mechanisms for submesoscale vertical motion at ocean fronts. *Ocean Modelling*, **14 (3-4)**, 241–256, doi: 10.1016/j.ocemod.2006.05.006.

Mahadevan, A., A. Tandon, and R. Ferrari, 2010: Rapid changes in mixed layer stratification driven by submesoscale instabilities and winds. *Journal of Geophysical Research: Oceans*, **115 (3)**, C03 017, doi: 10.1029/2008JC005203.

McCoy, D., D. Bianchi, and A. L. Stewart, 2020: Global observations of submesoscale coherent vortices in the ocean. *Progress in Oceanography*, **189**, doi: 10.1016/j.pocean.2020.102452.

McDowell, S. E., and H. T. Rossby, 1978: Mediterranean water: An intense mesoscale eddy off the bahamas. *Science*, **202 (4372)**, 1085–1087.

McMillan, J. M., A. E. Hay, R. G. Lueck, and F. Wolk, 2016: Rates of dissipation of turbulent kinetic energy in a high reynolds number tidal channel. *Journal of Atmospheric and Oceanic Technology*, **33 (4)**, 817–837, doi: 10.1175/JTECH-D-15-0167.1.

McWilliams, J. C., 1985: Submesoscale, coherent vortices in the ocean. 165–182 pp., doi: 10.1029/RG023i002p00165.

McWilliams, J. C., 2016: Submesoscale currents in the ocean. *Proceedings of the Royal Society A: Mathematical, Physical and Engineering Sciences*, **472 (2189)**, doi: 10.1098/rspa.2016.0117.

Mémery, L., M. Arhan, X. A. Alvarez-Salgado, M. J. Messias, H. Mercier, C. G. Castro, and A. F. Rios, 2000: The water masses along the western boundary of the south and equatorial Atlantic. URL www.elsevier.com/locate/pocean, 69–98 pp., doi: 10.1016/S0079-6611(00)00032-X.

Meunier, T., and Coauthors, 2018: Intrathermocline Eddies Embedded Within an Anticyclonic Vortex Ring. *Geophysical Research Letters*, **45 (15)**, 7624–7633, doi: 10.1029/2018GL077527.

Miles, J. W., 1961: On the stability of heterogeneous shear flows. *Journal of Fluid Mechanics*, **10 (4)**, 496–508, doi: 10.1017/S0022112061000305.

Molemaker, M. J., J. C. McWilliams, and X. Capet, 2010: Balanced and unbalanced routes to dissipation in an equilibrated Eady flow. *Journal of Fluid Mechanics*, **654**, 35–63, doi: 10.1017/S0022112009993272.

Molemaker, M. J., J. C. Mcwilliams, and W. K. Dewar, 2015: Submesoscale instability and generation of mesoscale anticyclones near a separation of the California undercurrent. *Journal of Physical Oceanography*, **45 (3)**, 613–629, doi: 10.1175/JPO-D-13-0225.1, URL http://journals.ametsoc.org/jpo/article-pdf/45/3/613/4563291/jpo-d-13-0225_1.pdf.

Moum, J. N., and T. R. Osborn, 1986: Mixing in the Main Thermocline. *Journal of Physical Oceanography*, **16 (7)**, 1250–1259, doi: 10.1175/1520-0485(1986)016<1250:mitmt>2.0.co;2.

Munk, W., 1981: , internal waves and small-scale processes. *Evolution of physical oceanography*, 264–291.

Munk, W., and C. Wunsch, 1998: Abyssal recipes ii: energetics of tidal and wind mixing. *Deep Sea Research Part I: Oceanographic Research Papers*, **45 (12)**, 1977–2010.

Nagai, T., A. Tandon, N. Gruber, and J. C. McWilliams, 2008: Biological and physical impacts of ageostrophic frontal circulations driven by confluent flow and vertical mixing.

Dynamics of Atmospheres and Oceans, **45 (3-4)**, 229–251, doi: 10.1016/j.dynatmoce.2007.12.001.

Nagai, T., A. Tandon, H. Yamazaki, and M. J. Doubell, 2009: Evidence of enhanced turbulent dissipation in the frontogenetic Kuroshio Front thermocline. *Geophysical Research Letters*, **36 (12)**, L12 609, doi: 10.1029/2009GL038832.

Napolitano, D. C., I. C. da Silveira, C. B. Rocha, G. R. Flierl, P. H. Calil, and R. P. Martins, 2019: On the steadiness and instability of the intermediate western boundary current between 24S and 18S. *Journal of Physical Oceanography*, **49 (10)**, doi: 10.1175/JPO-D-19-0011.1.

Napolitano, D. C., I. C. A. da Silveira, A. Tandon, and P. H. R. Calil, 2020: Submesoscale phenomena due to the Brazil Current crossing of the Vitoria Trindade Ridge. *Journal of Geophysical Research: Oceans*, doi: 10.1029/2020JC016731, URL https://onlinelibrary.wiley.com/doi/10.1029/2020JC016731.

Nencioli, F., G. Dall'Olmo, and G. D. Quartly, 2018: Agulhas Ring Transport Efficiency From Combined Satellite Altimetry and Argo Profiles. *Journal of Geophysical Research: Oceans*, **123 (8)**, 5874–5888, doi: 10.1029/2018JC013909, URL https://onlinelibrary.wiley.com/doi/abs/10.1029/2018JC013909.

Niiler, P. P., N. A. Maximenko, G. G. Panteleev, T. Yamagata, and D. B. Olson, 2003: Near-surface dynamical structure of the Kuroshio Extension. *J. Geophys. Res*, **108 (C6)**, 3193, doi: 10.1029/2002JC001461.

Nikurashin, M., and R. Ferrari, 2011: Global energy conversion rate from geostrophic flows into internal lee waves in the deep ocean. *Geophysical Research Letters*, **38 (8)**, L08 610, doi: 10.1029/2011GL046576.

Nikurashin, M., G. K. Vallis, and A. Adcroft, 2013: Routes to energy dissipation for geostrophic flows in the Southern Ocean. *Nature Geoscience*, **6 (1)**, 48–51, doi: 10.1038/ngeo1657.

Oakey, N. S., 1982: Determination of the Rate of Dissipation of Turbulent Energy from Simultaneous Temperature and Velocity Shear Microstructure Measurements. *Journal of Physical Oceanography*, **12 (3)**, 256–271, doi: 10.1175/1520-0485(1982)012<0256:dotrod>2.0.co;2.

Osborn, T. R., 1980: Estimates of the Local Rate of Vertical Diffusion from Dissipation Measurements. *Journal of Physical Oceanography*, **10 (1)**, 83–89, doi: 10.1175/1520-0485(1980)010<0083:eotlro>2.0.co;2.

Pereira, A. F., A. L. Belém, B. M. Castro, and R. Geremias, 2005: Tide-topography interaction along the eastern Brazilian shelf. *Continental Shelf Research*, **25 (12-13)**, 1521–1539, doi: 10.1016/j.csr.2005.04.008.

Polzin, K. L., J. M. Toole, J. R. Ledwell, and R. W. Schmitt, 1997: Estimates of diapycnal mixing in the abyssal ocean. *Science*, **276 (5309)**, 93–96, doi: 10.1126/science.264.5162.1120.

Ramachandran, S., and Coauthors, 2018: Submesoscale Processes at Shallow Salinity Fronts in the Bay of Bengal: Observations during the Winter Monsoon. *Journal of Physical Oceanography*, **48 (3)**, 479–509, doi: 10.1175/jpo-d-16-0283.1.

Rocha, C. B., I. C. da Silveira, B. M. Castro, and J. A. M. Lima, 2014: Vertical structure, energetics, and dynamics of the Brazil Current System at 22°S-28°S. *Journal of Geophysical Research: Oceans*, **119 (1)**, 52–69, doi: 10.1002/2013JC009143.

Rodrigues, R. R., L. M. Rothstein, and M. Wimbush, 2007: Seasonal Variability of the South Equatorial Current Bifurcation in the Atlantic Ocean: A Numerical Study. *Journal of Physical Oceanography*, **37 (1)**, 16–30, doi: 10.1175/jpo2983.1, URL http://journals.ametsoc.org/doi/abs/10.1175/JPO2983.1.

Ruddick, B., A. Anis, and K. Thompson, 2000: Maximum likelihood spectral fitting: The batchelor spectrum. *Journal of Atmospheric and Oceanic Technology*, **17 (11)**, 1541–1555, doi: 10.1175/1520-0426(2000)017<1541:MLSFTB>2.0.CO;2.

Rudnick, D. L., 2001: On the skewness of vorticity in the upper ocean. *Geophysical Research Letters*, **28 (10)**, 2045–2048, doi: 10.1029/2000GL012265.

Rumyantseva, A., N. Lucas, T. Rippeth, A. Martin, S. C. Painter, T. J. Boyd, and S. Henson, 2015: Ocean nutrient pathways associated with the passage of a storm. *Global Biogeochemical Cycles*, **29 (8)**, 1179–1189, doi: 10.1002/2015GB005097.

Sarmiento, J. L., and N. Gruber, 2006: *Ocean biogeochemical dynamics*. Princeton University Press.

Sharples, J., C. M. Moore, T. P. Rippeth, P. M. Holligan, D. J. Hydes, N. R. Fisher, and J. H. Simpson, 2001: Phytoplankton distribution and survival in the thermocline. *Limnology and Oceanography*, **46 (3)**, 486–496, doi: 10.4319/lo.2001.46.3.0486.

Sharples, J., and Coauthors, 2007: Spring-neap modulation of internal tide mixing and vertical nitrate fluxes at a shelf edge in summer. *Limnology and Oceanography*, **52 (5)**, 1735–1747, doi: 10.4319/lo.2007.52.5.1735.

Shchepetkin, A. F., and J. C. McWilliams, 2005: The regional oceanic modeling system (ROMS): A split-explicit, free-surface, topography-following-coordinate oceanic model. *Ocean Modelling*, **9 (4)**, 347–404, doi: 10.1016/j.ocemod.2004.08.002.

Shih, L. H., J. R. Koseff, G. N. Ivey, and J. H. Ferziger, 2005: Parameterization of turbulent fluxes and scales using homogeneous sheared stably stratified turbulence simulations. *Journal of Fluid Mechanics*, **525**, 193–214, doi: 10.1017/S0022112004002587.

Silveira, I. C. A., L. Calado, B. M. Castro, M. Cirano, J. A. M. Lima, and A. d. S. Mascarenhas, 2004: On the baroclinic structure of the Brazil Current-Intermediate Western Boundary Current system at 22°-23°S. *Geophysical Research Letters*, **31 (14)**, L14 308, doi: 10.1029/2004GL020036.

Silveira, I. C. A., J. A. M. Lima, A. C. K. Schmidt, W. Ceccopieri, A. Sartori, C. P. F. Franscisco, and R. F. C. Fontes, 2008: Is the meander growth in the Brazil Current system off Southeast Brazil due to baroclinic instability? *Dynamics of Atmospheres and Oceans*, **45 (3-4)**, 187–207, doi: 10.1016/j.dynatmoce.2008.01.002.

Smith, W. H., and D. T. Sandwell, 1997: Global sea floor topography from satellite altimetry and ship depth soundings. *Science*, **277 (5334)**, 1956–1962, doi: 10.1126/science.277.5334.1956.

Smith, W. H. F., and D. T. Sandwell, 1995: Global Sea Floor Topography from Satellite Altimetry and Ship Depth Soundings. *Science*, **277 (5334)**, 1956—-1962, URL http://science.sciencemag.org/www.sciencemag.org.

Soutelino, R., A. Gangopadhyay, and I. Da Silveira, 2013: The roles of vertical shear and topography on the eddy formation near the site of origin of the brazil current. *Continental Shelf Research*, **70**, 46–60.

Soutelino, R. G., I. C. A. Silveira, A. Gangopadhyay, and J. A. Miranda, 2011: Is the Brazil Current eddy-dominated to the north of 20°S? *Geophysical Research Letters*, **38 (3)**, L03 607, doi: 10.1029/2010GL046276.

Srinivasan, K., J. C. McWilliams, M. J. Molemaker, and R. O. Barkan, 2019: Submesoscale vortical wakes in the lee of topography. *Journal of Physical Oceanography*, **49 (7)**, 1949–1971, doi: 10.1175/JPO-D-18-0042.1, URL https://doi.org/10.1175/JPO-D-18-.

Srinivasan, K., J. C. McWilliams, L. Renault, H. G. Hristova, J. Molemaker, and W. S. Kessler, 2017: Topographic and mixed layer submesoscale currents in the near-surface southwestern tropical Pacific. *Journal of Physical Oceanography*, **47 (6)**, 1221–1242, doi: 10.1175/JPO-D-16-0216.1.

Stramma, L., and M. England, 1999: On the water masses and mean circulation of the South Atlantic Ocean. *Journal of Geophysical Research: Oceans*, **104 (C9)**, 20 863–20 883, doi: 10.1029/1999jc900139.

Taylor, G. I., 1938: The Spectrum of Turbulence. *Proceedings of the Royal Society of London. Series A-Mathematical and Physical Sciences*, **164 (919)**, 476–490, doi: 10.2514/8.1235.

Taylor, J. R., and R. Ferrari, 2009: On the equilibration of a symmetrically unstable front via a secondary shear instability. *Journal of Fluid Mechanics*, **622**, 103–113, doi: 10.1017/S0022112008005272.

Tennekes, H., and J. L. Lumley, 1989: *A first course in turbulence*. MIT press.

Thomas, L. N., 2005: Destruction of potential vorticity by winds. *Journal of Physical Oceanography*, **35 (12)**, 2457–2466, doi: 10.1175/JPO2830.1.

Thomas, L. N., A. Tandon, and A. Mahadevan, 2008: Submesoscale processes and dynamics. *Ocean modeling in an Eddying Regime*, **177**, 17–38.

Thomas, L. N., J. R. Taylor, E. A. D'Asaro, C. M. Lee, J. M. Klymak, and A. Shcherbina, 2016: Symmetric Instability, Inertial Oscillations, and Turbulence at the Gulf Stream Front. *Journal of Physical Oceanography*, **46 (1)**, 197–217, doi: 10.1175/jpo-d-15-0008.1.

Thomas, L. N., J. R. Taylor, R. Ferrari, and T. M. Joyce, 2013: Symmetric instability in the Gulf Stream. *Deep-Sea Research Part II: Topical Studies in Oceanography*, **91**, 96–110, doi: 10.1016/j.dsr2.2013.02.025.

Thorpe, S. A., 1973: Experiments on instability and turbulence in a stratified shear flow. *Journal of Fluid Mechanics*, **61 (4)**, 731–751, doi: 10.1017/S0022112073000911.

Thorpe, S. A., 2005: *The turbulent ocean*. Cambridge University Press.

Thorpe, S. A., 2007: *An Introduction to Ocean Turbulence An Introduction to*. Cambridge University Press, 240 pp.

Veronis, G., 1972: On properties of seawater defined by temperature. *Deep-Sea Res*, **24**, 325–329.

Vic, C., J. Gula, G. Roullet, and F. Pradillon, 2018: Dispersion of deep-sea hydrothermal vent effluents and larvae by submesoscale and tidal currents. *Deep-Sea Research Part I: Oceanographic Research Papers*, **133**, 1–18, doi: 10.1016/j.dsr.2018.01.001.

Vic, C., G. Roullet, X. Capet, X. Carton, M. J. Molemaker, and J. Gula, 2015: Eddy-topography interactions and the fate of the Persian Gulf Outflow. *Journal of Geophysical Research: Oceans*, **120 (10)**, 6700–6717, doi: 10.1002/2015JC011033, URL https://onlinelibrary.wiley.com/doi/abs/10.1002/2015JC011033.

Whitt, D. B., and J. R. Taylor, 2017: Energetic Submesoscales Maintain Strong Mixed Layer Stratification during an Autumn Storm. *Journal of Physical Oceanography*, **47 (10)**, 2419–2427, doi: 10.1175/jpo-d-17-0130.1.

Wolk, F., H. Yamazaki, L. Seuront, and R. G. Lueck, 2002: A new free-fall profiler for measuring biophysical microstructure. *Journal of Atmospheric and Oceanic Technology*, **19 (5)**, 780–793, doi: 10.1175/1520-0426(2002)019<0780:ANFFPF>2.0.CO;2.

Zhai, X., H. L. Johnson, and D. P. Marshall, 2010: Significant sink of ocean-eddy energy near western boundaries. *Nature Geoscience*, **3 (9)**, 608–612, doi: 10.1038/ngeo943.

Zhang, Z., J. Tian, B. Qiu, W. Zhao, P. Chang, D. Wu, and X. Wan, 2016: Observed 3D Structure, Generation, and Dissipation of Oceanic Mesoscale Eddies in the South China Sea. *Scientific Reports*, **6**, doi: 10.1038/srep24349.